AN ABSTRACT OF THE DISSERTATION OF

Sasiporn Prasertpalichat for the degree of Doctor of Philosophy in Materials Science presented on April 7, 2015.

Title: Non-Stoichiometry in Bismuth Perovskite Solid Solutions.

Abstract approved:

_____

David P. Cann

The role of A-site non-stoichiometry was investigated in lead-free piezoelectric ceramics based on compositions in the 1-x($Bi_{0.5}Na_{0.5}TiO_3$)-$x$$BaTiO_3$ system near the morphotropic phase boundary where x = 0.055, 0.06 and 0.07. The samples were prepared by a conventional solid state mixed oxide route with the A-site stoichiometry modified to incorporate donor-doping (through Bi-excess) and acceptor-doping (through Na-excess). While no change in the crystal structure was observed via donor-doping, acceptor-doping was found to promote rhombohedral distortions. A significant improvement in dielectric properties was observed in donor-doped compositions and, in contrast, a degradation in properties was observed in acceptor-doped compositions. Compared to the stoichiometric composition, the acceptor-doped compositions displayed a significant increase in coercive field (E_c) which is an indication of domain wall pinning as found in hard piezoelectrics such as $Pb(Zr_xTi_{1-x})O_3$ (PZT). This result was further confirmed via polarization hysteresis studies including PUND tests and remanent P-E hysteresis analyses. Moreover, all A-site acceptor-doped compositions also exhibited an increase in mechanical quality

factor (Q_m) as well as a decrease in piezoelectric coefficient (d_{33}), dielectric loss (tan δ), remanent polarization (P_r) and dielectric permittivity, which are all the typical characteristics of the effects of "hardening". The mechanism for the observed hardening in A-site acceptor doped BNT-based systems is linked to changes in the long-range domain structure and defect chemistry.

Impedance spectroscopy was utilized to analyze the effects of A-site non-stoichiometry on the conduction mechanisms. An electrically heterogeneous microstructure was observed in both the stoichiometric and Na-excess compositions. In addition, the Na-excess compositions exhibited lower resistivities ($\rho \sim 10^3$ Ω-cm) with characteristic peaks in the impedance data indicating ionic conductivity similar to recent observations of oxide ion conduction in $(Bi_{0.5}Na_{0.5})TiO_3$. In contrast, Bi-excess compositions resulted in an electrically homogeneous microstructure with an increase in resistivity by ~3-4 orders of magnitude and an associated activation energy of 1.57 eV which was close to half of the optical band gap. Long-term annealing studies were conducted at 800°C to identify changes in crystal structure and electrical properties. The results of this study demonstrates that the dielectric and electrical properties of (1-*x*)BNT-*x*BT ceramics at the compositions near the MPB are very sensitive to Bi/Na stoichiometry.

Non-Stoichiometry in Bismuth Perovskite Solid Solutions

by
Sasiporn Prasertpalichat

A DISSERTATION

submitted to

Oregon State University

in partial fulfillment of
the requirements for the
degree of

Doctor of Philosophy

Presented April 7, 2015
Commencement June 2015

Doctor of Philosophy dissertation of Sasiporn Prasertpalichat presented on April 7, 2015

APPROVED:

Major Professor, representing Materials Science

Director of the Materials Science Program

Dean of the Graduate School

I understand that my dissertation will become part of the permanent collection of Oregon State University libraries. My signature below authorizes release of my dissertation to any reader upon request.

Sasiporn Prasertpalichat, Author

ACKNOWLEDGEMENTS

First and foremost, I would like to express my deepest gratitude to my advisor, Prof. Dr. David P. Cann for all the encouragement, support and guidance throughout my time here. I am so lucky to have an advisor who is tremendously supportive and understand students in every ways. You provided us excellent, joyful, and yet motivational atmosphere for doing the research. Thank you for all the great opportunities that you have given me. Most of them are beyond my dreams and I wouldn't have had a chance to do them without your support. I would like to thanks for all the kind and cheering words, which meant a lot to me. I would also like to thanks for your prompt and patient correcting of all of my writing. Without you, I wouldn't have been able finish them. You are the best advisor that one could ever ask for.

I would like to acknowledge all of my committee members, Dr. William H. Warnes, Dr. David Ji, Dr. John F. Conley and Dr. Wade Marcum. Those feedbacks that I got during my preliminary examination were very precious and I hope that I have managed to respond to several of them here.

Getting through grad school and dissertation without being crazy requires a lot of supports from a group of people who you call "friends". And I have many many people to thank for in this regard. First of all, I would like to thank to my current and former Electroceramics group members: Nitish Kumar, thanks for all the discussions and clarifications on the concept that I didn't understand and thanks for all the other

helps as well; Narit (Sunny) Triamnak, thanks for teaching all the ceramics processing and how to use all of the equipment when I first joined the lab and throughout these past years; Eric Patterson, thanks for teaching me lots of things in the lab; Chien-Chih Huang, thanks for your kind help with my first project here at OSU; Dr. Whitney Schmidt, thanks a lot for your help in editing my thesis; Senghwa Kwon, Natthaphon Raengthon, Troy Ansell, Nopsiri Chaiyo, Ratthiporn Sumang and Connor Mccue, thanks for all the favors that you guys gave me in the lab. I would also like to thank my awesome 3rd floor Dearborn MatSci friends: Ashley Mason and Michelle Jennings, being officemates with you guys was awesome even though it's just a short period of time and thanks for all the cheering word and supports as well; Trevor K. Howard, Alexsey Ionin, Jenna Schardt, Kunal Kate and Suzanne Mirashrafi, thanks for the Durak games and fun time at happy hours. All of you are truely nice, I would never forget the good times that we've shared together. If I have forgotten anyone, I apologize

I would like to thank *Higher Educational Strategic Scholarships for Frontier Engineering* from Thai government which provided me the financial supports throughout these years.

Finally, I would especially like to thank my mom, my dad and my brother for their unconditional love. Thanks for being there with me in good and bad times. Thanks for your truly understanding and supports. Without you, I wouldn't have made it this far.

TABLE OF CONTENTS

TABLE OF CONTENTS (Continued)

Page

TABLE OF CONTENTS (Continued)

Page

LIST OF FIGURES

LIST OF FIGURES (Continued)

Figure Page

LIST OF FIGURES (Continued)

Figure Page

LIST OF FIGURES (Continued)

Figure Page

LIST OF FIGURES (Continued)

Figure Page

LIST OF TABLES

1 Introduction and Motivation

Lead-based materials such as lead zirconate titanate ($Pb[Zr_x,Ti_{1-x}]O_3$, PZT) have dominated piezoelectric materials markets for more than half a century due to the excellent piezoelectric properties. However, concerns regarding the toxicity of lead (Pb^{2+}) on environmental and human health have led to a restriction of its use in many electrical devices, as directed by legislation in the European Union and other countries. Therefore, a search for lead-free piezoelectric materials with comparable properties to that of PZT is crucial.

The excellent properties in PZT can be attributed to both the unique electronic structure of Pb^{2+} (i.e. lone pair electrons) and the existence of the morphotropic phase boundary (MPB). In terms of electronic structure, Bi^{3+} is a reasonable choice for replacing Pb^{2+} since it possesses a high polarizability as well as a similar electronic structure to that of Pb^{2+}. Therefore, various Bi-based perovskite compounds (e.g. $Bi_{0.5}Na_{0.5}TiO_3$ (BNT), $Bi_{0.5}K_{0.5}TiO_3$ (BKT), $BiFeO_3$ (BF)) as well as their solid solutions with other perovskite end members have been extensively studied. Among them, the solid solution of $(1\text{-}x)Bi_{0.5}Na_{0.5}TiO_3\text{-}xBaTiO_3$ has been the focus of many studies because of the discovery of its MPB ($\sim x = 0.06$) which is accompanied by an enhancement in electromechanical and piezoelectric properties similar to that of PZT (e.g. $d_{33} =$ 125 pC/N, $k_{33} = 55\%$ and $\varepsilon_{33}^T/\varepsilon_0 = 580$).

Despite excellent piezoelectric properties, there are barriers to implementing BNT and BNT-based material systems due to high leakage currents, which has been attributed

to defects arising from the loss of the volatile elements Bi and Na. Therefore, extensive research has been carried out to understand the effects of A-site non-stoichiometry on the electrical properties of BNT. The results show that a small change in the stoichiometry of the A-site cation can significantly affect the conductivity, the dielectric properties, and most importantly the piezoelectric properties. Further studies also show that non-stoichiometry also influences the crystal structure.

While many studies have been carried out on the end member BNT, there have been no systematic studies regarding the effects of A-site non-stoichiometry on the electrical properties of (1-*x*)BNT-*x*BT compositions near the morphotropic phase boundary. Therefore, the focus of this thesis will be:

1. To study the role of the A-site cation stoichiometry on the underlying defect equilibria and electrical properties

2. To determine the dominant conduction mechanism as a result of A-site non-stoichiometry, which will in turn help clarify the observed electrical properties

2 Background

2.1 Perovskite Structure and Tolerance Factor

The perovskite structure was first discovered by Gustav Rose in 1839 and subsequently named after a Russian mineralogist Les Alexseevich Perovski who first characterized it. Nevertheless, it was not until 1945 that the crystal structure of the mineral perovskite $CaTiO_3$ was first published by H.D. Megaw [1]. After that, compounds that have the same structural configuration as $CaTiO_3$ are referred to as perovskites. Perovskite is a major structure found in oxide compounds; however, it can be encountered in other compounds e.g. chlorides, sulfides and bromides as well [2]. Compounds with the perovskite structure were found to possess higher piezoelectric and ferroelectric properties than that of other structures (e.g. bismuth-layer structure, tungsten bronzes), and thus making them promising for many technological applications, including capacitors, microwave resonators and piezoelectric transducers.

Ideally, the perovskite structure has the stoichiometry of ABO_3 for oxides and possesses the cubic space group $Pm\bar{3}m$. A unit cell of cubic perovskite structure comprises of A site cations at the corners of the cube, a B site cation at the body center and oxygen anions at the face center as shown in Fig. 2.1 (a). The coordination number of A cation and B cation are twelve and six, respectively. Therefore, the size of A cation is normally bigger than that of B cation [3]. Alternatively, the ABO_3 perovskite structure can be visualized as an infinite three-dimensional network of corner-sharing BO_6

octahedra with an A cation sitting in the center of the cube generated by eight corner-sharing octahedra [4] as shown in Fig. 2.1 (b).

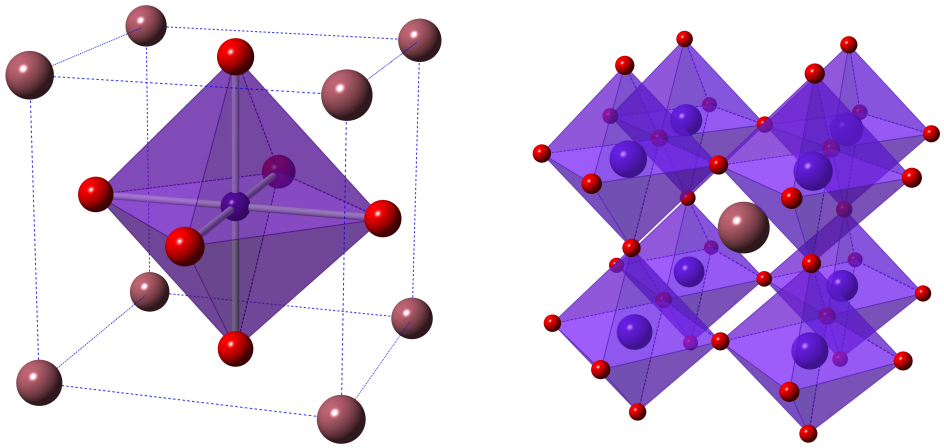

(a) (b)

Fig. 2.1 (a) unit cell of perovskite structure, ABO_3 (b) a three-dimensional corner-sharing BO_6 octahedral

Even though the A- and B-site in the perovskite structure can accommodate various cations, not all combinations of cations will result in a perovskite structure. Thus, the Goldschmidt tolerance factor (t), which was first proposed by V.M. Goldschmidt [5], is normally used for predicting the stability of the perovskite structure and is expressed as following:

$$t = \frac{(R_A + R_O)}{\sqrt{2}(R_B + R_O)} \tag{2.1}$$

where R_A, R_B and R_O are the ionic radii of the A-cation, B-cation and oxygen anion respectively. For complex perovskites in which more than one cation occupy the A-site or B-site, e.g. $A\left(B_{0.5}^{3+}B_{0.5}^{5+}\right)O_3$, an average radius of ions on each site is used. Therefore, a modified tolerance factor can be written as [6]:

$$t = \frac{(R_A + R_O)}{\sqrt{2}\left[\left(\frac{R_B^{3+} + R_B^{5+}}{2}\right) + R_O\right]} \tag{2.2}$$

Depending on a set of ionic radii being used, the range of tolerance factor where perovskite structure is stable is different. For example, if ionic radii based on octahedral coordination is used, the perovskite structure will be stable if t lies between $0.77 < t < 0.99$; instead, if the ionic radii is corrected for the 12 coordination of the A-site cation, the structure is stable when $t = 0.88$ to 1.09. Therefore, if t is beyond this limit, other structures are expected to be formed, e.g. $LiNbO_3$, which crystallizes in the ilmenite structure and not the perovskite structure despite having the chemical formula ABO_3. This could be attributed to a small size of Li ion that gives rise to a too low tolerance factor ($t = 0.86$) [7].

Typically, the ideal cubic perovskite structure exists at elevated temperature [3] e.g., at T > 130°C for $BaTiO_3$ [8], at T > 288°C for $Bi_{0.5}Na_{0.5}TiO_3$ and at T > 490°C for $PbTiO_3$ [9]. Nevertheless, room temperature cubic perovskites with a tolerance factor close to unity can be seen in some compounds, e.g. $SrTiO_3$ ($t = 1.002$, using Shannon and Pewitt radii [10]). At room temperature, most perovskite structure compounds are found

as a distorted perovskite rather than an ideal cubic form. Distortions from the ideal cubic perovskite structure come from one of three mechanisms: (1) distortion of the octahedra, (2) cation displacements within the octahedral and (3) tilting of the octahedral [4]. The first and second mechanisms arise from the electronic instability of the cation in octahedral coordination, while the third one (tilting of octahedra) is normally observed when the A-cation is too small or too large. For $t > 1$, the BO_6 octahedral network will tilt in such a way that a tetragonal distortion occurs (e.g. $BaTiO_3$). In contrast, for $t < 1$, the distortion of the perovskite structure tends to favor lower symmetries such as orthorhombic or rhombohedral symmetry.

The tolerance factor is a good guideline for predicting the stability and crystal system of the perovskite compound. However, it should be noted that it depends upon the set of ionic radii being used and for a more reliable estimation of crystal structure, more in-depth considerations of the crystal chemistry are necessary. The tolerance factor is successfully used in explaining many key properties, e.g. a relationship between tolerance factor and transition temperature of compositions at MPB by Eitel *et. al* [7]. In addition, Navrotsky determined that the enthalpy of formation in perovskite compounds becomes less exothermic as the tolerance factor deviates more from unity, indicating a decrease in the stability of the structure [11].

2.2 Ferroelectricity

Similar to ferromagnetic materials which have spontaneous magnetization, ferroelectric materials are defined as polar materials which possess spontaneous polarizations that can be reoriented by an external applied electric field.

An evolution of spontaneous polarization can be visualized through the perovskite $BaTiO_3$, which was the first ceramic material in which ferroelectric behavior was observed. In $BaTiO_3$, upon cooling down across its Curie point (~130°C) [8], the structure starts to change from a high temperature paraelectric cubic phase to a ferroelectric tetragonal phase as seen in Fig. 2.2 (a) and (b). Accompanying this cubic-tetragonal transformation is the occurrence of spontaneous polarization in the <001> direction as a result of a relative displacement of Ti^{4+} cations to O^{2-} anions [12]. A displacement of Ti^{4+} towards O^{2-} in the <001> direction was proven to be energetically favorable since it also causes the Ti^{4+} in the above unit cell to locate further away from that O^{2-}; thus, leading to a similar displacement of all Ti^{4+} ions in the same column. Finally, a coupling of the adjacent column will give rise to a similar displacement of all Ti^{4+} in the entire $BaTiO_3$ sample. Upon further cooling, $BaTiO_3$ will transform to orthorhombic phase at 0°C and to a rhombohedral phase at -80°C. The corresponding spontaneous polarization directions for orthorhombic (*mm2*) and rhombohedral (*3m*) are parallel to the face diagonal and the body diagonal, respectively [8, 9, 13].

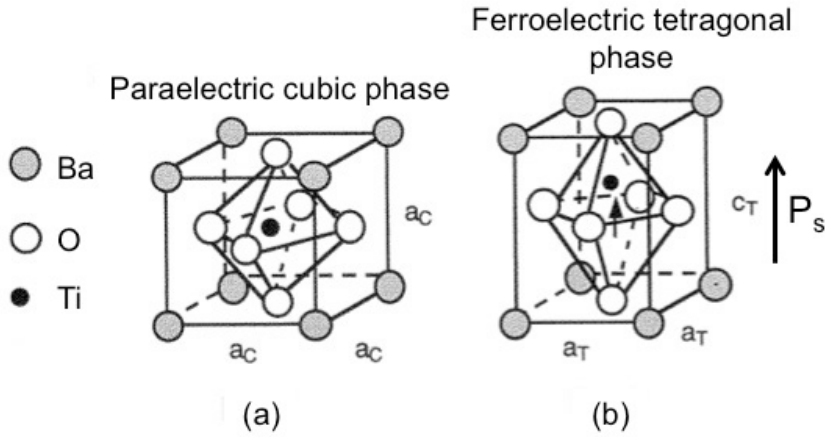

Fig. 2.2 A transformation of $BaTiO_3$ from (a) high temperature (T > 130°C) paraelectric cubic phase to (b) ferroelectric tetragonal phase with a spontaneous polarization along <001> direction (taken from [9])

An important consequence of the spontaneous polarization is the occurrence of surface charge, which generates a depolarizing field (E_d) aligned in the opposite direction to the spontaneous polarization (P_s). To minimize the electrostatic energy associated with this depolarizing field, the "twinning process" (i.e. a splitting of ferroelectric materials into many regions with oppositely oriented polarizations) occurs as shown in Fig 2.3. The region that contains the same direction of polarization is called a domain and the boundary between these domains whose polarization orientation align oppositely is called 180° domain wall. Apart from 180° domain walls, 90° domain walls could also be generated during cubic-tetragonal phase transition in order to minimize a resultant elastic energy from the mechanical stress as seen in Fig. 2.3. Allowed domain states and domain-wall orientations depend on crystalline symmetry. For example, in rhombohedral ferroelectric perovskite structures, 180°, 109° and 71° domain walls can occur [8].

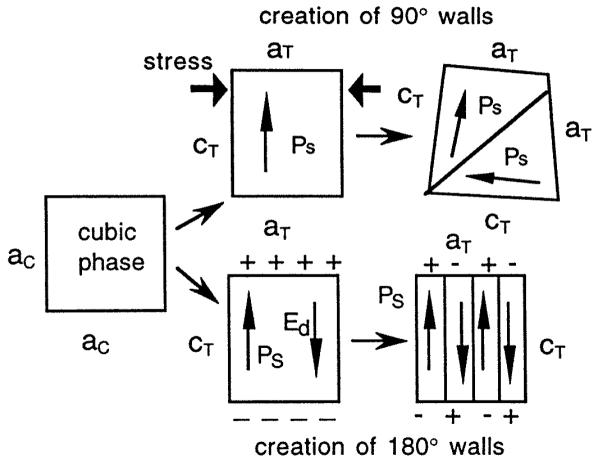

Fig. 2.3 A schematic representation of 180° and 90° domain wall formation in a tetragonal perovskite ferroelectric (figure taken from [9])

The most important characteristic of a ferroelectric material is a reorientation of polarization under applied electric field, which will appear as hysteresis loop in a polarization electric field (*P-E*) plot [14] as seen in Fig. 2.4. According to Fig. 2.4, a linear increase in polarization (section AB) occurs at small field strength. Then, a drastic and non-linear increase in polarization (section BC) is obtained after the field strength that is sufficient to switch a domain is reached. Finally, after all the domains are aligned, a linear increase in polarization is obtained again at high field end (section CD). From the *P-E* loop, important characteristic parameters such as remanent polarization (P_r), coercive field (E_c), and spontaneous polarization (P_s) can be obtained. The P_r is the polarization that remains unchanged after applied electric field is removed (point E). And the coercive field (E_c) is the electric field strength that is needed to bring polarization back to zero (point F). In other words, E_c indicates the "hardness" of domain

switching. For spontaneous polarization (P_s), its value can be estimated by extrapolating the linear section (section CD) to intercept on the polarization axis.

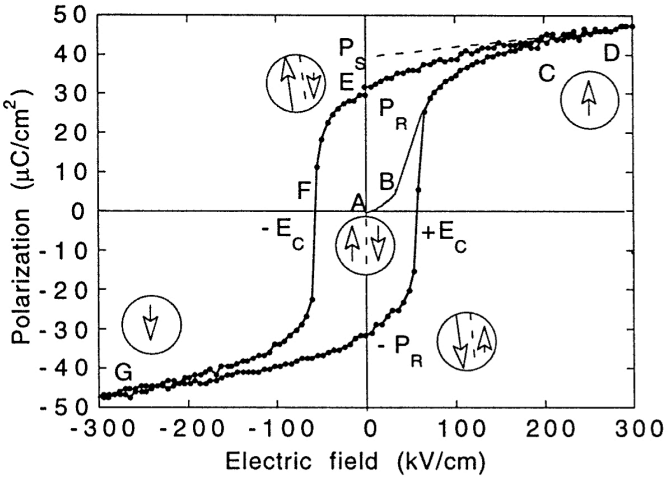

Fig. 2.4. A typical ferroelectric *P-E* hysteresis loop showing characteristic parameter such as coercive field (E_c), remanent polarization (P_r) and spontaneous polarization (P_s) (figure taken from [9])

Though hysteresis loops can provide useful information related to ferroelectric material properties, interpretation of the *P-E* hysteresis loop should be made with caution, as it is affected by many factors. One of the most important factors is conductivity. For an *ideal* ferroelectric insulator, a change of measured charge only comes from polarization switching. However, in *real* ferroelectric, conductivity always coexists and affects the measured charge according to the following equation:

$$Q = 2P_rA + \sigma EAt \tag{2.3}$$

Where Q is charge (C/cm^2), A is area (cm^2), σ is the electrical conductivity and t is the measuring time. According to a criterion given by Dawber *et al.* [15], the effect of conductivity is negligible if $\sigma < 10^{-7}$ S/cm and, in contrast, a deterioration of ferroelectricity could be observed if conductivity is large ($\sigma > 10^{-6}$ S/cm). For the *P-E* loop, as the conductivity increases a transition from ideal square ferroelectric hysteresis loop to a round loop could be observed, as shown in Fig 2.5 [16].

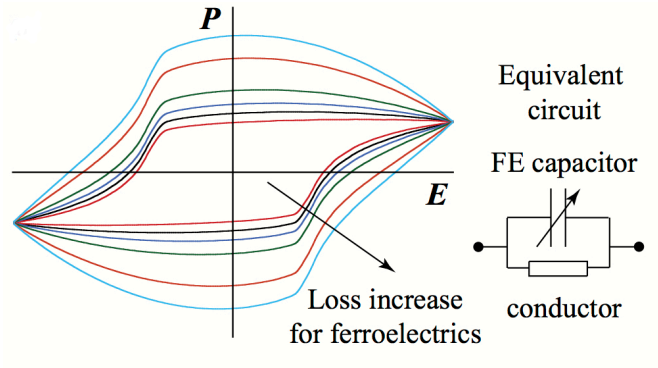

Fig. 2.5. Schematic representation of *P-E* hysteresis loop for ferroelectric sample showing a transition from square loop to round loop with increasing conductivity (figure taken from [16])

From Fig. 2.5, it can also be seen that both P_r and E_c also increase with increasing conductivity. An increase of E_c is typically an indication of the hardness of domain wall switching as a result of pinning centers (i.e. defects). Thus, it is very important to rule out the effect of conductivity in ferroelectric hysteresis loops prior to any interpretation.

In addition to conductivity, other factors including charged defects, mechanical stresses, grain sizes, anisotropy and phase boundaries could also affect ferroelectric hysteresis loops. For example, a decrease in grain size could result in a transition of ferroelectric loop from a classic square shape to a slanted one, as both intrinsic lattice distortion and extrinsic domain wall contribution is reduced with decreasing grain size [16].

2.3 Piezoelectricity

In 1880, the Curie brothers (Jacques and Pierre) observed that an electric charge could be induced in some crystals (e.g. quartz, topaz, tourmaline and Rochelle salt) under an applied mechanical stress. The developed charge was found to be a function of stress and its sign was also switched as the applied stress changes from tensile to compressive stress. This phenomenon was termed “direct” piezoelectric effect. Later, the “converse” piezoelectric effect, i.e. a deformation of crystals under an applied electric field, was proved to exist by both thermodynamic principles and experiment. Similar to the direct piezoelectric effect, a sign of crystal deformation or strain is also changed (e.g. elongation or contraction) if the direction of electric field is reversed [13, 14]. The direct piezoelectric effect is widely utilized in force, pressure, vibration and acceleration sensors while the converse piezoelectric effect is used in actuator and displacement devices [8, 9].

The piezoelectric effect is strongly symmetry dependent, thus can be found only in noncentrosymmetric point groups (or crystal classes). Of the 32 crystallographic classes, only 21 are noncentrosymmetric. However, the cubic 432 class has a set of symmetry elements that manifests itself in such a way that piezoelectricity equals zero; therefore, only 20 remaining crystal classes possess piezoelectricity. Of these 20 classes, ten classes possess a unique polar axis (i.e. electric dipole moment), which may exhibit spontaneous polarization. Under a uniform heat, the pyroelectric effect could be observed along this unique polar axis due to a change in the magnitude of the electric dipole. According to this classification, ferroelectric materials, which possess spontaneous polarization that can re-orient with electric field, are therefore a subset of both pyroelectric and piezoelectric materials [14]. The symmetry classification diagram for piezoelectricity is shown in Fig. 2.6.

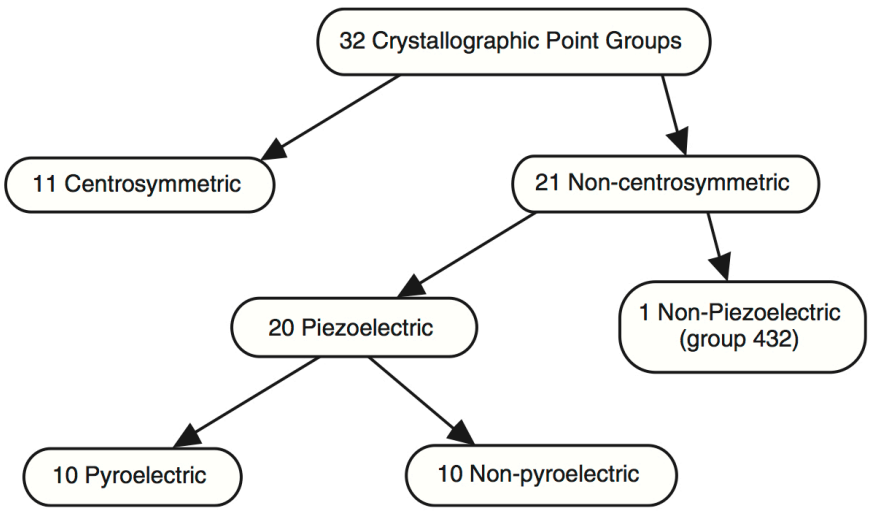

Fig. 2.6 Symmetry classification diagram for piezoelectricity (taken from [13])

Since the piezoelectric effect differs along different axes, the tensor form is used for accurately describing the phenomenon. The direct and converse piezoelectric effect can be described using tensor notation with the following equations (i, j, k = 1, 2, 3):

$$D_k = d_{kij}\sigma_{ij} \qquad \text{(Direct)} \qquad (2.4)$$

$$S_{ij} = d_{kij}E_k \qquad \text{(Converse)} \qquad (2.5)$$

where electric displacement (D_k) and electric field (E_k) are first-rank tensors, stress (σ_{ij}) and strain (S_{ij}) are second-rank tensors and the piezoelectric coefficient (d_{kij}) is a third-rank tensor. The unit for the piezoelectric coefficient (d_{kij}) is C/N (i.e. coulomb per newton) for the direct piezoelectric effect and m/V (i.e. meter per volt) for the converse piezoelectric effect. In theory, the number of independent components in any n^{th}-rank tensor equals to 3^n, therefore, the piezoelectric coefficient, a third-rank tensor, would have $3^3 = 27$ components. However, due to the symmetry of the stress ($\sigma_{ij} = \sigma_{ji}$) and strain ($S_{ij} = S_{ji}$), the permissible components of the piezoelectric coefficient tensor reduce to 18. Furthermore, according to Neumann's principle [17], which states "symmetry elements of any physical properties of a crystal must include symmetry elements of the point group of that crystal"; as the symmetry is higher, the number of the independent components in piezoelectric coefficient tensor will be lower. For example, the maximum of 18 independent components can be found in piezoelectric tensor of triclinic crystal class (point group *1*) whereas only 3 independent components are found in that of tetragonal *4mm* point group as seen in Fig. 2.7.

$$\begin{pmatrix} d_{11} & d_{12} & d_{13} & d_{14} & d_{15} & d_{16} \\ d_{21} & d_{22} & d_{23} & d_{24} & d_{25} & d_{26} \\ d_{31} & d_{32} & d_{33} & d_{34} & d_{35} & d_{36} \end{pmatrix} \qquad \begin{pmatrix} 0 & 0 & 0 & 0 & d_{15} & 0 \\ 0 & 0 & 0 & d_{15} & 0 & 0 \\ d_{31} & d_{31} & d_{33} & 0 & 0 & 0 \end{pmatrix}$$

(a) (b)

Fig. 2.7 Matrix of piezoelectric coefficients for (a) triclinic symmetry (point group *1*) and (b) tetragonal symmetry (point group *4mm*)

The piezoelectric response comes from not only intrinsic but also extrinsic contributions. The intrinsic contribution depends on only lattice properties and can be expressed according to the following equation:

$$d \approx 2Q\varepsilon_0\varepsilon P_r \tag{2.6}$$

where Q is the electrostrictive constant, ε_0 and ε are the permittivities of free space and the material, respectively, and P_r is the remanent polarization. Hence, a material with large remanent polarization and polarizability is expected to have high piezoelectric coefficient due to high intrinsic contribution. The extrinsic contribution comes from movements of non-180° domain walls. In some materials where the switching of domain walls is relatively easy (e.g. soft PZT ceramics), the extrinsic contribution was found to contribute as much as 50% to the net piezoelectric coefficient [18].

Similar to the *P*-*E* hysteresis loop, strain-electric field (*S*-*E*) hysteresis loops can be observed during electric field cycling as shown in Fig. 2.8. Due to the unique shape the *S*-*E* hysteresis loop is often called a "butterfly loop". Figure 2.8 (a) shows a typical *S*-*E* hysteresis loop from an ideal monodomain single crystal in which the polarization can promptly switch by only 180° (i.e. there are no 90° domain walls). Since there is no domain wall switching involved in this case, the strain will linearly increase along the section ABC through the converse piezoelectric effect according to equation (5). Upon decreasing the field, strain also linearly decreases along the same path (section ABC) until reaching zero at zero electric field. A further increase in the electric field in the negative direction will result in a decrease of strain with respect to point A. After all polarizations align along the new electric field direction, an abrupt increase in the strain as seen in section DE of the plot occurs. Finally, a linear increase in the strain along section EFA is observed again upon further increasing the electric field. In contrast, real ceramics contain both 180° and non-180° domain walls. Thus, the *S*-E hysteresis loop will arise not only from a normal converse piezoelectric effect but also from switching and movement of the domain walls. The contribution from the domain leads to a nonlinear increase in strain and a hysteresis loop as shown in Fig. 2.8 (b). As each domain possesses a different coercive field, a less sudden change in strain is also observed. And upon electric field removal, a remanent strain will be observed at zero field since some domains might not switch back to their original states.

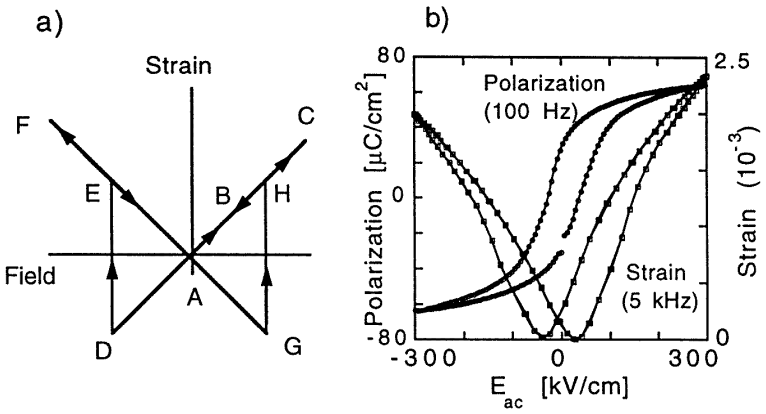

Fig. 2.8 (a) Idealized *S-E* hysteresis loop from monodomain single crystal which assume prompt switching of polarization by 180° domain only (b) actual polarization and strain loops measured on (111)-oriented sol-gel $Pb(Zr_{0.53}Ti_{0.47})O_3$ thin film. (figure taken from [9])

2.4 Morphotropic Phase Boundary (MPB)

It has been known that the enhancement of dielectric and piezoelectric properties can be attributed to the phase instability, which can be induced either by compositional modification (i.e. morphotropic phase boundary, MPB) or by temperature variation (i.e. polymorphic phase transition, PPT). By definition, the MPB is a boundary in a composition-temperature phase diagram where two ferroelectric phases with different symmetry coexist in an equal quantity. At the MPB, an abrupt change in crystal structure is observed. In some cases, most notably for PZT, the boundary between the two phases is almost temperature independent [14, 19].

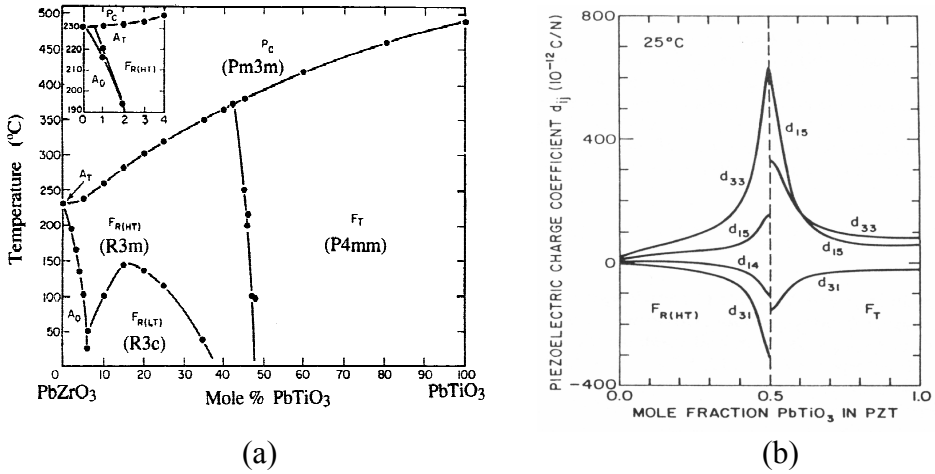

(a) (b)

Fig. 2.9 (a) Temperature-composition phase diagram of PZT showing MPB at x = 0.48 (after Jaffe *et. al*) (b) enhanced piezoelectric coefficient at MPB taken from [14]

The concept of the MPB is well known in lead zirconate titanate ($Pb(Zr_{1-x}Ti_x)O_3$, PZT) where an MPB between rhombohedral (*R3c*) on the lead zirconate ($PbZrO_3$) side and tetragonal (*P4mm*) on the lead titanate ($PbTiO_3$) side occurs at x = 0.48 as shown in Fig. 2.9 (a). At the MPB, an anomalously high dielectric constant, piezoelectric coefficient, and coupling factor are observed, as seen in Fig. 2.9 (b). This can be attributed to the coexistence of two phases at the MPB which gives rise to a large number of the thermodynamically equivalent polarization directions (total of 14 polarization directions, six from tetragonal <001> and eight from rhombohedral <111>). Analysis of the thermodynamics using Landau-Devonshire-Ginzburg theory also exhibited the anisotropic flattening of the Gibbs free energy profile at the MPB between rhombohedral and tetragonal of PZT, which leads to enhanced domain wall mobility [20].

Later discoveries ([21], [22], [23]) from both theoretical and experimental studies have revealed the existence of intermediate monoclinic phases (M_A, M_B, and M_C; space group *Cm*) between the rhombohedral (R) and tetragonal (T) phase, as shown in Fig. 2.10 (a). These monoclinic phases were believed to mediate a rotation from the [111] polarization direction within the rhombohedral phase to the [001] polarization direction within the tetragonal phase [24]. Recently, the study by Zhang *et al.* [25] revealed for the first time that there exists the phase boundary between the monoclinic M_A and M_B by using a combination of Rietveld refinement and pair distribution function analysis. This study has also revealed that the M_A phase is more benefit than M_B phase in terms of supporting the superior piezoelectric properties.

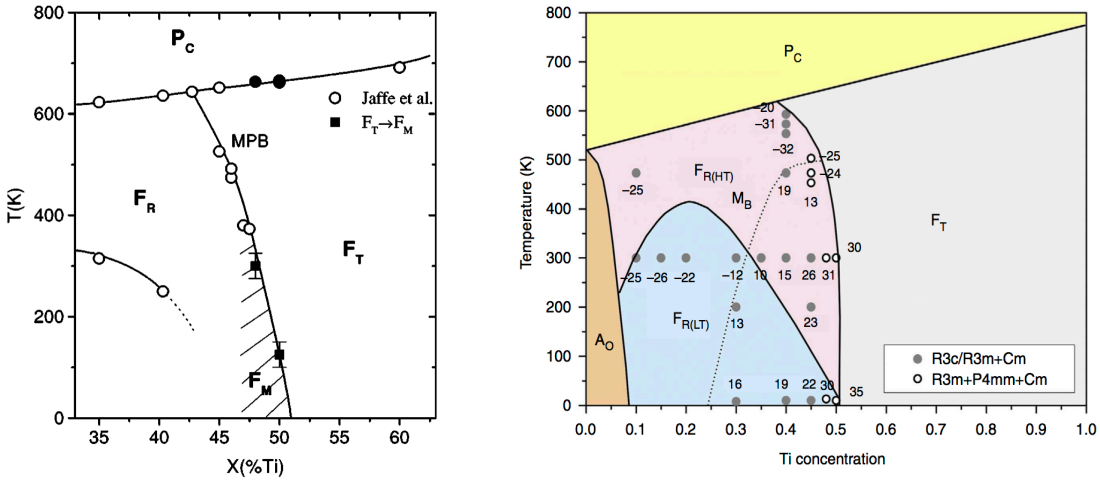

(a) (b)

Fig. 2.10 (a) Preliminary modification of the original PZT phase diagram by Noheda *et al.* [21] showing the monoclinic phase (F_M) between the rhombohedral (F_R) and the tetragonal phase (F_T) (figure taken from [21] (b) phase diagram from Zhang *et al.* [25] with the dotted line showing the phase boundary between the M_B and M_A monoclinic phase (figure taken from [25])

Superior piezoelectric properties at the composition near MPB have been found in other $PbMeO_3$-$PbTiO_3$ systems e.g. $(PbZn_{1/3}Nb_{2/3}O_3)_{1-x}$-$(PbTiO_3)_x$, (PZN-PT, with $x \approx 0.08$), $(PbMg_{1/3}Nb_{2/3}O_3)_{1-x}$-$(PbTiO_3)_x$, (PMN-PT, with $x \approx 0.35$), $(PbSc_{1/2}Nb_{2/3}O_3)_{1-x}$-$(PbTiO_3)_x$, and (PSN-PT, with $x \approx 0.43$). The MPB concept was also adopted in lead-free solid solutions where two end members with different crystal structure are selected to form solid solutions that have the MPB separating two crystal structures like that of lead-based systems e.g. the solid solutions of $(1-x)(Bi_{0.5}Na_{0.5})TiO_3$-$xBaTiO_3$ (MPB at $x \sim 0.06$-0.08 separating rhombohedral and tetragonal phases) and $(K_{0.5}Na_{0.5})NbO_3$–$BaTiO_3$ (MPB separating orthorhombic and tetragonal phases) [26].

It should be noted that the MPB could be divided into two types based on its temperature dependence. The first type is an MPB with minimal temperature dependence, i.e. a vertical line in a composition-temperature phase diagram, and the second type is a curved MPB as shown in Fig. 2.11 (a) and (b), respectively. The vertical MPB is more preferable than the curved type since the material properties in a vertical MPB remain close to the MPB during the temperature variation while that of curved MPB are moved away from the MPB. Thus, in real applications a material with a vertical MPB will have more stable properties over a wider temperature range.

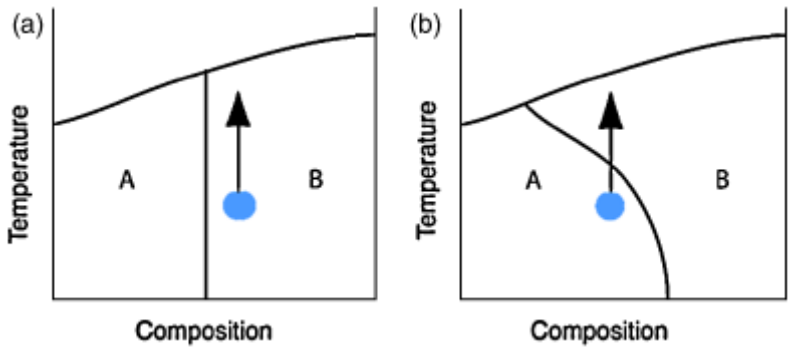

Fig. 2.11. Schematic diagrams show (a) Vertical MPB where the material's properties are stable throughout a wide temperature range (b) curved MPB (figure taken from [27])

2.5 Defect Chemistry

Defects are inevitable in the real world due to limitations of the chemical precursor purity and issues encountered during processing. By definition, any atomic-scale deviation from an ideal perfect crystal is called a defect. This includes grain boundaries, dislocations (i.e. line defects), and point defects. Grain boundaries and line defects gain less attention than point defects since they are not part of the equilibrium state of a crystal and the best understanding of them so far is mainly qualitative. Primarily, two types of point defects can occur in ionic crystals. One is a Frenkel defect, which is a displacement of an ion from its original site to a place that is not normally occupied (i.e. to an interstitial site). Another type is a Schottky defect, which is a simultaneous absence of both cations and anions from their normally occupied sites [8] [28]. For the perovskite structure where the packing density is quite high, it is very unlikely that Frenkel or interstitial defects will occur [14]. Understanding defects in

perovskite oxides is very crucial as they play an important role in controlling major properties including material hardening, softening, aging and fatigue as well as transport properties.

To describe a defect and its associated charge, Kroger-Vink notation is normally used. This notation system consists of: (1) *the main symbol*, indicates defect species; (2) *the subscript*, indicates the site that is replaced by defects; and (3) *the superscript*, which indicates the mismatch in charge of the defect with respect to the charge of the host ion. For example, if an ion with a lower valence (*A*, acceptor dopant) replaces the host ion (*B*) with higher valence, a negatively charged defect can be represented as A'_B, where the prime ($'$) indicates a relative negative charge. In contrast, if a substituting ion has higher valence (*D*, donor dopant) than the host ion, the defect can be represented as $D^{\cdot}_B$, where the dot ($^{\cdot}$) indicates a relative positive charge [28, 29].

2.5.1 Donor-, Acceptor-doping and Its Associated Defects

In perovskite oxide compounds e.g. $Pb(Zr_{0.5}Ti_{0.5})O_3$ and $BaTiO_3$, modifying electrical properties for different applications is normally done through doping with donor or acceptor dopants on either the A- or B-site. Typical donor and acceptor dopants used in $BaTiO_3$ and $Pb(Zr_{0.5}Ti_{0.5})O_3$ are shown in Table 2.1.

Table 2.1 Common aliovalent dopants in $Pb(Zr_{0.5}Ti_{0.5})O_3$ and $BaTiO_3$ [8]

A-site donors	La^{3+}, Bi^{3+}, Nd^{3+}
B-site donors	Nb^{5+}, Ta^{5+}, Sb^{5+}
A-site acceptors	K^{+}, Rb^{+}
B-site acceptors	Co^{3+}, Fe^{3+}, Sc^{3+}, Ga^{3+}, Cr^{3+}, Mn^{3+}, Mn^{2+}, Mg^{2+}, Cu^{2+}

For acceptor doping in which negatively charged defect is created, a positively charged defect is needed to compensate and maintain charge neutrality by one of three options: 1) cation interstitials, 2) anion vacancies or 3) holes. For example, an incorporation of acceptor Fe_2O_3 or CuO dopants into $PbTiO_3$ could result in compensating oxygen vacancies (i.e. ionic compensation) as follows:

$$Fe_2O_3 \xrightarrow{2PbTiO_3} 2Fe'_{Ti} + 3O_O^X + V_O^{\cdot\cdot} \tag{2.7}$$

$$CuO \xrightarrow{PbTiO_3} Cu''_{Ti} + O_O^X + V_O^{\cdot\cdot} \tag{2.8}$$

Apart from deliberately doping with acceptor dopants, oxygen vacancies could also be created in oxide compounds that contain volatile components e.g. Bi_2O_3, Na_2CO_3 in $(Bi_{0.5}Na_{0.5})TiO_3$ or PbO in $Pb(Zr_{0.5}Ti_{0.5})O_3$. At high sintering temperatures, the loss of this A-site volatile element will result in compensating oxygen vacancies as follows:

$$Pb_{Pb}^{X} + O_{O}^{X} \rightleftharpoons PbO(g) + V_{Pb}'' + V_{O}^{\cdot\cdot} \quad (2.9)$$

Similar to acceptor doping, the positively charge defects from donor doping could be compensated by one of three options: 1) anion interstitials, 2) cation vacancies and 3) electrons. Two examples of a cation-vacancy compensating defect (V_{Pb}'') after La_2O_3 doping on the A-site or Nb_2O_5 doping on the B-site of $PbTiO_3$ are shown in equation (2.10) and (2.11), respectively:

$$La_2O_3 \xrightarrow{2PbTiO_3} 2La_{Pb}^{\cdot} + 3O_{O}^{X} + V_{Pb}'' \quad (2.10)$$

$$Nb_2O_5 \xrightarrow{2PbTiO_3} 2Nb_{Ti}^{\cdot} + 5O_{O}^{X} + V_{Pb}'' \quad (2.11)$$

It should be noted that the above equations (i.e. (2.7) - (2.11)) are written based on an assumption that the composition is in equilibrium with the ambient atmosphere (i.e. oxygen activity) at a given temperature [28]. In the real system, the oxygen activity is typically too high or too low, which can occur either spontaneously during processing or deliberately by experimentally controlling the oxygen partial pressure. Consequently, the composition will gain or lose oxygen until a new equilibrium is reached. For example, if the oxygen activity is high (i.e. oxidizing atmosphere), the composition could gain oxygen back as follows [30]:

$$\frac{1}{2}O_2 + V_O^{\cdot\cdot} \leftrightharpoons O_O + 2h^{\cdot} \quad (2.12)$$

To incorporate oxygen back to the crystallographic site as an ion, the oxygen atom takes on two electrons from the valence band, leaving behind two holes that contribute to p-type conduction. Thus, a transition from ionic ($V_O^{\cdot\cdot}$) to p-type electronic ($h^{\cdot}$) compensation can be obtained.

In contrast, at low oxygen activity (i.e. reducing atmosphere), the oxygen ion will leave the crystal. Since oxygen needs to leave as a neutral atom, it leaves behind two electrons according to the following equation:

$$O_O^x \longrightarrow V_O^{\cdot\cdot} + 2e' + \frac{1}{2}O_2 \quad (2.13)$$

Thus, a transition from ionic to n-type electronic conduction will occur.

The type of compensating defects has a great influence on the transport properties of doped perovskite oxides. Depending upon whether the dominant defects are ionic or electronic, a difference in conductivity by many orders of magnitude could be observed.

2.6 Hardening and Softening

Apart from the excellent piezoelectric properties at the MPB, another reason that makes PZT the market-dominant piezoelectric material is the ability for its properties to

be adjusted for specific applications through cation doping. Typically, a small amount of dopants on the order of 1-2 at% could induce the materials properties to possess "soft" or "hard" characteristics.

Soft characteristics can be achieved by doping with donor dopants or higher valence cations on either the A- or B-site. Typical donor dopants used are La^{3+} on the A-site or Nb^{5+} on the B-site. Other donor dopants have also been reported as shown in Table 2.1. A substitution of this higher valence cation will result in a positively charged defect (e.g. $La_{Pb}^{\cdot}$, $Nb_{Ti}^{\cdot}$) and a compensating A-site vacancy (e.g. $V_{Pb}^{\prime\prime}$) as previously shown in equation (11) and (12). Regardless of the site that is being doped, the materials exhibit the same soft characteristics, which include improved electrical resistivity (low conductivity), an increase in the piezoelectric coefficients, dielectric constant (ε_r) and dielectric losses (tan δ) as well as a decrease in the mechanical quality factor (Q_m), coercive field (E_c) and aging effect [14, 31].

While the improvement in electrical resistivity was attributed to a compensation of the effects of naturally present acceptor cations and lead vacancies, the rest of the softening characteristics were attributed to higher domain wall mobilities [14]. Nevertheless, the reasons why domain wall mobility increases in soft materials are still controversial and many hypotheses have been proposed. A reduction of internal stress as a result of lead vacancy formation ($V_{Pb}^{\prime\prime}$) has long been suggested as a source of a higher domain wall mobility [32]. Another theory is based on the fact that donor dopants could compensate naturally present acceptor defects as well as lead vacancies, thus preventing the formation of compensating oxygen vacancies ($V_O^{\cdot\cdot}$). Since oxygen vacancies are

suspected to be responsible for domain wall pinning, a decrease of them leads to higher domain wall mobility. Recently, first-principle studies on $PbTiO_3$ by Chandrasekaran *et al.* [33] have suggested that a higher domain wall mobility in donor-doping is a result of lower concentration of oxygen vacancies, which is in agreement with previous theories and hypotheses.

Alternatively, hardening can be achieved by doping with acceptor dopants or lower valence cations (e.g. Fe^{3+} replacing Ti^{4+}/Zr^{4+} or K^{+} replacing Pb^{2+}). Acceptor doping causes the formation of negatively charged defects (e.g. Fe'_{Ti}) along with compensating oxygen vacancies ($V_O^{\cdot\cdot}$) as shown previously in equation (7). These mobile charged defects stabilize domain configurations, and subsequently lead to a decrease of domain wall contributions to the polarization response. Consequently, the materials show hardening characteristics, which include a moderately lowered electrical resistivity (i.e. high conductivity), a decrease in the piezoelectric coefficient, ε_r and tan δ, as well as an increase in Q_m and E_c and aging effects. Three mechanisms have been proposed as to the origin of the stabilized domain configurations: (1) *grain boundary effects* [34, 35], which is a diffusion of charged defects to grain boundaries, resulting in internal bias fields that pin polarization orientation; (2) *domain wall effects* [36, 37], which is an inhibition of domain wall movement as a result of the diffusion of charged defects to the domain wall area and (3) *volume or bulk effects* [38, 39], which is an alignment of defect dipoles along the spontaneous polarization (P_s) within domains.

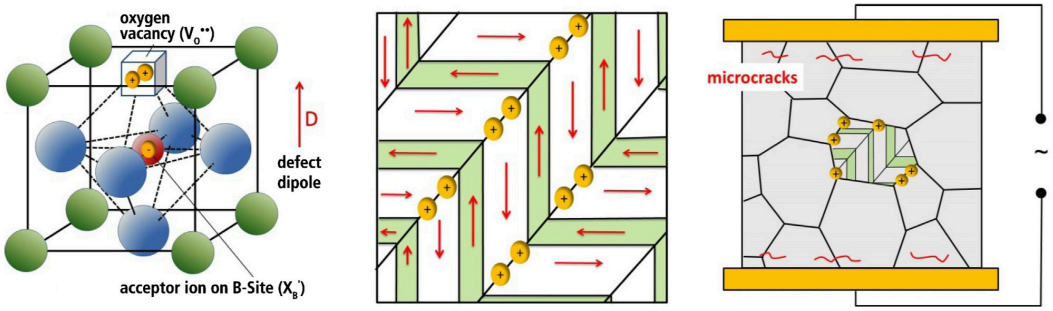

(a) Volume effect (b) Domain effect (c) Grain boundary effect

Fig. 2.12 Schematic illustration showing the proposed domain stabilization mechanisms, (a) volume effect, (b) domain effect and (c) grain boundary effect (figure taken from [40])

Among the proposed mechanisms, the most widely accepted one is the *volume effect* model. In this model, defect dipoles (e.g $Fe'_{Ti} - V_O^{\cdot\cdot}$) may randomly align along one of the possible directions when the sample is in its high temperature paraelectric cubic phase (Fig. 2.13 (a)). As the sample cools down to the paraelectric-ferroelectric phase transition, the defect dipoles will tend to align along the spontaneous polarization directions allowed by the symmetry of the phase in order to minimize their potential energy e.g <001> directions for the tetragonal phase (Fig. 2.13(b)) or <111> directions for the rhombohedral phase (Fig. 2.13(c)). This spontaneous realignment of the defect dipoles during the sample cooling through T_c is also known as the aging process. Aging time, which is the time that the defect dipoles need for aligning themselves along the P_s, is temperature dependent. For example, the aging time of $BaTiO_3$ is 5 days at 80 °C and 28 days at room temperature [41, 42].

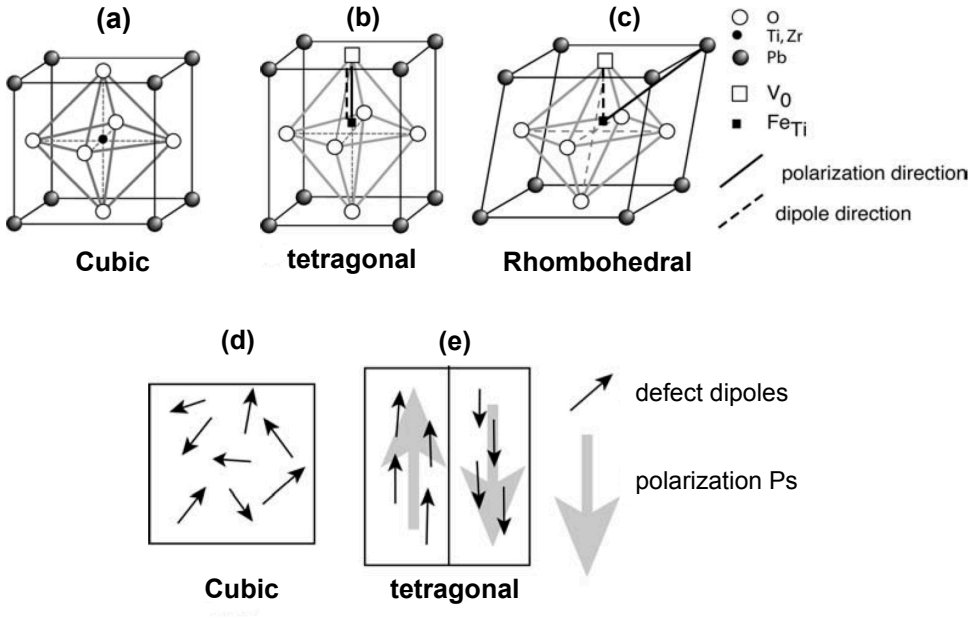

Fig. 2.13 Defect dipoles and spontaneous polarization (P_s) direction in (a) cubic, (b) tetragonal and (c) rhombohedral unit cell of a perovskite crystal. In (b) and (c), the *dotted* and *solid* line represent a defect dipole and a spontaneous polarization direction, respectively. Schematic representations exhibit corresponding defect dipoles and Ps in (d) cubic (randomly aligned) and (e) tetragonal (preferentially aligned along P_s) (figure adapted from [43])

For unpoled ceramics, aging will result in a pinched or constricted *P-E* hysteresis loop, as shown in Fig. 2.14 (b). This occurs because there is insufficient time for the defect dipole to reorient (at room temperature) through the displacement of oxygen vacancies. Therefore, under an alternating field, only the spontaneous polarizations can align with the electric field whereas the defect dipoles remain in their original positions (i.e. along P_s). When the electric field is removed, these defect dipoles will provide a restoring force that can bring back the spontaneous polarizations to their original state [44]. In contrast, if the ceramic is poled at high enough temperature (but below T_c) and at

electric field levels that are sufficient to reorient the P_s and defect dipoles, the shifting of whole *P-E* hysteresis under an alternating field will be observed, as shown in Fig. 2.14 (a). Deaging can be achieved by two ways: 1) by applying the alternating field to the ceramics hundreds of times or 2) by heating the ceramics beyond the transition temperature (T_c). After deaging, defect dipoles randomly align again; thus, the pinched P-E hysteresis loop becomes symmetric again due to an absence of the restoring force from aligned defect dipoles.

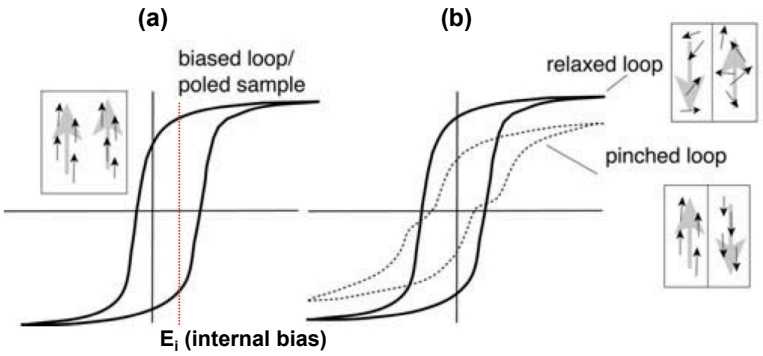

Fig. 2.14 *P-E* hysteresis loop in hard rhombohedral PZT ceramics (a) *P-E* loop of poled sample showing internal bias field (E_i) (b) a pinched loop in aged sample and a symmetric or relaxed loop after deaging (figure adapted from [43])

2.7 A-site and B-site ordering

In complex oxide systems, cation ordering on the sub-lattice site (A-site or B-site) could lead to a dramatic change in various key properties, e.g. dielectric/ferroelectric properties, conductivity, magneto-resistance, and magnetic behavior [45].

B-site ordering has been studied intensively in A($B'_xB''_{1-x}$)O_3 complex perovskites due to its strong relation to relaxor properties. Several interesting results have been found in lead-based Pb($B'_xB''_{1-x}$)O_3 perovskites where B' is typically a low valence cation e.g. Zn^{2+} ,Sc^{3+}, Mg^{2+} and B'' is a cation with higher valency e.g. Ti^{4+}, Nb^{5+}, Ta^{5+}. A suitable thermal treatment as well as the size and charge difference between B' and B''cation are important key factors for ordering.

Ordering in Pb($B'_xB''_{1-x}$)O_3 compounds can be divided into two groups based on charge electroneutrality. The first group is found in a 1:1 perovskite compounds e.g., Pb($Sc_{1/2}Ta_{1/2}$)O_3 (PST), and Pb($Sc_{1/2}Nb_{1/2}$)O_3 (PSN). In this group, the 1:1 ratio of B-site cation is accompanied by a 1:1 ordered nanodomain, resulting in a stoichiometric charge on B-site (4+). It was shown that the degree of ordering of compound in this group could change the dielectric behavior from relaxor to normal as shown in Fig. 2.15 (a), where the dielectric behavior of PST changes from a diffuse phase transition with frequency dependence (relaxor) to a sharp and frequency-independent (normal) behavior as the degree of ordering increased from 0.35 to 0.80 [46, 47].

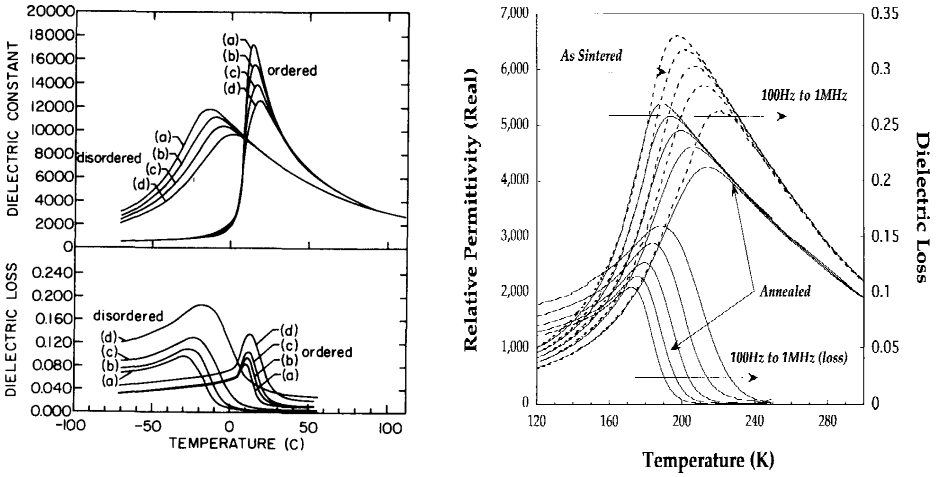

(a) (b)

Fig. 2.15 (a) Dielectric constant and loss in 1:1 perovskite (e.g. PST) showing a change from relaxor to a normal ferroelectric when a sample is induced from disordered (s = 0.35) to ordered state (s = 0.80) taken from [47] (b) Dielectric constant and loss in 1:2 perovskite (e.g. PMN) showing the persistence of relaxor behavior after annealing (figure taken from [36])

The second type of compounds has a 1:2 ratio of B' *to* B'' e.g $Pb(Mg_{1/3}Nb_{2/3})O_3$ (PMN), and $Pb(Mg_{1/3}Ta_{2/3})O_3$ (PMT). Instead of having stoichiometric 1:2 cation order as suggested in formula, the diffraction data revealed that the domain comprises of 1:1 ordered nanodomains, which results in a lower charge than expected (< 4+). Unlike 1:1 perovskite, it was found that the relaxor behavior in 1:2 perovskite compounds persists in all samples regardless of the degree of ordering. Due to the absence of domain growth after long annealing heat treatments, the "space charge" model was used to explain the observed ordering in many past studies. In this model, the B' *and* B'' sites in the negatively charged ordered nanodomain are occupied exclusively by B^{2+} and B^{5+}, respectively. And the net negative charge in ordered nanodomain must be compensated by an oppositely charge B^{5+}-rich disordered matrix in order to maintain charge neutrality.

However, this model was finally dismissed due to many reasons: (1) the lack of direct experimental evidence for compositional segregation, (2) the new discoveries of pronounced domain coarsening (> 95%) in PMT-PZ [48], PMN-PSN [49], and Tb-doped PMN [50] which is highly prohibited in space charge model since it leads to an unrealistic imbalance in charge.

An alternate explanation was proposed called the "random site" model where B'' is occupied solely by B^{5+} and B' is occupied by a random mixing of B^{2+} and the remaining B^{5+}. This model allows the domain to grow throughout the sample since the stoichiometry on the B-site is maintained in every region in the sample. Shown in Fig. 2.15 (b) [48] is a comparison of the dielectric permittivity between as-sintered and annealed PMT samples. It can be seen that the relaxor behavior in annealed sample still persists even though the ordered domain volume increases from ~20% to ~95% of overall volume. The random site model is widely accepted due to many reasons: (1) it allows the pronounced domain coarsening which was previously prohibited in the space charge model, (2) an insensitivity of the relaxor to the degree of ordering can be attributed to a localized-disordering on the B' site which is inherent in random site model and (3) several structure refinement results are in agreement with the random site model [51].

Studies of ordering on the A-site in perovskite compounds are rare compared to that of their B-site counterparts. However, it has been shown in the colossal magneto-resistive (CMR) manganite perovskites that A-site ordered samples resulted in a large increase in T_c from 270K for the disordered sample to 355 K for the A-site ordered one.

Moreover, it has been found in $La_{0.67-x}Li_{3x}TiO_3$ (x = 0.11) that the conductivity of the ordered sample is one order of magnitude lower than that of the disordered one [52].

2.8 Literature Review

2.8.1 Overview about BNT and BNT-BT

In the last 50 years, an A-site complex perovskite $(Bi_{0.5}Na_{0.5})TiO_3$ (BNT) has been the focus of great interest as a promising alternative to lead-based piezoceramics due to its excellent piezoelectric properties compared to other lead free piezoelectrics (e.g. high remanent polarization, P_r = 38 $\mu C/cm^2$, and high Curie temperature, T_c = 320 °C [53]).

However, BNT has a complicated crystal structure. Previously, it was reported as having a rhombohedral *R3c* structure at room temperature [54]. Recent high resolution x-ray diffraction data from Aksel *et al.* [55] and Gofman *et al.* [56] have suggested that the room temperature crystal structure to be a lower symmetry monoclinic *Cc* space group. In addition, there exists a discrepancy between the local structure as seen by various techniques (e.g. transmission electron microscopy (TEM) [57, 58], pair distribution function (PDF) analysis [59]) and the average long range structure obtained by neutron and synchrotron powder diffraction data [55]. This discrepancy was attributed to the complex in-phase and out-of-phase octahedral tilting [58] as well as a random distribution of Bi and Na [59].

Despite having many excellent piezoelectric properties, a high d_{33} value in pure BNT is hard to obtain due to the high coercive field (E_c = 73 kV/cm) and high

conductivity, which makes the poling process very difficult. Another drawback is the presence of the depolarization temperature (T_d) around 200°C which ultimately limits the working temperature of piezoelectric materials for many applications. In order to overcome these issues as well as to find an MPB with superior properties that match that of PZT, BNT was modified with doping or by making solid solutions with various end members, e.g. BNT-$BaTiO_3$ (BNT-BT) [26, 60, 61], BNT-$Bi_{0.5}K_{0.5}TiO_3$ (BNT-BKT) [62] and BNT-$NaNbO_3$ (BNT-NN) [63].

Among these modified materials, the solid solution (1-*x*)BNT-*x*BT has been the focus of many studies due to the existence of an MPB at compositions ~ x = 0.06 with superior piezoelectric properties along with a reduction in E_c as shown in Table 2.2.

Table 2.2. Dielectric and piezoelectric properties of BNT and BNT-based solid solutions (taken from [27])

System	$\epsilon_{33}^T/\varepsilon_0$ (1 kHz)	d_{33} (pC/N)	P_r ($\mu C/cm^2$)	E_c (kV/mm)	T_d (°C)	T_c/T_m (°C)	References
BNT	406 (Bi)*	94 (Bi)*	38	7.3	200	315-337	[14],[53]
BNT-xBT MPB x=6%-8%	601-826	122-176	37.8-40	2.72-3.41	90-105	225-288	[26, 60, 61]
BNT-2NN	624	88	27.8	5.67	~100	~300	[63]

*(Bi) denoted 0.3 wt% bismuth excess

Though superior piezoelectric properties were obtained in compositions near the MPB, one drawback was the shift in T_d from ~200°C (for pure BNT) to ~100°C (for compositions near the MPB). This effectively limits (1-*x*)BNT-*x*BT solid solutions even more for many applications. The lower T_d is indicative of a less stable ferroelectric which results in easier domain switching which dramatically enhances the piezoelectric properties at the MPB due to an ease of domain switching. The tradeoff between high piezoelectricity and low T_d is often encountered in Bi-based systems [64]. It was postulated that T_d features a phase transition from a ferroelectric state to an antiferroelectric because of the observation of constricted polarization hysteresis loops above this temperature. However, recent studies by Wook *et al.* [65] suggested that T_d was a result of an evolution of a coexistence of *R3c* and *P4bm* polar nanoregions (PNRs) at increasing temperature.

Since the first discovery in 1991 by Takenaka *et al*. [26], more than five phase diagrams of (1-*x*)BNT-*x*BT have been proposed and the equilibrium phases present in this system is still open for a discussion [26, 66-68]. This indicates that the crystal structure and the evolution of the crystal structure with temperature are quite complicated. Previous studies by transmission electron microscopy (TEM) together with dielectric measurements [66] give a common agreement for the unpoled state of (1-*x*)BNT-*x*BT that, for $x < 0.04$, the system has a rhombohedral structure with *R3c* space group. In the range of $0.5 < x < 0.7$, TEM data showed a core shell structure with a coexistence of rhombohedral *R3c* and tetragonal *P4bm* phases. For $x > 0.7$, the structure evolves into the tetragonal *P4bm* phase. Recent studies from TEM revealed a new phase boundary at x = 3-4% to be a mixing of *Cc/R3c* phase [69]. This result is in agreement

with the high resolution X-ray and neutron diffraction data from Usher *et al.* [70] in which a Rietveld refinement data suggested a *Cc* phase as the primary phase for x = 4%. Figure 2.16 (b) shows the updated phase diagram of (1-x)BNT-xBT, which includes the new *Cc* phase on the BNT-rich side of the diagram.

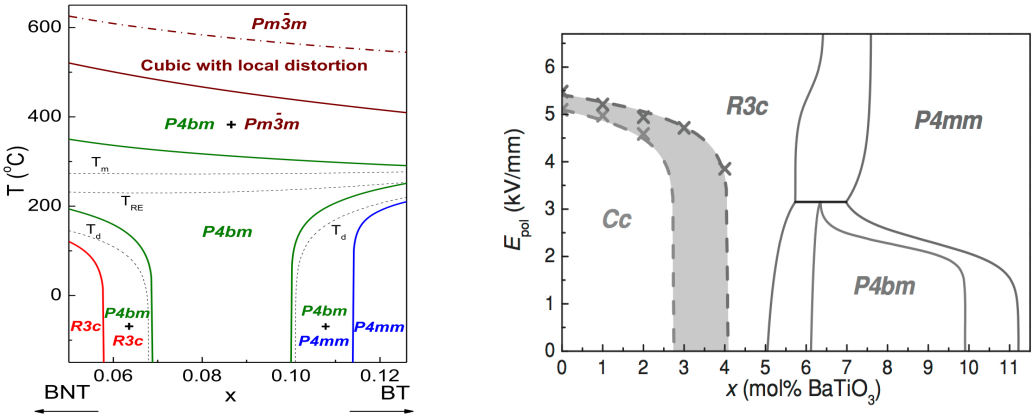

Fig. 2.16 (a) a phase diagram for (1-x)BNT-xBT [69] showing an MPB between *R3C* and *P4bm* phase at x ~ 0.055-0.07 and (b) the updated phase diagram of (1-x)BNT-xBT showing a new phase boundary *Cc*/*R3c* at x = 3-4% (figure adapted from [69]).

The structure at the MPB is also quite complex. Given that the BNT end member has rhombohedral symmetry and BT has tetragonal symmetry, the coexistence of rhombohedral and tetragonal phases at the MPB around x = 0.06-0.07 is not unexpected. However, recent and independent studies from both laboratory [71, 72] and high resolution X-ray diffraction [73, 74] experiments reported the crystal structure at the MPB to be pseudocubic. Local deviations from the average pseudocubic long range structure was also observed. For example, TEM studies [67, 68] revealed the local

structure of the x = 0.06 composition to be a mixture of complex domain (*R3c*) and nanodomain (*P4bm*) structures and that of the x = 0.07 composition included nanodomain features corresponding to *P4bm* symmetry. In addition, recent *in situ* TEM [75] results showed that the MPB (i.e. x = 5.5, 6 and 7%) was not stable under an applied electric field and the constituent (*R3c*) and (*P4bm*) phases can be created or destroyed. For example, for compositions at x = 5.5 and 6% BT, an initial MPB with co-existing *R3c* and *P4bm* phases completely transformed to pure *R3c* (i.e. the MPB was destroyed) through the phase transition sequence *P4bm* > *P4mm* > *R3c.*

2.8.2 A-site non-stoichiometric studies in (1-*x*)BNT-*x*BT

Since Bi and Na on the A-site are volatile elements, the A-site vacancies in BNT and BNT-BT are likely to be formed during sintering. This essentially makes the stoichiometry of the sintered compositions different from the expected stoichiometry. The effects of A-site non-stoichiometry on the physical, dielectric and piezoelectric properties as well as the crystal structure reported in the literatures are summarized below.

Hiruma *et al*. [76] studied the effect of Bi and Na non-stoichiometry according to the chemical formula $Bi_{0.5(1+x)}Na_{0.5}TiO_{3-0.75x}$ and $Bi_{0.5}Na_{0.5(1+y)}TiO_{3-0.75x}$, which is denoted as BNT-Bi(x), BNT-Na(y) and x,y = -0.01, -0.02 and 0.01. The results showed a decrease in dielectric loss (decreased conductivity) in samples that possessed either excess in Bi (e.g. BNT-Bi(0.01) or deficient in Na (e.g. BNT-Na(-0.01) BNT-Na(-0.02)). In contrast, an increase in dielectric loss (increased conductivity) was observed in samples that with either deficient in Bi (e.g. BNT-Bi(-0.01)) or excess in Na (e.g. BNT-Na(0.01)). Due to

an improvement of dielectric properties and a decrease in conductivity in samples with Bi/Na > 1.0 and a general degradation in dielectric properties for samples with Bi/Na < 1.0, it was proposed that Bi vaporization during the high sintering temperatures was the primary reason for the deteriorations in properties. Similarly, Zuo *et al*. [77] also reported the effects of A-site nonstoichiometry in BNT but in this study both Bi and Na were changed by the same amount (i.e. $(Bi_{0.5}Na_{0.5})_{1+x}TiO_3$ x = -0.02, -0.01, -0.005, 0, 0.005, 0.01). Samples with A-site deficiency resulted in relatively high dielectric loss and high conductivity compared to that of A-site cation excess samples. This confirmed that the A-site vacancies formed during sintering are responsible for the high conductivity of BNT ceramics. However, the ferroelectric properties were largely unaffected by the A-site nonstoichiometry since *P-E* hysteresis loops for both A-site deficient and A-site excess samples remained the same. Separate work from Sung *et al*. [78, 79] showed that T_d decreased in samples with excess Bi or deficient Na but increased in samples with deficient Bi or excess Na.

Recently, Li *et al.* [80, 81] reported a thorough study on the effect of Bi and Na non-stoichiometry in BNT by using impedance spectroscopy and other techniques. The impedance data revealed that BNT with excess Bi (i.e. $NBi_{0.51}T$) or deficient Na ($Na_{0.49}BT$) exhibited an increase in resistivity by 3-4 orders of magnitude. The dependence of the bulk resistivity on the pO_2 and the value of activation energy of 1.66 eV (~ ½ E_g) suggested n-type electronic conduction as the primary conduction mechanism for these highly insulating samples. In contrast, for samples with a deficiency in Bi ($NBi_{0.49}T$) or an excess in Na ($N_{0.51}BT$), a decrease in resistivity and a grain boundary resistivity that was a strong function of pO_2 as well as results from

electromotive force measurements revealed that the conduction mechanism was dominated by $V_O^{\cdot\cdot}$. Figure 2.17 (a) shows Arrhenius type plots of the bulk conductivity for resistive samples (i.e. samples with excess Bi or deficient Na, Bi/Na > 1.0) and conductive samples (i.e. samples with deficient Bi or excess Na, Bi/Na < 1.0).

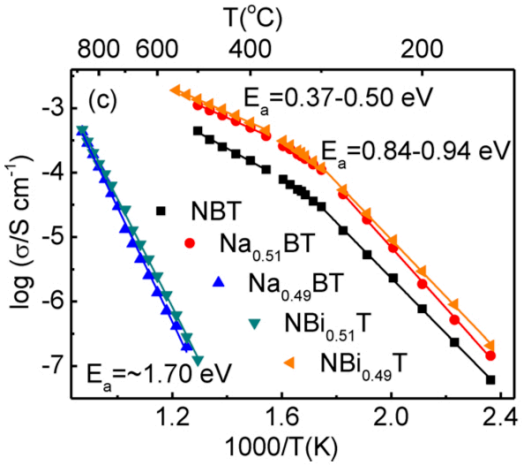

Fig. 2.17 Arrhenius type plots of bulk resistivity showing a similar behaviour between excess Bi and deficient Na sample (blue and green line, E_a ~ 1.70 eV). Similar conducting behaviour between deficient Bi and excess Na is also observed (orange and red line). (figure taken from [81])

These studies also highlighted the importance of the pre-drying step of the hygroscopic Na_2CO_3 starting reagent prior to processing. The adsorbed water in undried Na_2CO_3 powder has shown to result in a significant change in the stoichiometry of Na, and thus giving similar electrical properties to the Na-deficient sample.

There have been few studies on the effects of stoichiometry on the crystal structure of BNT. In one study, Spreitzer *et al*. [82] showed that a rhombohedral

distortion in pure BNT can be suppressed and became more cubic-like when the samples were Na-deficient.

2.8.3 B-site modification studies in (1-*x*)BNT-*x*BT

The previous section reviewed studies on A-site non-stoichiometry in pure BNT system which focused on the relationship between the non-stoichiometry, the properties and the loss of volatile elements during processing (e.g. Bi and Na). In considering the B-site, there have been a number of reports on the effects of acceptor doping. These studies have tried to investigate whether or not hardening characteristics, which have been successfully obtained in acceptor-doped PZT, can be achieved in BNT-based systems. Typical acceptor dopants used in PZT (e.g. Fe^{3+} and Mn^{3+}) were adopted in BNT-based systems and the results from the literatures are shown below.

Unlike PZT or $BaTiO_3$, acceptor-doped BNT-based solid solutions exhibit only a slight or moderate hardening. For example, Aksel *et al.* [83] studied the effect of Fe_2O_3 doping on the B-site in BNT and noted a slight increase in E_c as shown in Fig. 2.18 (a). This was attributed to the pseudocubic structure of BNT, which made almost no difference in the energy required for reorientation of defect dipole along all six oxygen octahedral sites. Jo *et al*. [84] also studied the effect of acceptor Fe-doped 92BNT-6BT-2KNN. However, due to the ergodic relaxor nature of this composition, which is characterized by a constricted *P-E* hysteresis loop, hardening characteristics like an increase in E_c or internal bias are difficult to resolve, as seen in Fig. 2.18 (b).

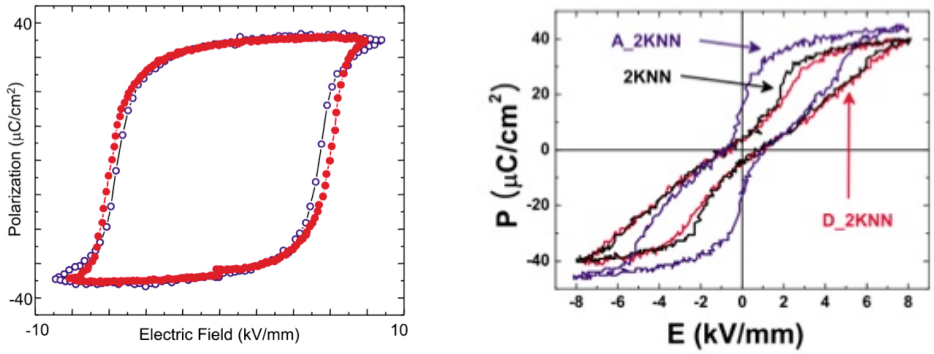

(a) (b)

Fig. 2.18 (a) Polarization hysteresis loops for undoped (blue) and 1% Fe-doped BNT (red) **(**taken from [83] and (b) polarization hysteresis loops of Fe doped 92BNT-6BT-2KNN (i.e. A_2KNN) (figure taken from [84])

In a study on Mn acceptor-doped 92BNT-8BT [85], an increase in Q_m was also observed. However, owing to a change in microstructure and density, it could not be concluded that the observed phenomena was the result of microscopic hardening (i.e. hardening due to the stabilized of domain by $V_O^{\cdot\cdot}$).

2.9 References

1. Megaw, H.D., *Crystal structure of double oxides of the perovskite type*. Proceedings of the Physical Society, 1946. **58**(2): p. 133.

2. Goodenough, J. and J. Longo, *Crystallographic and magnetic properties of perovskite and perovskite-related compounds*, 1970, Springer-Verlag: Berlin. p. 126-314.

3. Galasso, F.S., *Structure, properties, and preparation of perovskite-type compounds*. Vol. 5. 1969: Pergamon Press Oxfond.

4. Woodward, P.M., *Octahedral Tilting in Perovskites. I. Geometrical Considerations*. Acta Crystallographica Section B, 1997. **53**(1): p. 32-43.

5. Goldschmidt, V.M., *Die gesetze der krystallochemie*. Naturwissenschaften, 1926. **14**(21): p. 477-485.

6. Sleight, A.W. and R. Ward, *Compounds of Hexavalent and Pentavalent Uranium with the Ordered Perovskite Structure*. Inorganic Chemistry, 1962. **1**(4): p. 790-793.

7. Eitel, R.E., et al., *New high temperature morphotropic phase boundary piezoelectrics based on $Bi(Me)O_3$-$PbTiO_3$ ceramics*. Japanese Journal of Applied Physics, 2001. **40**: p. 5999.

8. Moulson, A.J. and J.M. Herbert, *Electroceramics: materials, properties, applications*. 2003: John Wiley & Sons.

9. Damjanovic, D., *Ferroelectric, dielectric and piezoelectric properties of ferroelectric thin films and ceramics*. Reports on Progress in Physics, 1998. **61**(9): p. 1267.

10. Shannon, R.t. and C.T. Prewitt, *Effective ionic radii in oxides and fluorides*. Acta Crystallographica Section B: Structural Crystallography and Crystal Chemistry, 1969. **25**(5): p. 925-946.

11. Cheng, J. and A. Navrotsky, *Enthalpies of formation of $LaBO_3$ perovskites (B= Al, Ga, Sc, and In)*. Journal of materials research, 2003. **18**(10): p. 2501-2508.

12. Cohen, R.E., *Origin of ferroelectricity in perovskite oxides*. 1992.

13. Safari, A. and E.K. Akdogan, *Piezoelectric and acoustic materials for transducer applications*. 2008: Springer.

14. Jaffe, B., *Piezoelectric ceramics*. Vol. 3. 1971: Academic press London and Newyork.

15. Dawber, M., K. Rabe, and J. Scott, *Physics of thin-film ferroelectric oxides*. Reviews of modern physics, 2005. **77**(4): p. 1083.

16. Jin, L., F. Li, and S. Zhang, *Decoding the fingerprint of ferroelectric loops: comprehension of the material properties and structures*. Journal of the American Ceramic Society, 2014. **97**(1): p. 1-27.

17. Nye, J.F., *Physical properties of crystals*. 1985: Clarendon press.

18. Zhang, X., et al., *Dielectric and piezoelectric properties of modified lead titanate zirconate ceramics from 4.2 to 300 K*. Journal of Materials Science, 1983. **18**(4): p. 968-972.

19. Haertling, G.H., *Ferroelectric ceramics: history and technology*. Journal of the American Ceramic Society, 1999. **82**(4): p. 797-818.

20. Damjanovic, D., *Contributions to the piezoelectric effect in ferroelectric single crystals and ceramics*. Journal of the American Ceramic society, 2005. **88**(10): p. 2663-2676.

21. Noheda, B., et al., *Tetragonal-to-monoclinic phase transition in a ferroelectric perovskite: The structure of* $PbZr_{0.52}Ti_{0.48}O_3$. Physical Review B, 2000. **61**(13): p. 8687.

22. Mishra, S., et al., *ARTICLES-Structure, structural phase transitions, mechanical properties, defects, etc.-Evidence for another low-temperature phase transition in tetragonal* $Pb(Zr_xTi_{1-x})O_3$ *(x = 0.515, 0.520)(6*. Physical Review-Section B-Condensed Matter, 2001. **64**(5): p. 54101-54101.

23. Ranjan, R., S. Mishra, and D. Pandey, *Room temperature structure of Pb(ZrTiO) around the morphotropic phase boundary region: A Rietveld study*. Journal of Applied Physics, 2002. **92**: p. 3266.

24. Vanderbilt, D. and M.H. Cohen, *Monoclinic and triclinic phases in higher-order Devonshire theory*. Physical Review B, 2001. **63**(9): p. 094108.

25. Zhang, N., et al., *The missing boundary in the phase diagram of* $PbZr_{1-x}Ti_xO_3$. Nature communications, 2014. **5**.

26. Takenaka, T., K.-I. Maruyama, and K. Sakata, $(Bi_{1/2}Na_{1/2})TiO_3$*–* $BaTiO_3$ *system for lead-free piezoelectric ceramics*. Japanese Journal of Applied Physics, 1991. **30**(9B): p. 2236-2239.

27. Rödel, J., et al., *Perspective on the Development of Lead-free Piezoceramics*. Journal of the American Ceramic Society, 2009. **92**(6): p. 1153-1177.

28. Smyth, D.M., *The defect chemistry of metal oxides*. The Defect Chemistry of Metal Oxides, by DM Smyth, pp. 304. Foreword by DM Smyth. Oxford University Press, Jun 2000. ISBN-10: 0195110145. ISBN-13: 9780195110142, 2000. **1**.

29. Kofstad, P. and T. Norby, *Defects and transport in crystalline solids*. University of Oslo, Oslo, 2007.

30. Smyth, D.M., *Defect structure in perovskite titanates*. Current Opinion in Solid State and Materials Science, 1996. **1**(5): p. 692-697.

31. Shrout, T.R. and S.J. Zhang, *Lead-free piezoelectric ceramics: Alternatives for PZT?* Journal of Electroceramics, 2007. **19**(1): p. 113-126.

32. Gerson, R., *Variation in ferroelectric characteristics of lead zirconate titanate ceramics due to minor chemical modifications*. Journal of Applied Physics, 1960. **31**(1): p. 188-194.

33. Chandrasekaran, A., et al., *Defect ordering and defect–domain-wall interactions in $PbTiO_3$: A first-principles study*. Physical Review B, 2013. **88**(21): p. 214116.

34. Takahashi, M., *Space charge effect in lead zirconate titanate ceramics caused by the addition of impurities*. Japanese Journal of Applied Physics, 1970. **9**(10): p. 1236.

35. Lupascu, D.C., Y.A. Genenko, and N. Balke, *Aging in ferroelectrics*. Journal of the American Ceramic Society, 2006. **89**(1): p. 224-229.

36. Warren, W.L., et al., *Electronic and ionic trapping at domain walls in $BaTiO_3$*. Journal of the American Ceramic Society, 1994. **77**(10): p. 2753-2757.

37. Warren, W., et al., *Electronic domain pinning in $Pb(Zr, Ti)O_3$ thin films and its role in fatigue*. Applied physics letters, 1994. **65**(8): p. 1018-1020.

38. Lambeck, P. and G. Jonker, *The nature of domain stabilization in ferroelectric perovskites*. Journal of Physics and Chemistry of Solids, 1986. **47**(5): p. 453-461.

39. Zhang, L. and X. Ren, *In situ observation of reversible domain switching in aged Mn-doped $BaTiO_3$ single crystals*. Physical Review B, 2005. **71**(17): p. 174108.

40. Genenko, Y.A., et al., *Mechanisms of aging and fatigue in ferroelectrics*. Materials Science and Engineering: B, 2015. **192**: p. 52-82.

41. Ren, X., *Large electric-field-induced strain in ferroelectric crystals by point-defect-mediated reversible domain switching*. Nature materials, 2004. **3**(2): p. 91-94.

42. Zhang, L., W. Chen, and X. Ren, *Large recoverable electrostrain in Mn-doped (Ba, Sr)TiO_3 ceramics*. Applied physics letters, 2004. **85**(23): p. 5658-5660.

43. Damjanovic, D., *Hysteresis in piezoelectric and ferroelectric materials*. The science of hysteresis, 2006. **3**: p. 337-465.

44. Zhang, L. and X. Ren, *Aging behavior in single-domain Mn-doped $BaTiO_3$ crystals: Implication for a unified microscopic explanation of ferroelectric aging*. Physical Review B, 2006. **73**(9): p. 094121.

45. Davies, P.K. and M.A. Akbas, *Chemical order in PMN-related relaxors: structure, stability, modification, and impact on properties*. Journal of Physics and Chemistry of Solids, 2000. **61**(2): p. 159-166.

46. Randall, C., et al., *Classification and consequences of complex lead perovskite ferroelectrics with regard to B-site cation order*. J. Mater. Res, 1990. **5**(4): p. 829-34.

47. Setter, N. and L. Cross, *The role of B-site cation disorder in diffuse phase transition behavior of perovskite ferroelectrics*. Journal of Applied Physics, 1980. **51**(8): p. 4356-4360.

48. Akbas, M.A. and P.K. Davies, *Domain growth in Pb ($Mg_{1/3}Ta_{2/3}$)O_3 perovskite relaxor ferroelectric oxides*. Journal of the American Ceramic Society, 1997. **80**(11): p. 2933-2936.

49. Farber, L., et al., *Cation Ordering in Pb ($Mg_{1/3}Nb_{2/3}$)O_3–Pb($Sc_{1/2}Nb_{1/2}$)O_3 (PMN–PSN) Solid Solutions*. Journal of the American Ceramic Society, 2002. **85**(9): p. 2319-2324.

50. Akbas, M.A. and P.K. Davies, *Thermally Induced Coarsening of the Chemically Ordered Domains in Pb($Mg_{1/3}Nb_{2/3}$)O_3 (PMN)-Based Relaxor Ferroelectrics*. Journal of the American Ceramic Society, 2000. **83**(1): p. 119-23.

51. Dmowski, W., et al., *Structure refinement of large domain relaxors in the Pb ($Mg_{1/3}Ta_{2/3}$)O_3–$PbZrO_3$ system*. Journal of Physics and Chemistry of Solids, 2002. **63**(1): p. 15-22.

52. Harada, Y., et al., *Order–disorder of the A-site ions and lithium ion conductivity in the perovskite solid solution $La_{0.67-x}Li_{3x}TiO_3$ (x = 0.11)*. Solid State Ionics, 1999. **121**(1): p. 245-251.

53. Smolenskii, G., et al., *New ferroelectrics of complex composition*. Sov. Phys. Solid State, 1961. **2**(11): p. 2651-2654.

54. Jones, G. and P. Thomas, *Investigation of the structure and phase transitions in the novel A-site substituted distorted perovskite compound $Na_{0.5}Bi_{0.5}TiO_3$*. Acta Crystallographica Section B: Structural Science, 2002. **58**(2): p. 168-178.

55. Aksel, E., et al., *Monoclinic crystal structure of polycrystalline $Na_{0.5}Bi_{0.5}TiO_3$*. Applied Physics Letters, 2011. **98**(15): p. 152901-152901-3.

56. Gorfman, S. and P. Thomas, *Evidence for a non-rhombohedral average structure in the lead-free piezoelectric material $Na_{0.5}Bi_{0.5}TiO_3$*. Journal of Applied Crystallography, 2010. **43**(6): p. 1409-1414.

57. Dorcet, V. and G. Trolliard, *A transmission electron microscopy study of the A-site disordered perovskite $Na_{0.5}Bi_{0.5}TiO_3$*. Acta Materialia, 2008. **56**(8): p. 1753-1761.

58. Levin, I. and I.M. Reaney, *Nano-and Mesoscale Structure of $NaBiTiO_3$: A TEM Perspective*. Advanced Functional Materials, 2012. **22**(16): p. 3445-3452.

59. Keeble, D.S., et al., *Bifurcated Polarization Rotation in Bismuth-Based Piezoelectrics*. Advanced Functional Materials, 2013. **23**(2): p. 185-190.

60. Chen, M., et al., *Structure and electrical properties of $(Na_{0.5}Bi_{0.5})_{1-x}Ba_xTiO_3$ piezoelectric ceramics*. Journal of the European Ceramic Society, 2008. **28**(4): p. 843-849.

61. Xu, C., D. Lin, and K. Kwok, *Structure, electrical properties and depolarization temperature of $(Bi_{0.5}Na_{0.5})TiO_3$-$BaTiO_3$ lead-free piezoelectric ceramics*. Solid state sciences, 2008. **10**(7): p. 934-940.

62. Yoshii, K., et al., *Electrical properties and depolarization temperature of $(Bi_{1/2}Na_{1/2})TiO_3$-$(Bi_{1/2}K_{1/2})TiO_3$ lead-free piezoelectric ceramics*. Japanese journal of applied physics, 2006. **45**: p. 4493.

63. Takenaka, T., T. Okuda, and K. Takegahara, *Lead-free piezoelectric ceramics based on $(Bi_{1/2}Na_{1/2})TiO_3$-$NaNbO_3$*. Ferroelectrics, 1997. **196**(1): p. 175-178.

64. Chu, B.-J., et al., *Electrical properties of $Na_{1/2}Bi_{1/2}TiO_3$-$BaTiO_3$ ceramics*. Journal of the European Ceramic Society, 2002. **22**(13): p. 2115-2121.

65. Jo, W., et al., *On the phase identity and its thermal evolution of lead free $(Bi_{1/2}Na_{1/2})TiO_3$-6 mol% $BaTiO_3$*. Journal of Applied Physics, 2011. **110**(7): p. 074106.

66. Ma, C., et al., *Domain structure-dielectric property relationship in lead-free (1-x)($Bi_{1/2}Na_{1/2}$)TiO_3- x$BaTiO_3$ ceramics*. Journal of Applied Physics, 2010. **108**(10): p. 104105-104105-8.

67. Ma, C. and X. Tan, *In situ Transmission Electron Microscopy Study on the Phase Transitionsin Lead-Free (1–x)($Bi_{1/2}Na_{1/2}$)TiO_3–x$BaTiO_3$ Ceramics*. Journal of the American Ceramic Society, 2011. **94**(11): p. 4040-4044.

68. Ma, C. and X. Tan, *Phase diagram of unpoled lead-free–ceramics*. Solid State Communications, 2010. **150**(33): p. 1497-1500.

69. Ma, C., H. Guo, and X. Tan, *A New Phase Boundary in ($Bi_{1/2}Na_{1/2}$)TiO_3–$BaTiO_3$ Revealed via a Novel Method of Electron Diffraction Analysis*. Advanced Functional Materials, 2013. **23**(42): p. 5261-5266.

70. Usher, T.-M., et al., *Crystal structure of 0.96($Na_{0.5}Bi_{0.5}TiO_3$)–0.04($BaTiO_3$) from combined refinement of x-ray and neutron diffraction patterns*. Applied Physics Letters, 2012. **101**(15): p. 152906.

71. Ranjan, R. and A. Dviwedi, *Structure and dielectric properties of ($Na_{0.5}Bi_{0.5}$)$_{1-x}Ba_xTiO_3$: $0 \le x \le 0.10$*. Solid state communications, 2005. **135**(6): p. 394-399.

72. Zhang, S.T., et al., *Temperature-Dependent Electrical Properties of 0.94$Bi_{0.5}Na_{0.5}TiO_3$–0.06$BaTiO_3$ Ceramics*. Journal of the American Ceramic Society, 2008. **91**(12): p. 3950-3954.

73. Daniels, J.E., et al., *Electric-field-induced phase transformation at a lead-free morphotropic phase boundary: Case study in a 93%($Bi_{0.5}Na_{0.5}$)TiO_3–7%$BaTiO_3$*. Applied Physics Letters, 2009. **95**(3): p. 032904-032904-3.

74. Simons, H., et al., *Electric-field-induced strain mechanisms in lead-free 94%($Bi_{1/2}Na_{1/2}$)TiO_3 – 6%$BaTiO_3$*. Applied Physics Letters, 2011. **98**(8): p. 082901.

75. Ma, C., et al., *Creation and Destruction of Morphotropic Phase Boundaries through Electrical Poling: A Case Study of Lead-Free ($Bi_{1/2}Na_{1/2}$)TiO_3-$BaTiO_3$ Piezoelectrics*. Physical Review Letters, 2012. **109**(10).

76. Hiruma, Y., H. Nagata, and T. Takenaka, *Thermal depoling process and piezoelectric properties of bismuth sodium titanate ceramics*. Journal of Applied Physics, 2009. **105**(8): p. 084112-084112-8.

77. Zuo, R., et al., *Influence of A-site nonstoichiometry on sintering, microstructure and electrical properties of ($Bi_{0.5}Na_{0.5}$)TiO_3 ceramics*. Materials Chemistry and Physics, 2008. **110**(2): p. 311-315.

78. Sung, Y., et al., *Effects of Na nonstoichiometry in ($Bi_{0.5}Na_{0.5+x}$)TiO_3 ceramics*. Applied Physics Letters, 2010. **96**(2): p. 022901-022901-3.

79. Sung, Y., et al., *Effects of Bi nonstoichiometry in ($Bi_{0.5+x}Na$)TiO_3 ceramics*. Applied Physics Letters, 2011. **98**(1): p. 012902.

80. Li, M., et al., *A family of oxide ion conductors based on the ferroelectric perovskite $Na_{0.5}Bi_{0.5}TiO_3$*. Nature materials, 2014. **13**(1): p. 31-35.

81. Li, M., Zhang, Huairuo, Zhang, Cook, Stuart N, Li, Linhao, Kilner John A, Reaney, Ian M, Sinclair, Derek C, *The dramatic influence of A-site non-stoichiometry on the electrical conductivity and conduction mechanisms in the perovskite oxide $Na_{0.5}Bi_{0.5}TiO_3$*. Chemistry of Materials, 2015. **27**: p. 629-634.

82. Spreitzer, M., M. Valant, and D. Suvorov, *Sodium deficiency in $Na_{0.5}Bi_{0.5}TiO_3$*. Journal of Materials Chemistry, 2007. **17**(2): p. 185-192.

83. Aksel, E., et al., *Defect structure and materials "hardening" in FeO-doped [BiNa]TiO ferroelectrics*. Applied Physics Letters, 2010. **97**: p. 012903.

84. Jo, W., et al., *Effect of Nb-donor and Fe-acceptor dopants in ($Bi_{1/2}Na_{1/2}$)TiO_3–$BaTiO_3$–($K_{0.5}Na_{0.5}$)NbO_3 lead-free piezoceramics*. Journal of Applied Physics, 2010. **108**(1): p. 014110-014110-6.

85. Zhu, M., et al., *Microstructure and Electrical Properties of MnO-Doped ($Na_{0.5}Bi_{0.5}$)$_{0.92}Ba_{0.08}TiO_3$ Lead-Free Piezoceramics*. Journal of the American Ceramic Society, 2007. **90**(1): p. 120-124.

3 Materials and Methods

Details about sample synthesis method and all the characterization techniques used in this research will be described in this chapter.

3.1 Materials Synthesis

All samples in this study were prepared by conventional solid-state synthesis methods. Reagent grade powders with the chemical purity listed in Table 3.1 were weighed according to the required chemical formula. It should be noted that the Na_2CO_3 powders were dried at 150°C for 10 h prior to weighing due to a concern regarding its hygroscopic nature. Failing to dry Na_2CO_3 precursor has been recently shown in BNT composition [1] to result in a significant change in electrical properties. Next, the powders were vibratory-milled by using 100% pure ethanol and high-density yttrium stabilized zirconia (YSZ) media (TOSOH corporation) for 6 hours followed by a drying step in a low temperature oven (~80°C) for at least 12 hours. The obtained powders were then calcined at 800°C for 2 hours followed by a re-milling and drying step in order to achieve sub-micron sized powder. The calcined powders were mixed with 3 wt% polyvinyl butyral (PVB) before uniaxially cold-pressing at 150 MPa to form a 12.7 mm diameter disc pellet. The pellets were sintered in a closed crucible at temperatures between 1150 to 1180°C for 2 h with a polymer burn out step at 400°C for 3 h with a

heating and cooling rate of 3°C/min. A covered crucible with a sacrificial powder of the same composition was used during sintering to minimize the loss of the volatile Bi and Na components.

Prior to making electrical measurements, samples were polished to obtain a smooth and parallel surface as well as to eliminate chemical inhomogeneity from a different degree of volatile element loss between surface and bulk. Typically, the samples are polished until the thickness is less than 1/10 of the diameter in order to prevent fringing effect. Then silver paste (Heraeus C1000) was applied on both sides and fired at 700 °C for 0.5 hours.

Table 3.1 Specification of oxide powders used in this research

Compound	**Purity**	**Supplier**
Bi_2O_3	99.9%	Sigma Aldrich
Na_2CO_3	99.95%	Alfa Aesar
TiO_2	99.9%	Sigma Aldrich
$BaCO_3$	99.8%	Alfa Aesar
ZnO	99.9%	Alfa Aesar
Ta_2O_5	99%	Alfa Aesar

3.2 Physical Properties and Structural Characterization

3.2.1 Structural Characterization

X-ray diffraction (XRD) was used to determine phase purity and crystal structure as well as the lattice parameters of both calcined powders and sintered ceramics. The room temperature diffraction patterns were collected by using Bruker AXS D8 diffractometer in the 2θ range of 20°-80° with a 0.01° increment and a scan speed of 1°/min. The source of X-ray is Cu-Kα radiation with a tube voltage and current of 40 kV and 40 mA, respectively. The peaks of the diffraction patterns were analyzed and matched with the database by using EVA software.

3.2.2 Inductively Coupled Plasma - Optical Emission Spectroscopy

To confirm the stoichiometry of the sintered samples, a high performance inductively coupled plasma-optical emission spectroscopy (ICP-OES) was performed on selected samples by using Perkin Elmer Optima 7300V equipped with WinLab32 ICP software Version 5.1.3.0550. Aqueous samples were prepared by mixing the ceramic powders with HNO_3 and HF acid in a high pressure Paar Bomb at 220 °C for 24 hours. Details about ICP-OES conditions used in this study are shown in Table 3.2 and the wavelength characteristics that were used for identified and quantified each element (Bi, Na, Ba and Ti) in the samples are shown in Table 3.3.

Table 3.2 Details about the ICP-OES operating conditions

ICP-OES conditions	
Nebulizer	Teflon GemCone
Spray Chamber	Cyclonic
RF power	1300 W
Ar Flow	15.0 L/min
Auxillary Ar Flow	0.2 L/min
Nebulizer Gas Flow	0.8 L/min

Table 3.3 Details about the wavelengths used for calculating the concentration of each element in the compositions

Element	**Wavelength (nm)***
Sc (as internal standard)	361.4, 424.7
Ba	233.5, 230.4, 413.1
Bi	223.1, 190.2, 306.8, 2222.8, 206.2
Na	589.6, 589.0
Ti	334.9, 336.1, 337.3, 334.9

*Reported value is an average of all wavelengths and has a relative standard deviation (RSD) of within 1%.

3.3 Electrical Properties Characterization

3.3.1 Dielectric properties

Dielectric measurements were carried out using an LCR meter (Agilent 4284A, Hewlett-Packard Inc.), which is capable of measuring the dielectric constant over the

frequency range of 100 Hz to 1 MHz. For low temperature dielectric measurements, the system was equipped with an environmental chamber (model 9023 Delta Design Inc.), which enables measurement temperatures between 150°C and -150°C. In contrast, high temperature dielectric measurements were conducted with an LCR meter equipped with a high temperature cell (NorECS ProboStat), which was designed to operate from room temperature up to 1,600°C. The heating and cooling rate during the measurement was 2 °C/min.

3.3.2 Ferroelectric properties

Polarization as a function of electric field (i.e. standard *P-E* hysteresis) measurements were carried out using a ferroelectric test system based on a Sawyer-Tower circuit (Precision Premier II, Radiant technology) utilizing Vision software. It should be noted that standard *P-E* hysteresis measurement captures sample's total response, including both remanent polarization and parasitics (e.g. linear capacitance, resistance, diode effects, leakage currents and etc.). The bipolar triangle waveform used for standard P-E hysteresis is shown in 3.1.

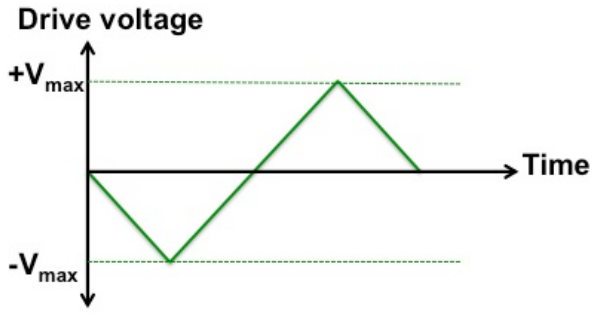

Fig. 3.1 Details of bipolar triangle waveform used in standard P-E hysteresis measurement [2]

To separate the ferroelectric from the non-ferroelectric contributions to the polarization response, Positive-Up-Negative-Down (PUND) test and remanent hysteresis measurement were employed. These two techniques exploit the fact that ferroelectric polarization remains unchanged after the applied electric field is removed [3]. Thus, in PUND test, when two consecutive electric pulses of the same polarity are applied (Fig. 3.2), both the ferroelectric and non-ferroelectric contributions will respond to the first pulse (i.e. total or switched polarization or *P**), while only non-ferroelectric contributions (i.e. non-switched polarization, *P*^) will respond to the second pulse [2]. Consequently, a subtraction of the non-switched polarization (*P*^) from the switched polarization (P*) gives rise to the switchable (or remanent) polarization ($\Delta P = P^* - P^\wedge$). For the remanent *P-E* hysteresis measurement, two consecutive half-triangular waves of the same polarity are used, as shown in Fig. 3.3.

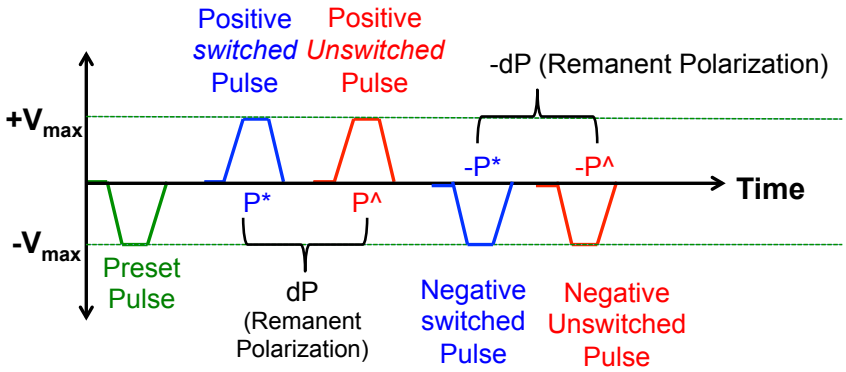

Fig. 3.2 Schematic representation of electrical profile used in PUND test showing two consecutive electric pulses in positive and negative direction. A subtraction of polarization response from switched and non-switched pulse gives rise to remanent polarization (ΔP)

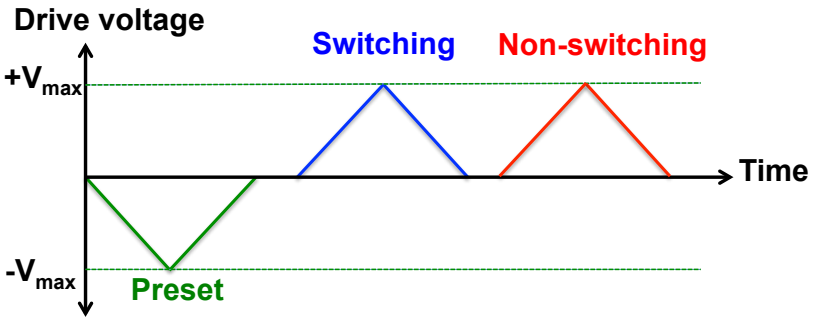

Fig. 3.3 Schematic representation of electrical profile used in remanent *P-E* hysteresis measurement showing two consecutive half-triangular electrical waves (picture adopt from [2])

3.3.3 Piezoelectric Properties

The mechanical quality factor (Q_m), which is inversely proportional to the mechanical loss factor (tan ϕ), was determined based on the method described in the IRE Standard [4]. The resonance/antiresonance peak was obtained by using an impedance gain/phase analyzer (Solartron SI1260A) and with SMaRT software (Solartron). The Q_m could be obtained by the following equation [4]:

$$\frac{1}{Q_m} = 2\pi f_r Z_m C \left(\frac{f_a^2 - f_r^2}{f_a^2}\right) \quad (3.1)$$

where, Z_m is the minimum impedance at the fundamental resonance frequency, f_r is fundamental resonance frequency, f_a is the antiresonance-frequency and C is the capacitance determined at 1 kHz.

The low field piezoelectric coefficient (d_{33}) was measured using the YE2730A (Sinoceramics) d_{33} meter. Prior to the Q_m and d_{33} measurements, all samples were poled by applying a dc electrical field of 60 kV/cm for 0.5 h at room temperature.

3.3.4 Resistivity Measurement

The bulk and grain boundary resistivity were measured using impedance spectroscopy (IS) technique. The measurements were conducted at different temperatures over the frequency range of 0.1 Hz to 5 MHz by using an impedance gain/phase analyzer (Solatron 1260A), which was equipped with Solatron 1296A dielectric interface in order to improve data accuracy at low frequencies. Before impedance measurements were carried out at each temperature step, the sample was held at temperature for 1 h to ensure temperature homogeneity. The output data were analyzed by using a combination of complex (Z^*) plane plot and the imaginary component of impedance (Z'') and electric modulus (M'') spectroscopic plots.

3.4 References

1. Li, M., Zhang, Huairuo, Zhang, Cook, Stuart N, Li, Linhao, Kilner John A, Reaney, Ian M, Sinclair, Derek C, *The dramatic influence of A-site non-stoichiometry on the electrical conductivity and conduction mechanisms in the perovskite oxide* $Na_{0.5}Bi_{0.5}TiO_3$. Chemistry of Materials, 2015. **27**: p. 629-634.

2. Technologies, R. *RT66A Analysis 2.1 User's Manual*.

3. Jaffe, B., *Piezoelectric ceramics*. Vol. 3. 1971: Academic press.

4. Jaffe, H., et al., *IRE standards on piezoelectric crystals: measurements of piezoelectric ceramics.* Proc. IRE, 1961. **49**: p. 1161-1169.

4 Crystal Structure and Electrical Properties of Complex Perovskite Solid Solutions Based on (1-*x*)$NaNbO_3$-*x*$Bi(Zn_{0.5}Ti_{0.5})O_3$

Sasiporn Prasertpalichat and David P. Cann

Materials Science, School of Mechanical Industrial and Manufacturing Engineering

Oregon State University

Corvallis, OR 97331

Published in December 2014 in

Journal of Electroceramics

Volume 33, Issue 3-4, page 214-220

4.1 Abstract

Ceramics based on the perovskite solid solution (1-x)$NaNbO_3$-$x$$Bi(Zn_{0.5}Ti_{0.5})O_3$ were prepared using conventional solid state synthesis. The crystal structure, electrical, and optical properties were examined. According to diffraction data, a single perovskite phase could be identified up to the composition x = 0.09. As the $Bi(Zn_{0.5}Ti_{0.5})O_3$ content increased the crystal structure transitioned from orthorhombic to pseudocubic symmetry. Furthermore, dielectric data showed that the dielectric maximum shifted to lower temperatures with the addition of $Bi(Zn_{0.5}Ti_{0.5})O_3$. Polarization hysteresis data revealed a slim linear loop across the whole range of solid solutions. Optical data also showed a decrease in the optical band gap from 3.4 eV for pure $NaNbO_3$ to 2.9 eV for the x = 0.09 composition. Using impedance spectroscopy, an electrically inhomogeneous microstructure was observed for compositions with increased $Bi(Zn_{0.5}Ti_{0.5})O_3$ content. Finally, the substitution of Ta on the B-site was shown to shift the dielectric maximum to temperatures as low as 100 K.

4.2 Introduction

Over the past ten years, a great deal of attention has been paid to search for alternatives to replace commercially used $Pb(Zr,Ti)O_3$ (PZT) piezoelectric ceramics due to an environmental concern regarding the toxicity of lead which not only a source of contamination during handling and processing, but also through exposure to aqueous biological solutions [1] or extreme chemical treatments [2]. Therefore, many systems

have been extensively studied e.g. $BaTiO_3$-based ceramics [3], $Bi_{0.5}Na_{0.5}TiO_3$-based materials [4, 5], Bi-layered structure materials [6] and alkaline niobate-based materials [7-9].

Among several alkaline niobate compounds, sodium niobate ($NaNbO_3$) is one of the more promising candidates due to its unique properties and a high dielectric constant ($\varepsilon_r \sim 2{,}000$-$3{,}000$) at the highest transition temperature at 360°C [10, 11]. Pure $NaNbO_3$ is one of the more complex perovskite materials that possesses six successive phase transitions from paraelectric cubic phase at high temperature (> 640°C) to antiferroelectric orthorhombic phase (*Pbma* or *Pbcm*) at room temperature (-100 to 360 °C) and a ferroelectric phase at low temperatures (< -100°C) [12, 13]. Also, $NaNbO_3$ can be an end member in many solid solutions including compounds such as $(K_{0.44}Na_{0.52}Li_{0.04})(Nb_{0.86}Ta_{0.10}Sb_{0.04})O_3$ [7] and $Na_{0.5}K_{0.5}NbO_3$ [7, 8] which possess comparable ferroelectric and piezoelectric properties to that of PZT.

$Bi(Zn_{0.5}Ti_{0.5})O_3$ (BZT) is an unstable perovskite at ambient temperature and pressure. However, recent study showed that it could be obtained under high pressure [14]. In $PbTiO_3$, alloying of $Bi(Zn_{0.5}Ti_{0.5})O_3$ resulted in an increase in both tetragonality (c/a = 1.11) and curie temperature (T_c > 700°C) [15]. In the previous work, solid solutions of $(1\text{-}x)NaNbO_3$-$xBi(Zn_{0.5}Ti_{0.5})O_3$, (1-*x*)NN-*x*BZT [16] were studied. The phase transition and dielectric properties as well as the effect of Li-doping were reported. However, the effects of the addition of BZT on other electrical properties and how it influences the crystal structure have not yet been reported in detail. In addition, while B-site doping with isovalent dopants such as Ta have been reported to dramatically improve

the properties in KNN [7], it has not been studied in this system. Therefore, in this study, solid solutions of (1-*x*)NN-*x*BZT will be studied in detail in order to fully understand the effect of BZT additions and the effects of B-site substitutions.

4.3 Experimental procedure

Bulk (1-*x*)$NaNbO_3$-*x*$Bi(Zn_{0.5}Ti_{0.5})O_3$ (abbreviated as (1-*x*)NN-*x*BZT) where x = 0.01, 0.03, 0.05, 0.07, 0.09 and 0.11 ceramic samples were prepared by a conventional solid state mixed oxide method by using reagent grade powder of Bi_2O_3 (99.9%), ZnO (99%), TiO_2 (99.9%), Na_2CO_3 (99.5%), Nb_2O_5 (99.9%) and Ta_2O_5 (99%). Prior to batching, Na_2CO_3 powder was dried at 150°C for 2 h due to the concern about hygroscopic. Raw materials were then batched according to a required stoichiometric ratio and ball-milled using ethanol and yttrium-stabilized zirconia as a media for 6 h. The dried powder was calcined at 920°C for 6 h followed by an additional milling and drying step in order to achieve sub-micron sized powder. The calcined powder was mixed with 3 wt% polyvinyl butyral (PVB) to increase the green strength and then uniaxially cold-pressed at 150 MPa to form a 12.7 mm diameter disc pellet. The polymer binder was burned out from the pellets at 400°C. Subsequently, the pellets were sintered at a temperature between 1,130 and 1,330°C for 2 h in a closed crucible with a sacrificial powder of the same composition to minimize bismuth loss.

The crystalline structure was examined using X-ray diffraction (XRD; Bruker-AXS D8) with a CuK_α source in a standard Bragg-Brentano geometry. The unit cell

volume was determined using the Le Bail mode in GSAS software. Prior to electrical measurements, the sintered pellets were polished until smooth and parallel surfaces were achieved and then silver paste (Heraeus C1000) was applied on both sides and finally fired at 700^{o}C for 0.5 h. Dielectric measurements were conducted over a wide temperature range (-150-600^{o}C) by using an Agilent 4284A LCR meter equipped with a NorECS ProboStat high temperature cell. For band gap determination, a diffuse reflectance measurement was conducted on a ground sintered pellet at room temperature with a UV visible spectrometer (Ocean Optics HR4000 UV-Vis). The Kubelka-Munk equation was utilized to obtain an optical absorbance curve which was subsequently analyzed to form a Tauc plot from which the band gap could be extrapolated.

4.4. Result and discussions

The theoretical density of (1-x)$NaNbO_3$-xBi($Zn_{0.5}Ti_{0.5}$)O_3 ceramics calculated from the XRD data ranged between 4.64 to 5.10 g/cm^3 for the compositions x = 0.01-0.09. All of (1-x)$NaNbO_3$-xBi($Zn_{0.5}Ti_{0.5}$)O_3 ceramics prepared in this study were sintered to high densities with geometry density (ρ) values measured between 4.3-4.6 g/cm^3 which is approximately ~90% of theoretical density. Figure 4.1 (a) illustrates the room temperature XRD patterns for all (1-x)NN-xBZT sintered samples with x = 0.01-0.11.

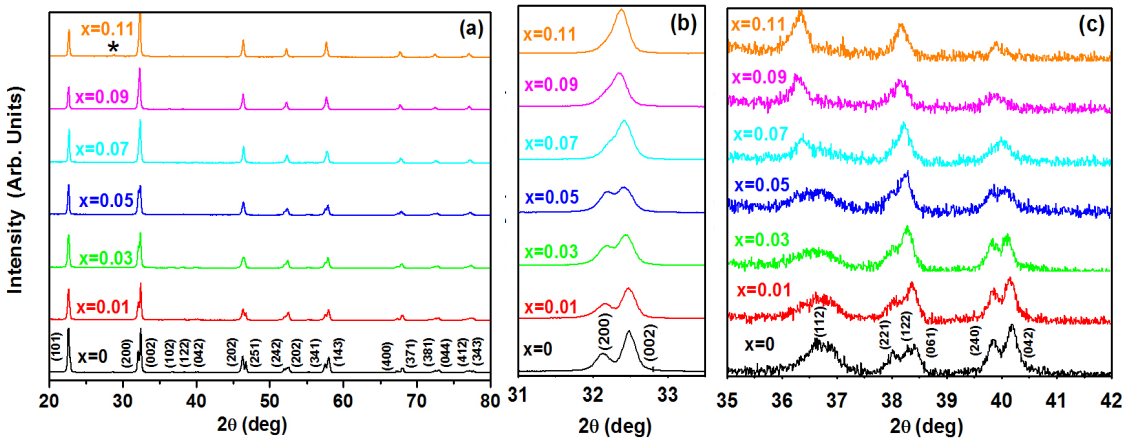

Fig. 4.1 (a) XRD data for (1-*x*)$NaNbO_3$-*x*$Bi(Zn_{0.5}Ti_{0.5})O_3$ sintered ceramics, (b) enlarged 2θ-region showing the {002} reflections and (c) enlarged 2θ-region showing the presence of orthorhombic reflections.

A single-phase perovskite was obtained for compositions up to $x = 0.09$ suggesting that $Bi(Zn_{0.5}Ti_{0.5})O_3$ successfully substitutes into the $NaNbO_3$ lattice to create a homogeneous solid solution of (1-*x*)$NaNbO_3$-*x*$Bi(Zn_{0.5}Ti_{0.5})O_3$. However, at the composition $x = 0.11$, a secondary phase was observed which was most likely a layered perovskite structured based on $Bi_5Nb_3O_{15}$. This suggests that the solubility limit of BZT in $NaNbO_3$ was close ~10 mol%. Regardless of the observation of a secondary phase, all ceramics adopted an orthorhombic perovskite structure from the $NaNbO_3$ parent phase and all peaks can be indexed according to JCPDS number 00-033-1270 (space group *Pbma*). Moreover, the (102), (122) and (042) diffraction peaks around 36° and 38° in the enlarged 2θ region shown in Fig. 4.1 (c) further confirm that the orthorhombic distortion of perovskite unit cell found in pure $NaNbO_3$ still persists in all (1-*x*)NN-*x*BZT solid solutions [17]. From an enlarged 2θ plot in Fig. 4.1 (b), it can be clearly seen that the (200) and (002) peaks gradually merge into one single broad peak at $x = 0.07$, indicating

that an introduction of BZT gradually changes the symmetry from orthorhombic to pseudo-cubic. Similar results were also observed in the $NaNbO_3$-$Bi_{0.5}Li_{0.5}TiO_3$ [18] and $NaNbO_3$-$Bi_{0.5}K_{0.5}TiO_3$ [19] systems as well.

Lattice parameters were extracted using the LeBail fitting method [20] in the GSAS software [21]. The space group used in this refinement was *Pbcm* [22]. The c-lattice parameter and unit cell volume as a function of *x* are shown in Fig 4.2 (a) and (b). It can be seen that c-axis parameter increased linearly up to $x = 0.07$ before it decreased sharply at $x = 0.09$. Similarly, the cell volume also increased linearly from $x = 0.01$ to $x = 0.05$ before exhibiting a sharp decrease at $x = 0.09$. The discrepancy in the trend may arise from the fact that the unit cell volume is also weighted by a- and b-axis lattice. An increase in c-axis lattice parameter and unit cell volume might be expected due to the larger average ionic radii of $Zn_{1/2}Ti_{1/2}$ (0.67 Å) compared to Nb^{5+} (0.64 Å) [23].

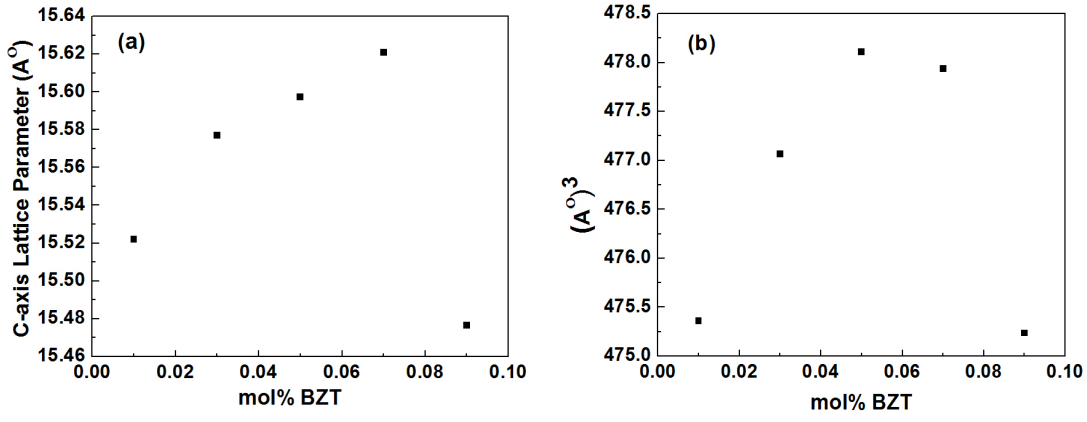

Fig. 4.2 (a) Diffraction data for c-axis lattice parameter and (b) unit cell volume for (1-*x)*NN-*x*BZT. Uncertainties are not indicated, but are less than the point size.

Figure 4.3 (a) shows the dielectric constant versus temperature at 10 kHz for (1-*x*)NN-*x*BZT ceramics from *x* = 0-0.09. Starting from *x* = 0 (pure NN), it was observed that the temperature of the dielectric maximum (T_{max}) for pure NN occurred around 347°C which is known to be a first-order phase transition from an antiferroelectric P (*Pbma*) phase to an antiferroelectric R (*Pmnm*) phase. Furthermore, this value agrees well with the previous studies where the dielectric anomaly from P to R phase was observed around 350-370°C [11, 24]. Instead of increasing T_c as was observed when BZT was added to$PbTiO_3$ in the $xPbTiO_3$-(1-*x*)$Bi(Zn_{0.5}Ti_{0.5})O_3$ [15] system, the addition of BZT in (1-*x*)NN-*x*BZT system resulted in a large shift in T_{max} from 296°C (for *x* = 0.01) down to to -83°C (for *x* = 0.09).

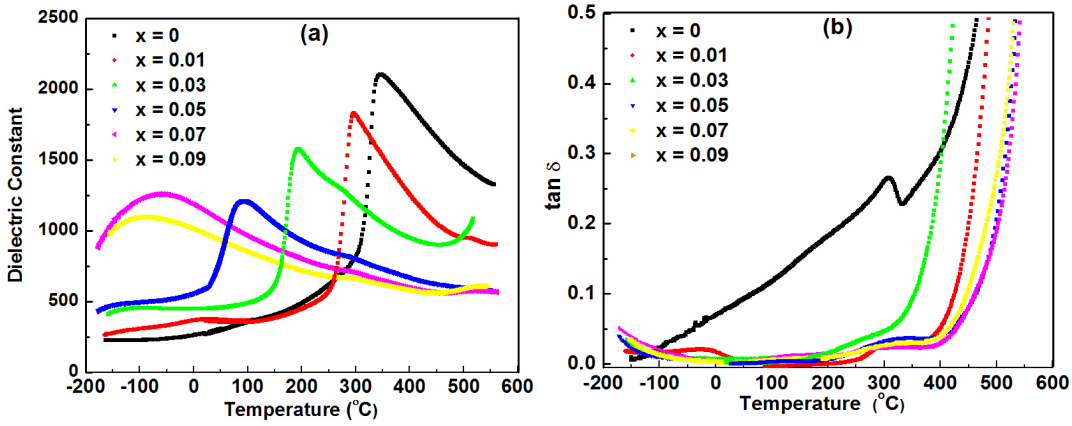

Fig. 4.3 (a) and (b) Temperature dependence of dielectric constant and dielectric loss for (1-*x*)NN-*x*BZT ceramics measured at 10 kHz

The effective ionic radii of substituting the charge compensated pair of Zn^{2+} (0.74 Å) and Ti^{4+} (0.605 Å) onto the B-site is 0.673 Å. Therefore, the shift in T_m as BZT was

added could be attributed to a weakening of the bonding in the B-site octahedral network after a substitution of a larger effective B-site ion (Zn^{2+}+Ti^{4+}, $r_{effective}$(0.673)) for Nb^{5+} ($r_{(Nb5+)}$ ~ 0.64 Å) [25]. The decrease in T_{max} has been observed in other perovskite systems including $Ba(Zr_xTi_{1-x})O_3$, $BiScO_3$-$Bi(Zn_{0.5}Ti_{0.5})O_3$-$BaTiO_3$ [26] and $NaNbO_3$-$Bi_{0.5}Li_{0.5}TiO_3$ [18]

Figure 4.4 shows the trend in T_{max} (determined from the maximum permittivity at 10 kHz) as a function of BZT content. According to Raevski and Prosandee, $NaNbO_3$-based solid solutions can be divided into two groups [27]. Group I is characterized by a smooth $T_{max}(x)$ dependence and a sharp dielectric maxima (ε_m). In contrast, group II $NaNbO_3$-based solid solutions have T_{max} (x) dependence that is smooth up to a threshold value of $x = x_0$. The value of x_0 varies from 5-20 mol% in most systems such as $NaNbO_3$-$BiFeO_3$ and $NaNbO_3$-$CaTiO_3$. One exception is $NaNbO_3$-$NaTaO_3$ where x_0 can be as high as 50 mol%. Moreover, the dielectric maxima for compositions with $x > x_0$ is highly frequency-dependent. Table 4.1 summarizes the threshold value x_0 for a range of solid solutions based on $NaNbO_3$ and other ABO_3 perovskites. According to Fig. 4.4, it can be seen that, T_{max} decreased linearly for compositions up to $x = 0.07$. Moreover, it can be seen that at $x = 0.07$ or higher, the dielectric maxima becomes dispersive. According to these two characteristic behaviors, we can conclude that (1-x)NN-xBZT belongs to group II with the threshold $x_0 = 0.07$.

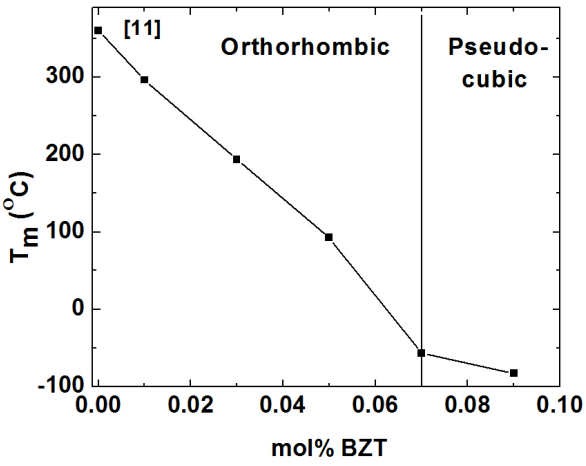

Fig. 4.4 Dielectric maximum temperature as a function of mol% BZT

Table 4.1 Summary of threshold values (x_0) for solid solutions based on $NaNbO_3$ and ABO_3

$NaNbO_3$-ABO_3 solid solutions	Threshold x_o
$NaNbO_3$-$Gd_{1/3}NbO_3$	~11 mol% [28]
$NaNbO_3$-$Na_{0.5}Bi_{0.5}TiO_3$	~12-15 mol% [29]
$NaNbO_3$-$SrTiO_3$	~15 mol% [30]
$NaNbO_3$-$NaTaO_3$	~50 mol% [31]

The dielectric properties as a function of frequency and temperature for (1-*x*)NN-*x*BZT is shown in Fig. 4.5. A sharp phase transition with no frequency dependence was clearly observed for $x = 0.01$. As x increased ($x = 0.05$) the transition peak broadened to a small degree but showed no frequency dependence, suggesting that a diffuse phase transition was induced after a moderate level of BZT additions. Finally, as x increased to

0.07 the transition peak became strongly dispersive and frequency-dependent, indicating the onset of relaxor-like behavior. The onset of relaxor-like behavior at x = 0.07 corresponds to the observation of change from orthorhombic to pseudo-cubic symmetry in the XRD data. The relaxor-like behavior could be attributed to the cation disorder since in this study both A-site and B-site are occupied by more than one cation [32].

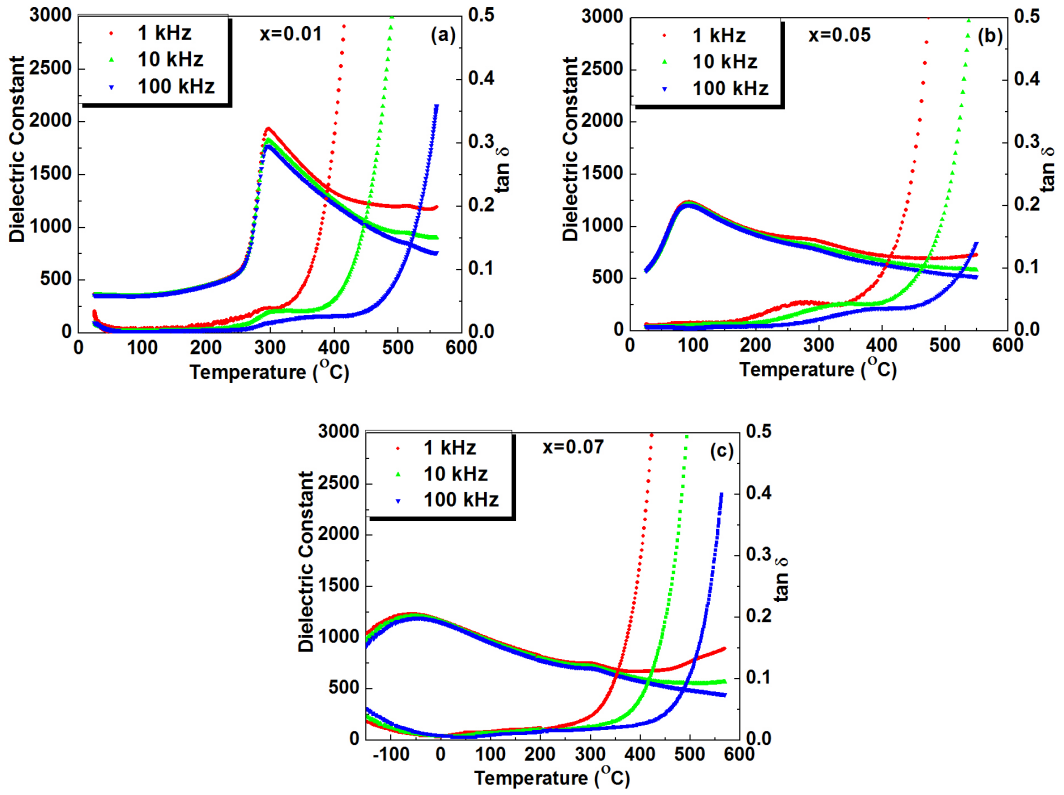

Fig. 4.5 Dielectric constant as a function of temperature measured on cooling at 1 kHz, 10 kHz and 100 kHz for (1-x)$NaNbO_3$-xBi($Zn_{0.5}Ti_{0.5}$)O_3 when (a) x = 0.01 (b) x = 0.05 and (c) x = 0.07

The diffuseness of transition peak can be described by the modified Curie-Weiss law [33]:

$$\frac{1}{\varepsilon} - \frac{1}{\varepsilon_m} = \left(T - T_{\varepsilon_m}\right)^{\gamma} / C_1 \qquad (4.1)$$

Where ε_m is the maximum value of dielectric constant, ε is a dielectric constant at temperature T, T_{ε_m} is the temperature at which the dielectric is maximum, γ is degree of diffuseness and ranging from 1 (for an ideal normal ferroelectric) to 2 (for an ideal relaxor ferroelectric) and C_1 is a Curie constant which is typically found to be on the order of 10^5 for a ferroelectric with a displacive phase transition [10]. Using the dielectric constant data at 1 kHz, the γ value can be determined from a slope of the plot between $\ln(1/\varepsilon - 1/\varepsilon_m)$ and $\ln(T - T_{\varepsilon_m})$. As seen from Table 4.2, the degree of diffuseness increased with increasing BZT content and dramatically shifted from 1.25 to 1.84 at the composition with 9 mol% BZT, confirming that the structure has transformed to relaxor behavior.

Table 4.2 Dielectric data for all compositions at 10 kHz

x mol% BZT	0.01	0.03	0.05	0.07	0.09
T_m (°C)	296	194	93	-57	-83
ε_m at T_m	1830	1580	1210	1220	1050
δ	1.25	1.48	1.54	1.68	1.84

Figure 4.6 shows the high field polarization data at room temperature for x = 0.01-0.09. It can be seen that the loop shows a linear response for all compositions. As expected from the dielectric data, the P_{max} value increased as x increased which closely matches the room temperature dielectric data shown in Fig. 4.3 (a).

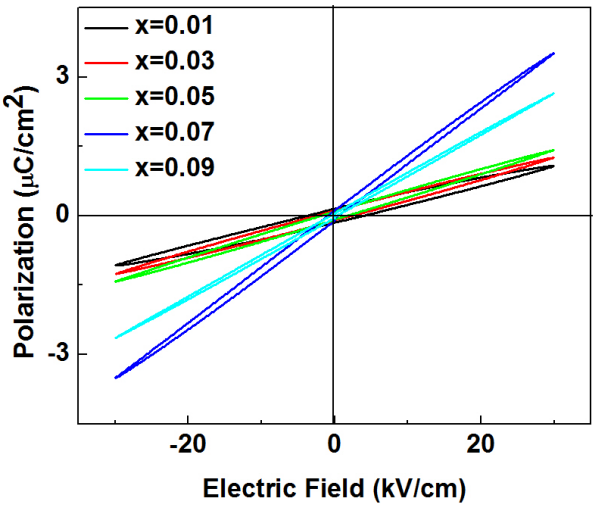

Fig. 4.6 The *P-E* hysteresis data measured at room temperature with a frequency of 1 Hz for a solid solutions of (1-*x*)NN-*x*BZT where x = 0.01-0.09

The optical absorption data for the (1-*x*)NN-*x*BZT ceramics in this study has been plotted in Fig. 4.7. By extrapolating the linear part of the Tauc plot, the band gap was obtained and is shown in Fig. 4.8. It can be seen that the addition of BZT resulted in a linear decrease in the band gap from 3.4 eV [34] for pure stoichiometric $NaNbO_3$ down to ~2.9 eV for the composition with 9 mol% BZT. It is known that the inter-band transition in $NaNbO_3$ is governed by an electronic transition from O-*2p* valence band to Nb*4d* conduction band [35, 36]. Therefore, the substitution of Bi on A-site and Zn and Ti on

the B-site are expected to perturb the electronic structure of the system. The narrower band gap might be attributed to an increase in unit cell volume since this can result in a distortion of unit cell and therefore a decrease in overlap between O-*2p* and metal (d^o) states [37].

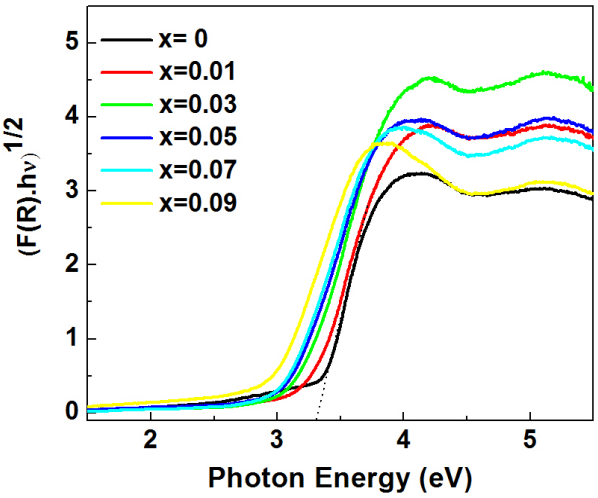

Fig. 4.7 Tauc plot showing optical absorption near band edge for (1-*x*)NN-*x*BZT where *x* = 0.00-0.09

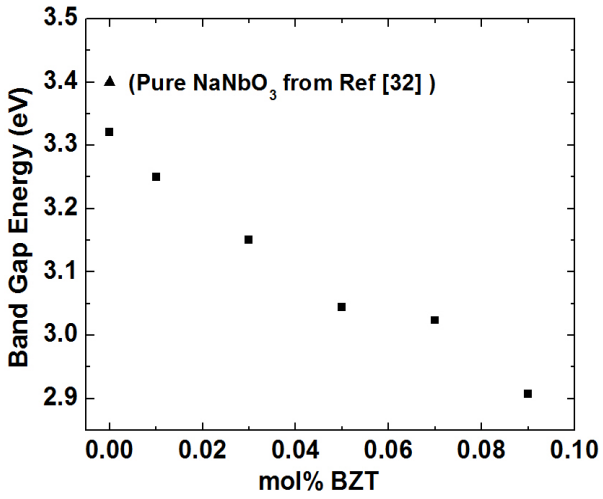

Fig. 4.8 Band gap energy as a function of composition of (1-*x*)NN-*x*BZT where *x* = 0-0.09

Figure 4.9 (a) and (b) shows the impedance data in both a complex plane plot and in a spectroscopic plot for the sample with *x* = 0.01. Similarly, Fig. 4.9 (c) and (d) show the same plots but with *x* = 0.07. The Z* plot for *x* = 0.01 (Fig. 4.9 (a)) deviated from a perfect circle as evidenced by a small semicircle at low frequency that was centered below the x-axis. This suggests that the *x* = 0.01 sample either possesses more than one relaxation time or the sample is not electrically homogeneous. This is also confirmed by the normalized spectroscopic plot in Fig. 4.9 (b) where the Z′′ curve does not completely overlap with the M′′ curve [38]. As x increased to 0.07, two phenomena have been observed as seen in Fig. 4.9 (c) and (d). First, the resistance is lower as seen from the x-intercept (Z′) and the Z″ peak maxima. Second, the electrical inhomogeneity is more pronounced as seen in complex plane plot where there is greater evidence of a semicircle at low frequency and also in the spectroscopic plot where the Z″ curve is broader.

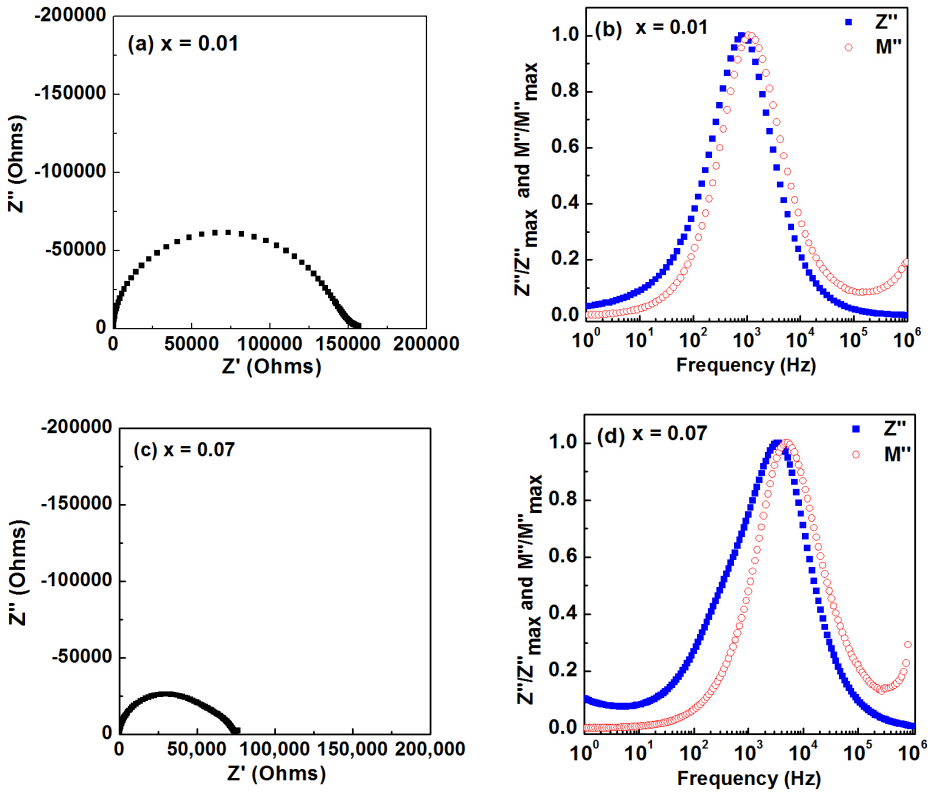

Fig. 4.9 Complex plane plots of (a) 0.99NN-0.01BZT and (c) 0.93NN-7BT Corresponding Z″ and M″ spectroscopic plots of (b) 0.99NN-0.01BZT and (d) 0.93NN-7BT (measured at 430°C)

In order to study the effect of replacing Ta^{5+} for Nb^{5+}, 0.93NN-0.07BZT was chosen as the base material and then 25 and 50 mol% of Ta was added. The plot in Fig. 4.10 (a) displays the temperature dependence of the dielectric constant and loss tangent measured at 10 kHz for $0.93Na(Nb_{1-y}Ta_y)O_3$-$0.07Bi(Zn_{0.5}Ti_{0.5})O_3$ where y = 0.25 and 0.50. In contrast to the Li^+ substitution for Na^+ on the A-site, the substitution of Ta on the B-site resulted in a decrease in T_{max} as seen in Fig. 4.10 (a) where the addition of 50 mol% Ta resulted in a shift of T_{max} to below -150°C. This is in agreement with the previous work from Torres-Pardo *et.al* [17] where Ta substitution for Nb in $NaNbO_3$

resulted in a decrease in T_{max} and from Lin *et al.* [9] where both T_c and T_{O-T} (orthorhombic to tetragonal transition temperature) decreased as the Ta content in $K_{0.5}Na_{0.5}(Nb_{(1-x)}Ta_x)O_3$ increased.

Fig. 4.10 (b) shows the polarization hysteresis (PE loop) data for 0.93NN-0.07BZT with 0 mol%, 25 mol% and 50 mol% Ta substituted. It can be seen that linear dielectric behavior is observed for 0 and 25% Ta. At 50 mol% Ta, it can be seen that the non-linear dielectric behavior was induced, which might be possibly due to presence of conduction losses.

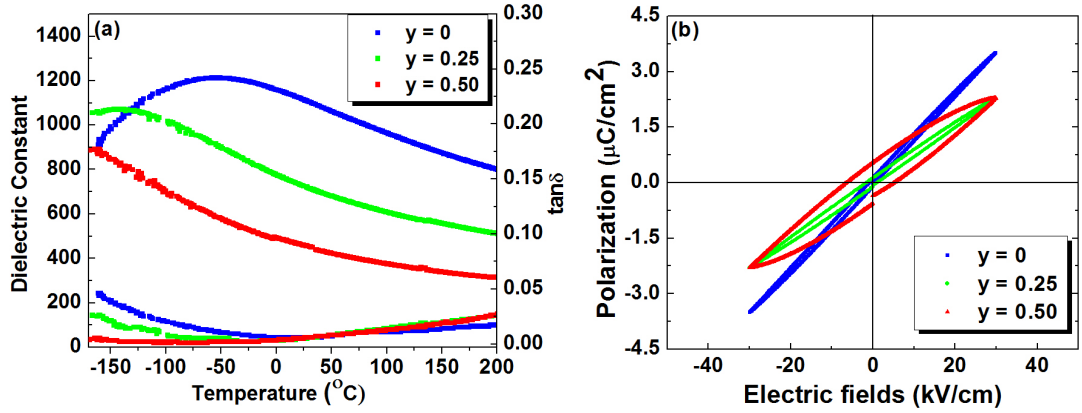

Fig. 4.10 (a) Dielectric Constant and tan δ as a function of temperature at a frequency of 10 kHz for $0.93Na(Nb_{1-y}Ta_y)O_3$-$0.07Bi(Zn_{0.5}Ti_{0.5})O_3$ (b) Room temperature polarization hysteresis data for $0.93Na(Nb_{1-y}Ta_y)O_3$-$0.07Bi(Zn_{0.5}Ti_{0.5})O_3$ at 1 Hz

4.5 Conclusion

Perovskite ceramics of the solid solution (1-x)$NaNbO_3$-xBi($Zn_{0.5}Ti_{0.5}$)O_3 with x = 0 to 0.11 were prepared. A single perovskite phase was observed up to x = 0.09 and a gradual change from orthorhombic to pseudocubic symmetry was also observed at x = 0.07. This suggests that the solubility limit should be between x = 0.07-0.09. The dielectric data showed a shift from a 1st order phase transition to a diffuse relaxor-like phase transition at x = 0.07. From optical data, it was shown that the optical band gap decreased from 3.3 eV to 2.9 eV over the range of compositions in this study. Impedance data also showed that the addition of BZT resulted in a more electrically heterogeneous microstructure. Finally, Ta substitution on the B-site resulted in a shift of T_m to lower temperature.

4.6 References

1. Foster, W.J., J.K. Meen, and D.A. Fox, *The effect of physiologic aqueous solutions on the perovskite material lead-lanthanum-zirconium titanate (PLZT): potential retinotoxicity*. Cutaneous and ocular toxicology, 2013. **32**(1): p. 18-22.

2. RoHs, E., *Directive 2002/95/EC,"Restriction of the use of certain hazardous substances in electrical and electronic equipment"*. Official Journal of the European Union, L, 2003. **37**: p. 19-23.

3. Yu, Z., et al., *Piezoelectric and strain properties of Ba ($Ti_{1-x}Zr_x$)O_3 ceramics*. Journal of applied physics, 2002. **92**(3): p. 1489-1493.

4. Takenaka, T., K.-I. Maruyama, and K. Sakata, *($Bi_{1/2}Na_{1/2}$)TiO_3–$BaTiO_3$ system for lead-free piezoelectric ceramics*. Japanese Journal of Applied Physics, 1991. **30**(9B): p. 2236-2239.

5. Safari, A. and M. Abazari, *Lead-free piezoelectric ceramics and thin films*. Ultrasonics, Ferroelectrics, and Frequency Control, IEEE Transactions on, 2010. **57**(10): p. 2165-2176.

6. Ikegami, S. and I. Ueda, *Piezoelectricity in ceramics of ferroelectric bismuth compound with layer structure*. Japan. J. Appl. Phys, 1974. **13**(10).

7. Saito, Y., et al., *Lead-free piezoceramics*. Nature, 2004. **432**(7013): p. 84-87.

8. Zuo, R., et al., *Phase transition and electrical properties of lead free ($Na_{0.5}K_{0.5}$)NbO_3–$BiAlO_3$ ceramics*. Journal of Alloys and Compounds, 2009. **476**(1): p. 836-839.

9. Lin, D., K. Kwok, and H. Chan, *Phase transition and electrical properties of ($K_{0.5}Na_{0.5}$)($Nb_{1-x}Ta_x$)O_3 lead-free piezoelectric ceramics*. Applied Physics A, 2008. **91**(1): p. 167-171.

10. Jona, F., *G. Shirane, Ferroelectric Crystals*. Dover P ub lications, Inc., New York, 1962. **199**(3): p. 3.

11. Shirane, G., R. Newnham, and R. Pepinsky, *Dielectric Properties and Phase Transitions of $NaNbO_3$ and (Na,K)NbO_3*. Physical Review, 1954. **96**(3): p. 581.

12. Megaw, H.D., *Ferroelectricity in crystals*. 1957.

13. Darlington, C. and K. Knight, *High-temperature phases of $NaNbO_3$ and $NaTaO_3$*. Acta Crystallographica Section B: Structural Science, 1999. **55**(1): p. 24-30.

14. Suchomel, M.R., et al., *Bi_2ZnTiO_6: A lead-free closed-shell polar perovskite with a calculated ionic polarization of 150 μC/cm^2*. Chemistry of materials, 2006. **18**(21): p. 4987-4989.

15. Suchomel, M.R. and P.K. Davies, *Enhanced tetragonality in (x)$PbTiO_3$-(1-x)Bi($Zn_{1/2}Ti_{1/2}$)O_3 and related solid solution systems*. Applied Physics Letters, 2005. **86**(26): p. 262905-262905-3.

16. Huang, C.-C., et al., *Phase Transitions and Dielectric Properties in Bi($Zn_{1/2}Ti_{1/2}$)O_3–($Na_{1-y}Li_y$)NbO_3 Perovskite Solid Solutions*. Japanese Journal of Applied Physics, 2009. **48**(3R): p. 031401.

17. Torres-Pardo, A., et al., *Phase coexistence in $NaNb_{(1-x)}Ta_xO_3$ materials with enhanced dielectric properties*. Journal of Materials Chemistry, 2012. **22**(30): p. 14938-14943.

18. Fu, L., et al., *Phase transition, dielectric and piezoelectric properties of $NaNbO_3$–$Bi_{0.5}Li_{0.5}TiO_3$ lead-free ceramics*. Current Applied Physics, 2012. **12**(6): p. 1523-1528.

19. Lin, D. and K.W. Kwok, *Ferroelectric and piezoelectric properties of new $NaNbO_3$–$Bi_{0.5}K_{0.5}TiO_3$ lead-free ceramics*. Journal of Materials Science: Materials in Electronics, 2010. **21**(10): p. 1060-1065.

20. Le Bail, A., H. Duroy, and J. Fourquet, *Ab-initio structure determination of $LiSbWO_6$ by X-ray powder diffraction*. Materials Research Bulletin, 1988. **23**(3): p. 447-452.

21. Larson, A.C. and R.B. Von Dreele, *Gsas*. General Structure Analysis System. LANSCE, MS-H805, Los Alamos, New Mexico, 1994.

22. Koruza, J., et al., *Phase transitions of sodium niobate powder and ceramics, prepared by solid state synthesis*. Journal of Applied Physics, 2010. **108**(11): p. 113509.

23. Shannon, R.t., *Revised effective ionic radii and systematic studies of interatomic distances in halides and chalcogenides*. Acta Crystallographica Section A: Crystal Physics, Diffraction, Theoretical and General Crystallography, 1976. **32**(5): p. 751-767.

24. Sakowski-Cowley, A., K. Lukaszewicz, and H.D. Megaw, *The structure of sodium niobate at room temperature, and the problem of reliability in pseudosymmetric structures*. Acta Crystallographica Section B: Structural Crystallography and Crystal Chemistry, 1969. **25**(5): p. 851-865.

25. Kuang, S., et al., *Influence of Zr dopant on the dielectric properties and Curie temperatures of Ba (ZrxTi 1− x) O 3 (0≤ x≤ 0.12) ceramics*. Scripta Materialia, 2009. **61**(1): p. 68-71.

26. Huang, C.-C., et al., *Phase transitions and ferroelectric properties in $BiScO_3$-$Bi(Zn_{1/2}Ti_{1/2})O_3$-$BaTiO_3$ solid solutions*. Journal of Applied Physics, 2007. **102**(4): p. 044103.

27. Raevski, I.P. and S.A. Prosandeev, *A new, lead free, family of perovskites with a diffuse phase transition: NaNbO3-based solid solutions*. Journal of Physics and Chemistry of Solids, 2002. **63**(10): p. 1939-1950.

28. Titov, V.V., et al., *Studies of Domain and Twin Patterns in $NaNbO_3$-$Gd_{1/3}NbO_3$ Solid Solution Crystals*. Ferroelectrics, 2008. **374**(1): p. 58-64.

29. Raevskaya, S., et al., *Structural and Dielectric Studies of $NaNbO_3$-$A_{0.5}Bi_{0.5}TiO_3$ (A-Li, Na, K) Solid Solutions*. Ferroelectrics, 2010. **399**(1): p. 27-34.

30. Glaister, R., *Solid solution dielectrics based on sodium niobate*. Journal of the American Ceramic Society, 1960. **43**(7): p. 348-353.

31. Hiroshi, I., Review of the Electrical Communication Laboratory, 1964. **12**: p. 469-487.

32. Setter, N. and L. Cross, *The role of B-site cation disorder in diffuse phase transition behavior of perovskite ferroelectrics*. Journal of Applied Physics, 1980. **51**(8): p. 4356-4360.

33. Uchino, K., et al., *Electrostrictive effect in lead magnesium niobate single crystals*. Journal of Applied Physics, 1980. **51**(2): p. 1142-1145.

34. Cross, L.E. and B.J. Nicholson, *LV. The optical and electrical properties of single crystals of sodium niobate*. The London, Edinburgh, and Dublin Philosophical Magazine and Journal of Science, 1955. **46**(376): p. 453-466.

35. Kato, H., H. Kobayashi, and A. Kudo, *Role of Ag^+ in the band structures and photocatalytic properties of $AgMO_3$ (M: Ta and Nb) with the perovskite structure*. The Journal of Physical Chemistry B, 2002. **106**(48): p. 12441-12447.

36. Eng, H.W., et al., *Investigations of the electronic structure of d^0 transition metal oxides belonging to the perovskite family*. Journal of Solid State Chemistry, 2003. **175**(1): p. 94-109.

37. Aguiar, R., et al., *The vast colour spectrum of ternary metal oxynitride pigments*. Dyes and Pigments, 2008. **76**(1): p. 70-75.

38. Raengthon, N., et al., *Defect mechanisms in high resistivity $BaTiO_3$–Bi ($Zn_{1/2}Ti_{1/2}$) O_3 ceramics*. Applied Physics Letters, 2012. **101**(11): p. 112904.

5 Hardening in Non-stoichiometric (1-*x*)$Bi_{0.5}Na_{0.5}TiO_3$-*x*$BaTiO_3$ Lead Free Piezoelectric Ceramics

Sasiporn Prasertpalichat and David P. Cann

Materials Science, School of Mechanical Industrial and Manufacturing Engineering

Oregon State University

Corvallis, OR 97331

Submitted to

Journal of Applied Physics

Manuscript ID: JR15-1461

5.1 Abstract

The role of A-site non-stoichiometry was investigated in lead-free piezoelectric ceramics based on compositions in the 1-x($Bi_{0.5}Na_{0.5}TiO_3$)-$x$$BaTiO_3$ system near the morphotropic phase boundary where x = 0.055, 0.06 and 0.07. Donor-doping was introduced through the addition of excess Bi, however there were no changes in the crystal structure. In contrast, acceptor doping was introduced through the addition of excess Na and was found to promote rhombohedral distortions. A significant improvement of dielectric properties was observed in donor-doped compositions and, in contrast, a degradation in properties was observed in acceptor-doped compositions. Compared to the stoichiometric composition, the acceptor-doped compositions displayed a significant increase in coercive field (E_c) which is an indication of domain wall pinning as found in hard $Pb(Zr_xTi_{1-x})O_3$. This result was further confirmed via polarization hysteresis studies including PUND tests and remanent *P-E* hysteresis analyses. Moreover, all A-site acceptor-doped compositions also exhibited an increase in mechanical quality factor (Q_m) as well as a decrease in piezoelectric coefficient (d_{33}), dielectric loss (tan δ), remanent polarization (P_r) and dielectric permittivity, which are all the typical characteristics of the effects of "hardening". The mechanism for the observed hardening in A-site acceptor doped BNT-based systems is linked to changes in the long-range domain structure and defect chemistry.

5.2 Introduction

Lead zirconate titanate ($Pb(Zr_xTi_{1-x})O_3$, PZT) ceramics are the most widely used piezoelectric materials due to not only its excellent dielectric and piezoelectric properties at the morphotropic phase boundary (MPB) but also its ability for its properties to be fine tuned via chemical doping with various elements. In PZT, donor doping or doping with higher valence ions on either the A- or B-site (e.g. Bi^{3+}/La^{3+} replacing Pb^{2+} or Sb^{5+}/Nb^{5+} replacing Zr^{4+}/Ti^{4}) has been shown to result in a "softening" which is typically characterized by an increase in piezoelectric activity, an increase in dielectric constant (ε_r) and loss ($\tan\delta$), as well as a decrease in the coercive field (E_c) and mechanical quality factor (Q_m) [1, 2]. Softening effects are attributed to an increase in domain wall mobility and there have been many hypotheses proposed to explain its origin. One explanation is based on a decrease in the internal stress caused by the formation of A-site vacancies [3]. Another theory is based on the fact that donor substitutional dopants can compensate for naturally-occurring acceptor defects and cation vacancies, leading to a net decrease in the concentration of oxygen vacancies which, when present as either isolated species or as part of a defect dipole, can effectively pin domain walls, therefore impacting domain wall mobility [4, 5].

Alternatively, acceptor doping or doping with lower valence cations (e.g. Fe^{3+} replacing Ti^{4+}/Zr^{4+}or K^{+} replacing Pb^{2+}) results in the formation of compensating oxygen vacancies. Defect associates and dipoles consisting of acceptor ions and compensating oxygen vacancies can be formed which then align along the polarization axes which leads to a stabilization of the domain configuration. Consequently, the material exhibits

"hardening" which is characterized by a reduction in piezoelectric activity, a decrease in ε_r and tan δ as well as an increase in Q_m and E_c [1, 6-8]. In addition, acceptor-doping also shows more pronounced aging effects due to the higher concentration of oxygen vacancies [9] which have been identified as a common mechanism in aging phenomena in both the grain boundary [10, 11] and defect dipole model [9, 12]. Hardened piezoelectric materials are very desirable in high-power applications such as transformers, ultrasonic motors and high intensity focused ultrasound (HIFU) since the high mechanical quality factor (low mechanical loss) and low dielectric loss help deliver high acoustic power with low heat generation [7].

However, due to the toxicity of lead oxide, which is the main component (~60-70 weight percent%) in PZT, replacement lead-free piezoelectric ceramics with comparable properties to that of PZT are needed. Among the available lead-free materials, a solid solution of $(1-x)(Bi_{0.5}Na_{0.5})TiO_3$-$xBaTiO_3$ ($(1-x)$BNT-xBT) has been developed as a promising candidate due to the excellent piezoelectric and electromechanical properties in compositions near the MPB. At room temperature, the MPB which features a rhombohedral BNT-like phase and a tetragonal BT-like phase was found to exist around x = 6-7 mol% BT. However, recent studies have reported that the crystal structure at the MPB is pseudocubic [13-15] rather than what was previously reported as a coexistence of rhombohedral and tetragonal phases [16]. A schematic representation of the phase diagram for this system as reported by Ma *et al.* is shown in Fig. 5.1.

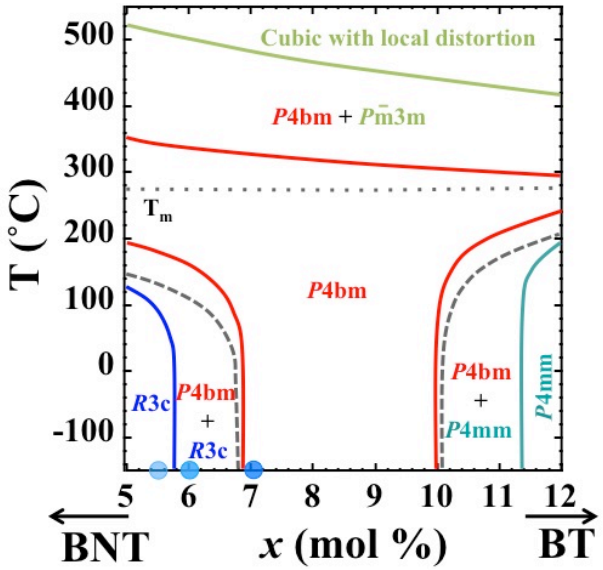

Fig. 5.1 (1-*x*)BNT-*x*BT phase diagram showing a morphotropic phase boundary between *R3c* and *P4bm* phase at x = 0.055, 0.06 and 0.07 (i.e. morphotropic phase boundary compositions) (figure adapted from Ma *et. al.* [17])

The depolarization temperature (T_d) and the temperature at which the dielectric constant is maximum (T_m) for the MPB compositions are found to be ~90-105°C and ~255-288°C [18], respectively. Due to various applications of acceptor-doped PZT, many studies have also been conducted to investigate the effect of acceptor-doping in lead-free (1-*x*)BNT-*x*BT based solid solutions. Unlike PZT or $BaTiO_3$, acceptor-doped BNT-based solid solutions exhibit only a slight or moderate hardening. For example, Aksel *et al.* [19] studied the effect of Fe_2O_3 doping on the B-site in BNT and noted a slight increase in E_c. This was attributed to the pseudocubic structure of BNT, which made almost no difference in the energy required for reorientation of defect dipole along all six oxygen octahedral sites. Jo *et al*. [20] also studied the effect of acceptor Fe-doped 92BNT-6BT-2KNN. However, due to the ergodic-relaxor nature of this composition,

which is characterized by a constricted *P-E* hysteresis loop, hardening characteristics like an increase in E_c or internal bias are difficult to resolve. In a study on Mn acceptor-doped 92BNT-8BT [21], an increase in Q_m was also observed. However, owing to a change in microstructure and density, it could not be concluded that the observed phenomena was the result of microscopic hardening.

In this study, the influence of A-site non-stoichiometry in (1-*x*)BNT-*x*BT compositions will be examined where x = 0.055, 0.06 and 0.07 (i.e. compositions near morphotropic phase boundary). The stoichiometric ratio of Bi/Na will be systematically varied so as to modify the total cation charge which in turn will result in effective donor or acceptor doping. The importance of this study is based on the fact that while prior work on chemical doping in (1-*x*)BNT-*x*BT has been carried out, the influence of the underlying cation stoichiometry on the hardening/softening characteristics has not been examined. This is important because both Na and Bi exhibit significant volatility during processing [22-24]. Therefore, it is important to examine the role of the cation stoichiometry on the underlying defect equilibria and electrical properties so that both doped and undoped compositions can be understood.

5.3 Experimental Procedure

Lead free piezoelectric ceramics based on 1-x($Bi_{0.5}Na_{0.5}$)TiO_3-$x$$BaTiO_3$ where x = 5.5, 6 and 7 mol% were prepared by a conventional solid state mixed oxide route. For each (1-*x*)BNT-*x*BT composition with x = 5.5, 6 and 7 mol%, A-site donor compositions

were synthesized by incorporating 2 mol% excess Bi_2O_3 and acceptor compositions were synthesized by incorporating 1 mol% excess Na_2O according to the chemical formula 1-x($Bi_{0.51}Na_{0.5}$)TiO_3-$x$$BaTiO_3$ (abbreviated as xBT(Bi)) and 1-x($Bi_{0.50}Na_{0.505}$)TiO_3-x$BaTiO_3$ (abbreviated as xBT(Na), respectively. Reagent grade powders of Bi_2O_3 (99.9%, Alfa Aesar), Na_2CO_3 (99.5%, Alfa Aesar), TiO_2 (99.9%, Sigma Aldrich) and $BaCO_3$ (99.9%, Alfa Aesar) were batched according to the chemical formula and then vibratory-milled using ethanol and yttrium-stabilized zirconia as a media for 6 h. Prior to batching, Na_2CO_3 powder was dried at 150°C for 10 h due to concerns regarding its hygroscopic nature. The obtained powders were then calcined at 800°C for 2 h followed by a re-milling and drying step in order to achieve sub-micron sized powder. The calcined powders were mixed with 3 wt% polyvinyl butyral (PVB) before uniaxially cold-pressing at 150 MPa to form a 12.7 mm diameter disc pellet. The pellets were sintered in a closed crucible at temperature between 1150 to 1180°C for 2 h with a polymer burned out step at 400°C for 3 h. A covered crucible with a sacrificial powder of the same composition was used during sintering to minimize the loss of the volatile Bi and Na components.

Phase purity and crystal structure determination was carried out on crushed sintered pellets using X-ray diffraction (XRD) with CuKα radiation (Bruker AXS D8) using a standard Bragg-Brentano geometry. In order to confirm the stoichiometry of the sintered ceramics, a high performance inductively coupled plasma-optical emission spectroscopy (ICP-OES) analysis with a relative standard deviation of 1% was performed on selected samples by Evans Analytical Group. Prior to electrical measurements,

samples were ground and polished to ~ 0.7 mm thick and then silver paste (Heraeus C1000) was applied on both sides and fired at 700°C for 0.5 h.

Dielectric measurements were carried out over a wide frequency and temperature range using an Agilent 4284A LCR meter equipped with a high temperature cell (NorECS ProboStat). Standard *P-E* hysteresis measurements were carried out using a ferroelectric test system based on a Sawyer-Tower circuit (Precision Premier II, Radiant technology) utilizing Vision software. To separate non-ferroelectric from ferroelectric polarization, PUND (positive-up-negative-down) tests and remanent *P-E* hysteresis measurements were performed on all samples. The determination of the mechanical quality factor (Q_m) was carried out by resonance/antiresonance method according to the IRE Standard [25] using an impedance gain/phase analyzer (Solartron SI1260A). The low field piezoelectric coefficient (d_{33}) was measured using a YE2730A d_{33} meter. All samples were poled by applying a dc electrical field of 60 kV/cm for 0.5 h at room temperature prior to the Q_m and d_{33} measurements.

5.4 Results and discussion

Figure 5.2 (a) shows the room temperature XRD patterns of donor (Bi), stoichiometric and acceptor (Na) doped (1-x)BNT-xBT ceramics, with x = 5.5, 6 and 7 mol% BT. A magnified 2θ region of (111), (200) and (211) peaks for each compositions is shown in Fig. 5.2 (b), (c) and (d), respectively. It should be noted that crushed pellets were used for the XRD in this study in order to get an accurate determination of the true

crystal structure. Our results and the findings of others have shown that the presence of ferroelastic 90° domains are seen in XRD data on the surface of ceramics after grinding [26].

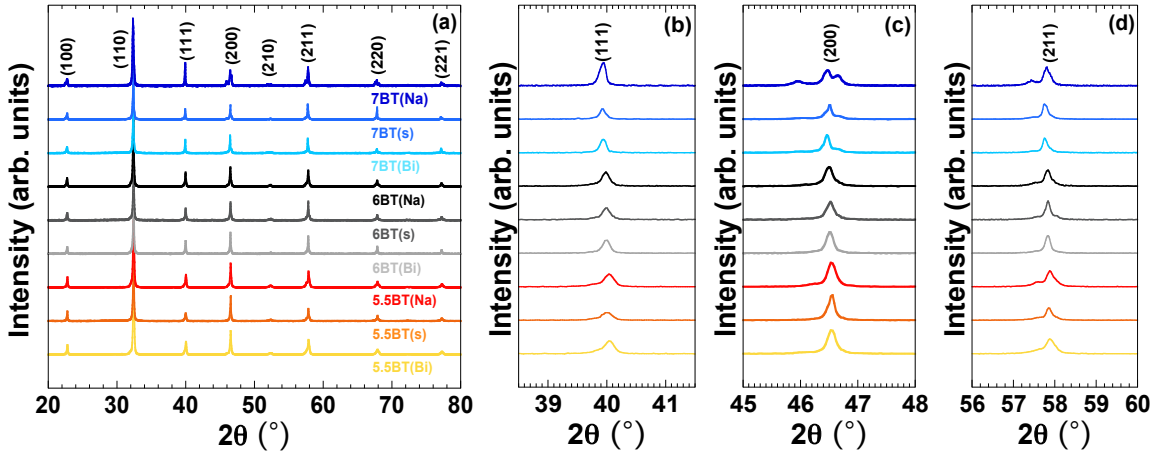

Fig. 5.2 (a) XRD patterns of donor (Bi) stoichiometric and acceptor (Na) doped (1-*x*)BNT-*x*BT where *x* = 5.5, 6 and 7 mol%. An enlarged 2θ region for (111), (200) and (211) reflections are shown in (b), (c) and (d), respectively

Within the resolution limit of the laboratory XRD, it is clearly seen that all ceramics possess a single-phase perovskite structure with no secondary phases. First, considering the stoichiometric compositions (identified as (s)), it can be seen that the 5.5BT(s) exhibited a pseudocubic structure with a slight rhombohedral distortion as seen from peak broadening and observable splitting in the (111) and (211) characteristic rhombohedral peaks along with the absence of any splitting or distortions in the (200) peak. With increasing *x* (i.e. 6BT(s) and 7BT(s)), the broadening decreased and the small shoulder in the (111) and (211) peaks gradually merged into a singlet peak while the

(200) peak evolved into a split peak as is clearly seen in the XRD data for 7BT(s). This suggests an evolution of the crystal structure from pseudocubic symmetry with a slight rhombohedral distortion to pseudocubic symmetry with a slight tetragonal distortion. This observation is in good agreement with the phase diagrams of the MPB region of unpoled (1-*x*)BNT-*x*BT proposed by Ma *et al.* [27-29]. Also, previous studies by both laboratory and synchrotron x-ray revealed the MPB crystal structure to be nearly cubic [13] or pseudocubic [14, 30]. For all donor-doped (i.e. Bi-excess) compositions (e.g. 5.5BT (Bi), 6BT (Bi) and 7BT (Bi)), the characteristics of the (111), (211) and (200) reflections remain principally the same as for the stoichiometric compositions, suggesting that donor-doping has little to no effect on the crystal structure. In contrast, an increase in the broadening and splitting of the (111) and (211) peaks was observed in all acceptor-doped (i.e. Na-excess) compositions (e.g. 5.5BT (Na), 6BT (Na) and 7BT (Na)), suggesting an increase in the rhombohedral distortions in the acceptor-doped compositions. Similar results were observed in the study by Spreitzer *et. al*. [31] where the original rhombohedral structure in pure BNT was suppressed and transformed into a cubic-like structure when sample was Na deficient.

To assess the quality of sintered samples and to confirm that the intended donor (2 mol% excess Bi) and acceptor (1 mol% excess Na) doped compositions were obtained, an elemental composition analysis ICP-OES was performed on selected samples [specifically (6BT (Bi) and 6BT (Na)]. The concentration of each element in mole percent (mol%) is shown in Table 5.1.

Table 5.1. A comparison of the concentration of each element between theoretical value of stoichiometric 6BT and determined value from ICP-OES for 6BT (Bi) and 6BT (Na)

Compositions	Concentration (mol%)			
	Bi	**Na**	**Ba**	**Ti**
Theoretical 6BT(s)	23.50	23.50	3.00	50.00
6BT(Bi)	24.01	22.46	3.00	50.52
Accuracy	0.32	0.44	0.082	0.76
6BT(Na)	23.89	22.44	2.93	50.75
Accuracy	0.54	1.65	0.33	1.47

While the data is not entirely clear some basic conclusions can be drawn. Within the equipment resolution and standard deviation, it is clearly seen from Table 5.1 that the measured concentration of Ba and Ti in both 6BT (Bi) and 6BT (Na) is close to the theoretical value, suggesting that there was no loss of these two non-volatile elements during processing. For the Bi-excess composition 6BT (Bi), the measured Bi concentration (24.01 mol%), taking into account the accuracy, is greater than that of the theoretical value (23.50 mol%), confirming that excess Bi was obtained. For the Na-excess composition 6BT(Na), the measured Bi concentration agrees well with theoretical value, while due to the large standard deviation in the measurement it is not possible to draw any conclusions about the Na concentration (measured at 22.44 mol%). Similar to other materials systems that are sensitive to small differences in starting compositions [32, 33], determining the composition in this study is quite challenging. Nevertheless, for the 6BT (Bi) composition, it can be unambiguously concluded that the sintered sample

exhibits enrichment in Bi even after considering the standard deviations in all possible extreme cases. For the 6BT(Na) composition, due to a high standard deviation of Na as mentioned earlier, it is not possible to derive any unambiguous conclusions. However, the rhombohedral distortions observed in excess Na compositions [i.e. *x*BT (Na), *x* = 5.5, 6 and 7] in the XRD data supports the conclusion that an excess of Na was obtained in these sintered ceramics. These are consistent with the findings of Spreitzer *et al*. [31] and Sung *et al.* [23] that observed an increase in rhombohedral distortions in BNT compositions with excess Na. The electrical properties (as will be shown in next section) will support these ICP results.

Figure 5.3 illustrates the temperature dependence of the dielectric constant and dielectric loss (tan δ) for *x*BT (Bi), *x*BT (s), and *x*BT(Na) where *x* = 5.5, 6 and 7 mol%. The depolarization temperature (T_d) and the temperature at which the dielectric constant is maximum (T_m) obtained from donor doped compositions (e.g. 5.5BT (Bi), 6BT (Bi) and 7BT (Bi)) are in a good agreement with previous studies [27, 28, 34, 35]. However, due to the high dielectric loss in the stoichiometric and acceptor-doped compositions it was not possible to accurately determine T_d. For all stoichiometric compositions, relatively high dielectric losses as well as an anomalous high dielectric constant at low frequencies (i.e. 100 Hz and 1 kHz) was observed. This high dielectric loss and anomalous high dielectric constant is indicative of the onset of conduction. It is likely that this can be ascribed to the loss of volatile Bi and Na during sintering which results in the formation of the vacancy defects (V_{Bi}''' , V_{Na}') along with compensating positively

charged defects (e.g. oxygen vacancies ($V_O^{\cdot\cdot}$), holes ($h^{\cdot}$)) [36]. Similar results were also reported in other stoichiometric BNT [22, 33] and other BNT-based systems [37].

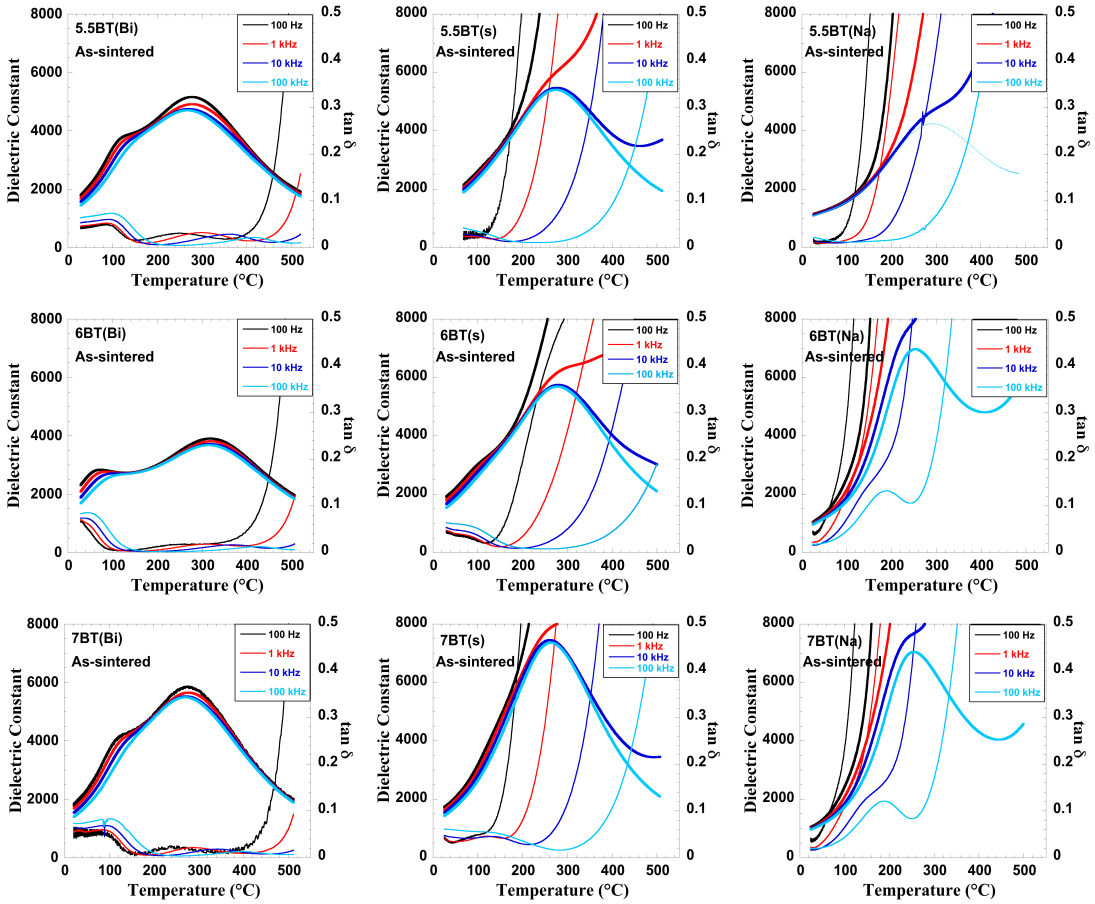

Fig. 5.3 Temperature dependence of dielectric constant and dielectric loss (tan δ) for donor (Bi) stoichiometric (s) and acceptor (Na) doped (1-x)BNT-xBT where x = 5.5, 6 and 7 mol%

Compared to stoichiometric compositions, donor-doped compositions show an excellent improvement in dielectric properties, which can be seen from not only the persistence of low dielectric loss (~2% at 10 kHz) up to high temperatures (500 °C) but also the disappearance of the anomalous high dielectric constant at low frequencies. This

can be attributed to two reasons. First, excess Bi compensates for Bi loss during sintering, leading to a decrease in both V_{Bi}''' defects and the compensating positively charged defects ($V_O^{\cdot\cdot}$ and $h^{\cdot}$) [38]. Second, due to a similar ionic radii between Bi ($r_{Bi^{3+}}$ = 1.38 Å) and Na ($r_{Na^{+}}$ = 1.39 Å) [39], it is most likely that some excess Bi substitutes for Na and results in positively charged $Bi_{Na}^{\cdot\cdot}$ defects which must be compensated either by an increase in negatively charged point defects (e.g. V_{Bi}''' , V_{Na}', e') or by a decrease in positively charged defects ($i.e. V_O^{\cdot\cdot}, h^{\cdot}$). The expected defect equilibrium is represented in equation 5.1:

$$e' + 3[V_{Bi}'''] + [V_{Na}'] + 4[V_{Ti}''''] + 2[Na_{Bi}''] = 2[V_O^{\cdot\cdot}] + h^{\cdot} + 2[Bi_{Na}^{\cdot\cdot}] \qquad (5.1)$$

However, due to the observed reduction in dielectric loss and presumed increase in resistivity, it is most likely that ionic compensation and a reduction in hole concentration is the dominant mechanism.

In opposite to donor-doped compositions, it is clearly seen that dielectric properties are significantly degraded in all acceptor-doped compositions. Again, due to a similar ionic radii between Bi and Na, it is likely that excess Na will replace Bi and result in Na_{Bi}'' defects, which subsequently leads to an increase in compensating positively charged defects ($V_O^{\cdot\cdot}$ and $h^{\cdot}$). An improvement of dielectric properties with donor doping through Bi-excess and a deterioration of the properties with acceptor doping through Na-excess confirms the ICP results that donor- and acceptor-doped compositions were obtained through Bi/Na non-stoichiometry.

Figure 5.4 shows a standard *P-E* hysteresis loops of donor (Bi) stoichiometric and acceptor (Na) doped (1-*x*)BNT-*x*BT, with *x* = 5.5, 6 and 7 mol% at room temperature. Typical square ferroelectric hysteresis loops are observed in all compositions as shown in Fig. 5.4 (a) (b) and (c). Interestingly, compared to the stoichiometric compositions, an increase in the coercive field (E_c) is observed in all A-site acceptor-doped compositions (e.g. *x*BT (Na), *x* =5.5, 6 and 7). This is one of the hardening characteristics that is typically seen in acceptor-doped PZT due to domain wall pinning [1, 8].

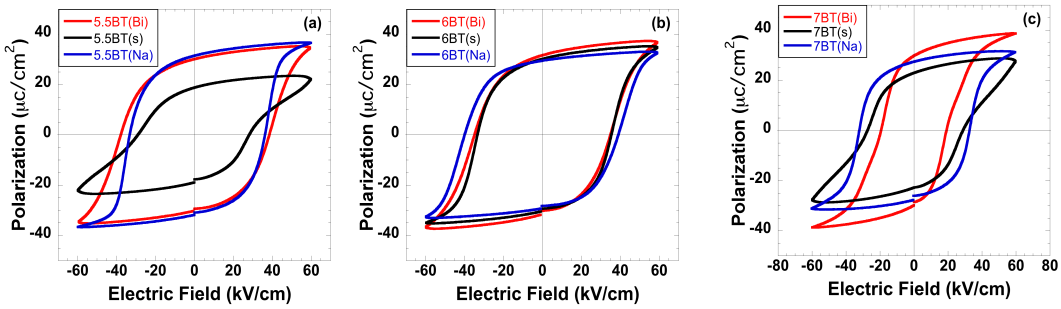

Fig. 5.4. Standard *P-E* hysteresis loops of donor (Bi) stoichiometric (s) and acceptor (Na) doped (1-*x*)BNT-*x*BT where *x* = 5.5, 6 and 7 mol% measured at room temperature with a frequency of 1 Hz

However, standard *P-E* hysteresis measurements include both ferroelectric (i.e. remanent polarization) and non-ferroelectric contributions (e.g. linear capacitance, resistance, diode effects, leakage currents, etc. which can be described as "a non-remanent polarization"). Given the relatively high losses seen in the dielectric measurements, remanent *P-E* hysteresis measurements and PUND tests were performed in order to determine the true ferroelectric polarization, which will in turn confirm that the observed phenomena was due to hardening rather than a misleading result from

conduction losses or leakage currents. The PUND test allows a separation of the ferroelectric from the non-ferroelectric contributions to the polarization by exploiting the fact that ferroelectric polarization remains unchanged after the applied electric field is removed. Therefore, when two consecutive electric pulses of the same polarity are applied, both the ferroelectric and non-ferroelectric polarization will respond to the first pulse (i.e. total or switched polarization or, P^*) while only non-ferroelectric contributions (i.e. non-switched polarization, $P^\wedge$) will respond to the second pulse [40]. Consequently, a subtraction of the non-switched polarization ($P^\wedge$) from the switched polarization (P^*) gives rise to the switchable (or remanent) polarization ($\Delta P = P^* - P^\wedge$). The results of the PUND measurement is shown in Table 5.2. Compared to the stoichiometric compositions, it can be seen that the switchable polarization (ΔP) of all acceptor-doped compositions is considerably less than that of the stoichiometric compositions.

Table 5.2 Room temperature switched polarization (P*), non-switched polarization ($P^{\wedge}$), and switchable polarization (ΔP) values measured from PUND tests on donor (Bi), stoichiometric (s), and acceptor (Na) doped (1-x)BNT-xBT ceramics (x = 5.5, 6 and 7%)

Compositions	P^* (μC/cm^2)	$P^{\wedge}$ (μC/cm^2)	ΔP (μC/cm^2)
5.5BT (Bi)	71.8	7.5	64.3
5.5BT (s)	84.7	6.8	77.9
5.5BT (Na)	79.1	10.5	68.6
6BT (Bi)	74.7	8.2	66.4
6BT (s)	67.8	8.2	59.6
6BT (Na)	62.2	6.8	55.4
7BT (Bi)	70.3	10.3	60.0
7BT (s)	73.4	7.4	65.9
7BT (Na)	50.5	10.3	40.2

For the remanent *P-E* hysteresis measurement, two consecutive half-triangular waves of the same polarity are used. Similar to the PUND test, subtraction of the non-switched polarization (non-ferroelectric contribution) from the switched polarization (total contribution) will give rise to the remanent *P-E* hysteresis loop as shown in Fig. 5.5. For all compositions, it can be seen that the remanent *P-E* hysteresis loop exhibits a reduction in P_r and becomes more square-like due to the elimination of the portion caused by conduction losses and other factors [1].

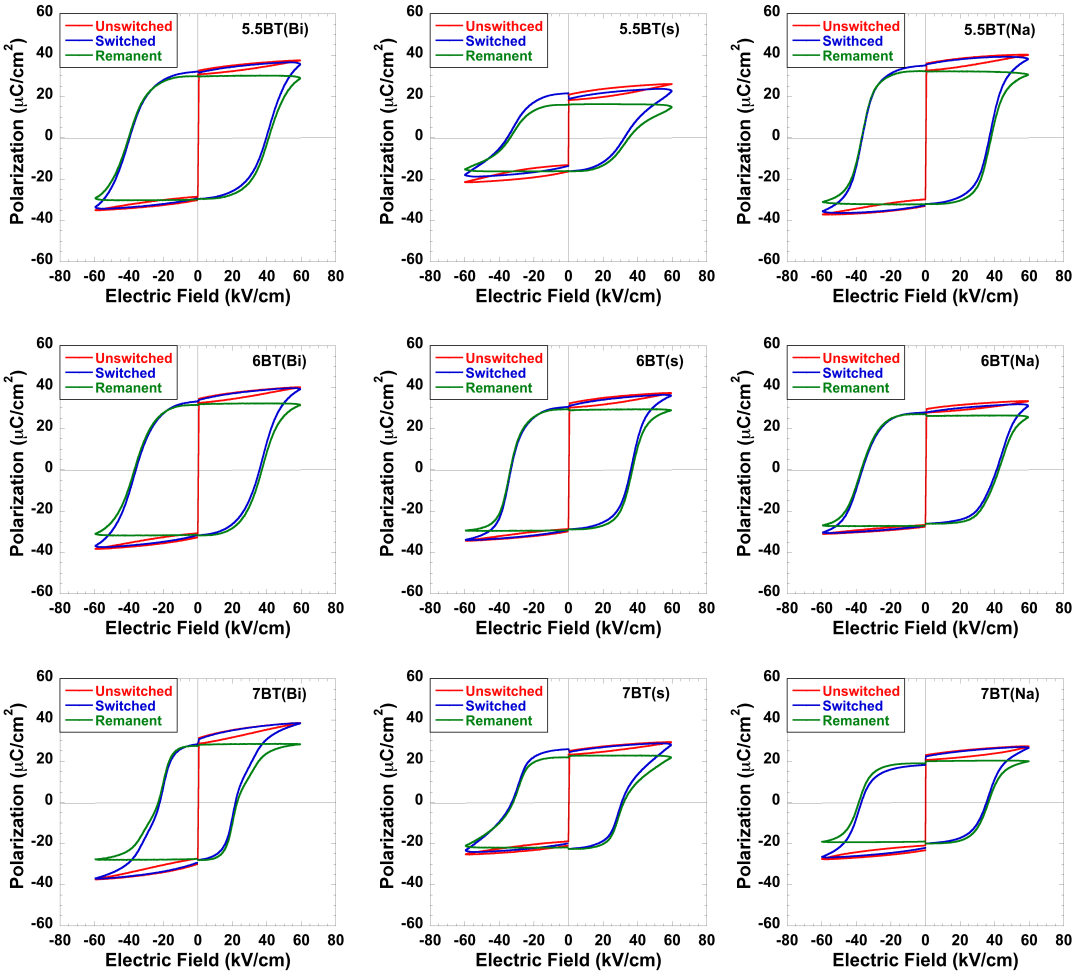

Fig. 5.5 Unswitched, switched and remanent *P-E* hysteresis data obtained from remanent hysteresis measurements from donor (Bi), stoichiometric and acceptor (Na) doped (1-*x*)BNT-*x*BT (*x* = 5.5, 6 and 7 mol% BT)

Figure 5.6 shows the remanent *P-E* hysteresis loops for donor-, stoichiometric and acceptor-doped (1-*x*)BNT-*x*BT compositions for each *x* = 5.5, 6 and 7 mol% BT on the same plot. It is clearly seen that an increase in E_c was observed in all acceptor-doped compositions. Since the remanent *P-E* hysteresis data is free from non-ferroelectric contributions, this result confirms that the observed increase in E_c is due to true hardening rather than an artifact from conduction losses.

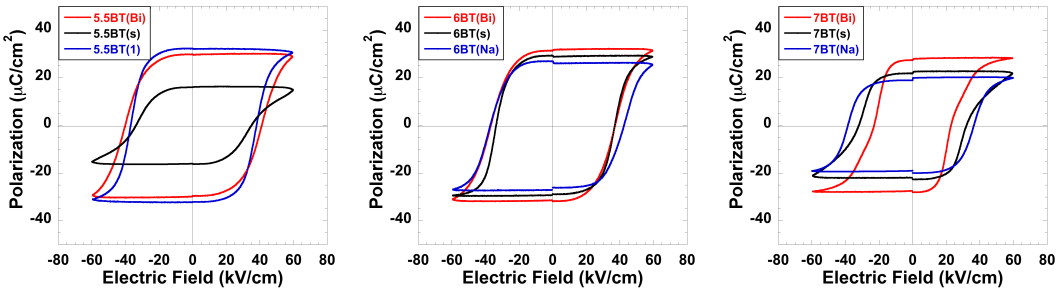

Fig. 5.6 Remanent *P*-*E* hysteresis of donor (Bi), stoichiometric and acceptor (Na) doped (1-*x*)BNT-*x*BT (*x* = 5.5, 6 and 7 mol% BT)

The value of P_r and E_c extracted from standard and remanent *P*-*E* hysteresis loop are shown in Table 5.3. In addition, after taking out the non-ferroelectric contributions, apart from the observed hardening characteristics in acceptor doped compositions, a "softening" characteristic (which include a decrease in E_c and an increase in P_r) was revealed in donor-doped 6BT and 7BT compositions.

Table 5.3. Values for P_r and E_c extracted from standard and remanent *P-E* hysteresis data for donor (Bi), stoichiometric, and acceptor (Na) doped (1-*x*)BNT-*x*BT (*x* = 5.5, 6 and 7 mol% BT)

Compositions	Normal *P-E* hysteresis		Remanent *P-E* hysteresis	
	E_c (kV/cm)	P_r (μC/cm^2)	E_c (kV/cm)	P_r (μC/cm^2)
5.5BT (Bi)	38.6	30.1	41.2	29.9
5.5BT (s)	28.3	18.8	35.1	16.0
5.5BT (Na)	36.3	31.5	38.1	32.3
6BT (Bi)	34.9	31.6	37.2	31.4
6BT (s)	35.4	30.2	36.9	29.3
6BT (Na)	39.2	29.5	42.6	27.0
7BT (Bi)	19.1	29.8	22.9	27.4
7BT (s)	28.8	22.9	32.0	21.9
7BT (Na)	32.7	27.4	36.5	19.0

The piezoelectric coefficient (d_{33}) and mechanical quality factor (Q_m) were also investigated and their corresponding values are shown in Table 5.4. The d_{33} values on stoichiometric samples poled at room temperature at a field of 60 kV/cm are in excellent agreement with previous studies where d_{33} values were reported to be between 122 and 176 pC/N [16, 18, 34, 41, 42]. Compared to the stoichiometric compositions, a significant decrease in d_{33} values was observed in all acceptor-doped compositions, e.g. a decrease from 148 (7BT (s)) to 44 pC/N (7BT (Na)). The d_{33} coefficients were measured again after 7 days and the same trend still persisted.

Table 5.4 Dielectric (ε_r, tan δ) and piezoelectric (d_{33} and Q_m) properties, of donor (Bi), stoichiometric (s) and acceptor (Na) doped (1-*x*)BNT-*x*BT, (*x* = 5.5, 6 and 7 mol% BT)

Compositions	ε_r @1kHz	tanδ @1kHz	d_{33} (pC/N)		Q_m
			1 h after poling	7 days after poling	
5.5BT (Bi)	1810	0.043	132	126	106
5.5BT (s)	1780	0.042	128	120	113
5.5BT (Na)	1150	0.01	81	78	246
6BT (Bi)	2110	0.069	142	151	69
6BT (s)	1790	0.047	125	127	150
6BT (Na)	1050	0.023	82	110	323
7BT (Bi)	1810	0.058	197	180	67
7BT (s)	1700	0.038	148	138	156
7BT (Na)	1040	0.021	44	48	196

For the "hardened" piezoelectric ceramics, internal friction is reduced due to the stabilization of the domain configuration. Therefore, the mechanical quality factor (Q_m), which is defined as a reciprocal of internal friction, is typically increased [43]. Consistent with prior results, it is clearly seen that the Q_m values of all acceptor-doped compositions were higher than that of the stoichiometric compositions. In addition, since a major contribution to the dielectric response measured at in kHz regime is derived from domain wall motion, the observed decrease in ε_r and tan δ could again be an indication of hardening [44]. A comparison of the dielectric properties including ε_r and tan δ, measured at 1 kHz are presented in Table 5.4. Similar to the results obtained in this study, a decrease in d_{33}, ε_r and tan δ as well as an increase of Q_m as a result of domain

wall stabilization has also been observed in acceptor-doped BT, PZT [45] and the lead-free ferroelectric $K_{0.5}Na_{0.5}NbO_3$ [7, 46]. Moreover, it should be noted that some evidence of "softening" characteristics (e.g. an increase in ε_r, tan δ, d_{33} and a decrease in Q_m) was also observed in the donor-doped compositions as seen in Table 5.4.

The sum of the experimental results in this study have clearly shown that the dielectric, ferroelectric and piezoelectric properties in all A-site acceptor-doped compositions in the system (1-x)BNT-xBT (x = 5.5, 6 and 7 mol% BT) correspond to "hardening" characteristics linked to a microscopic origin (i.e. domain stabilization) similar to what has been typically observed in ferroelectric PZT and BT. For a further analysis, we compare "hardening" due to B-site acceptor-doping in the conventional ferroelectric BT and the relaxor BNT-based system. For $BaTiO_3$, which has tetragonal ferroelectric structure with long-range domain structure, acceptor-doping on the B-site results in the formation of defect dipoles between negatively charged acceptor ions (e.g. Fe'_{Ti}) and compensating oxygen vacancies ($V_O^{\cdot\cdot}$). These defect dipoles ($Fe'_{Ti} - V_O^{\cdot\cdot}$) will eventually align along the spontaneous polarization, leading to stabilization of the domain wall which results in hardening characteristics [47].

As opposed to PZT and BT, a slight or moderate hardening and aging was observed in B-site acceptor-doped BNT-based systems [19, 48]. This discrepancy mainly arises from a different domain structure between conventional ferroelectric (with long-range domain structure) and BNT-based systems (with polar nanoregions (PNR)) as seen in a recent study by Sapper *et al.* [48]. In this study, the observation of aging effects due to 1 mol% Fe acceptor-doped (1-x)BNT-xBT (x = 1, 4, 6 and 15 mol% BT) was

investigated. That study showed that the aging effect was not observed in BNT-1BT, BNT-4BT and BNT-6BT, which are compositions that have dominant relaxor-like characteristics (i.e. PNR). In contrast, a decrease of P_r and E_c, which is an indication of aging from domain wall clamping, was observed in BNT-15BT because a ferroelectric long-range domain structure existed due to the increased mole fraction of BT.

Based on these findings, hardening due to A-site acceptor-doping in this study can be attributed to the simultaneous occurrance of a long-range domain structure and a clamping of the domain structures by defect dipoles. As explained earlier, a deterioration in dielectric properties of all A-site acceptor-doped (Na) compositions is most likely due to an increase in the concentration of positively charged defects ($V_O^{\cdot\cdot}, h^{\cdot}$) which compensate for the negatively charged defects Na_{Bi}''. Subsequently, defect dipoles between A-site acceptor ions and oxygen vacancies ($Na_{Bi}'' - V_O^{\cdot\cdot}$) could be formed. This is analogous to defect dipoles formed between B-site acceptor ions and oxygen vacancies ($Fe_{Ti}' - V_O^{\cdot\cdot}$) in recent studies by Chandrasekaran *et al.* [4] which showed evidence of defect dipoles between A-site lead vacancies and oxygen vacancies ($V_{Pb}'' - V_O^{\cdot\cdot}$) in tetragonal $PbTiO_3$ that preferentially align along unit cell spontaneous polarization directions. Therefore, it is possible that ($Na_{Bi}'' - V_O^{\cdot\cdot}$) defect dipoles align along the spontaneous polarization directions in the host structure of (1-*x*)BNT-*x*BT which stabilizes the domain structure.

In addition, it is also important to note that rhombohedral distortion is enhanced in all acceptor-doped (Na) compositions, implying that more long-range domain structures are developed. Therefore, it is most likely that defect dipoles ($Na_{Bi}'' - V_O^{\cdot\cdot}$) could stabilize

both PNR structures and long-range domain structures which directly results in the observed hardening characteristics. It was also observed that a greater degree of hardening (i.e. a greater change in E_c and P_r between the stoichiometric and acceptor-doped compositions) was obtained with an increase in BT content. This is likely due to an increase in the long-range ferroelectric order. This further supports the study by Sapper *et al.* [48] where the aging effect was found to be more pronounced in BNT-15BT than that of BNT-1BT.

5.5 Conclusions

Single-phase perovskites in the (1-x)BNT-xBT system where x = 0.055, 0.06 and 0.07 (i.e., near the morphotropic phase boundary) were prepared with modified cation stoichiometry to induce acceptor (excess Na) and donor (excess Bi) doping. Donor doping had no effects on the crystal structure while acceptor doping promoted rhombohedral distortions. A significant improvement in the dielectric properties was observed in all donor-doped and a deterioration in dielectric properties was observed in all acceptor-doped compositions. Compared to the stoichiometric composition, acceptor-doped compositions exhibited all of the expected "hardening" characteristics, including a decrease in d_{33}, ε_r and tan δ, as well as an increase in Q_m and E_c. The measured increase in E_c and decrease in P_r were confirmed by PUND tests and remanent P-E hysteresis measurements. The mechanism for the hardening in A-site doped BNT-based systems as compared B-site doping were explained based on an enhancement in the long-range domain structure and the defect chemistry.

5.6 References

1. Jaffe, B., *Piezoelectric ceramics*. Vol. 3. 1971: Academic press London and Newyork.

2. Berlincourt, D., O.E. Mattiat, and Y. Kikuchi, *Ultrasonic transducer materials*. 1971: Plenum Pub Corp.

3. Gerson, R., *Variation in ferroelectric characteristics of lead zirconate titanate ceramics due to minor chemical modifications*. Journal of Applied Physics, 1960. **31**(1): p. 188-194.

4. Chandrasekaran, A., et al., *Defect ordering and defect–domain-wall interactions in $PbTiO_3$: A first-principles study*. Physical Review B, 2013. **88**(21): p. 214116.

5. He, L. and D. Vanderbilt, *First-principles study of oxygen-vacancy pinning of domain walls in $PbTiO_3$*. Physical Review B, 2003. **68**(13): p. 134103.

6. Moulson, A.J. and J.M. Herbert, *Electroceramics: materials, properties, applications*. 2003: John Wiley & Sons.

7. Zhang, S., et al., *Characterization of hard piezoelectric lead-free ceramics*. Ultrasonics, Ferroelectrics and Frequency Control, IEEE Transactions on, 2009. **56**(8): p. 1523-1527.

8. Shrout, T.R. and S.J. Zhang, *Lead-free piezoelectric ceramics: Alternatives for PZT?* Journal of Electroceramics, 2007. **19**(1): p. 113-126.

9. Lambeck, P. and G. Jonker, *The nature of domain stabilization in ferroelectric perovskites*. Journal of Physics and Chemistry of Solids, 1986. **47**(5): p. 453-461.

10. Lupascu, D.C., Y.A. Genenko, and N. Balke, *Aging in ferroelectrics*. Journal of the American Ceramic Society, 2006. **89**(1): p. 224-229.

11. Genenko, Y.A., et al., *Aging of poled ferroelectric ceramics due to relaxation of random depolarization fields by space-charge accumulation near grain boundaries*. Physical Review B, 2009. **80**(22): p. 224109.

12. Robels, U. and G. Arlt, *Domain wall clamping in ferroelectrics by orientation of defects*. Journal of applied physics, 1993. **73**(7): p. 3454-3460.

13. Ranjan, R. and A. Dviwedi, *Structure and dielectric properties of $(Na_{0.50}Bi_{0.50})_{1-x}Ba_xTiO_3$: $0 \le x \le 0.10$*. Solid state communications, 2005. **135**(6): p. 394-399.

14. Simons, H., et al., *Electric-field-induced strain mechanisms in lead-free 94%($Bi_{1/2}Na_{1/2}$)TiO_3–6%$BaTiO_3$*. Applied Physics Letters, 2011. **98**(8): p. 082901.

15. Daniels, J.E., et al., *Electric-field-induced phase transformation at a lead-free morphotropic phase boundary: Case study in a 93%($Bi_{0.5}Na_{0.5}$)TiO_3–7%$BaTiO_3$ piezoelectric ceramic*. Applied Physics Letters, 2009. **95**(3): p. -.

16. Takenaka, T., K.-I. Maruyama, and K. Sakata, *($Bi_{1/2}Na_{1/2}$)TiO_3–$BaTiO_3$ system for lead-free piezoelectric ceramics*. Japanese Journal of Applied Physics, 1991. **30**(9B): p. 2236-2239.

17. Ma, C. and X. Tan, *In situ Transmission Electron Microscopy Study on the Phase Transitionsin Lead-Free (1−x)($Bi_{1/2}Na_{1/2}$)TiO_3–x$BaTiO_3$ Ceramics*. Journal of the American Ceramic Society, 2011. **94**(11): p. 4040-4044.

18. Rödel, J., et al., *Perspective on the Development of Lead-free Piezoceramics*. Journal of the American Ceramic Society, 2009. **92**(6): p. 1153-1177.

19. Aksel, E., et al., *Defect structure and materials "hardening" in FeO-doped [BiNa]TiO ferroelectrics*. Applied Physics Letters, 2010. **97**: p. 012903.

20. Jo, W., et al., *Effect of Nb-donor and Fe-acceptor dopants in ($Bi_{1/2}Na_{1/2}$)TiO_3–$BaTiO_3$–($K_{0.5}Na_{0.5}$)NbO_3 lead-free piezoceramics*. Journal of Applied Physics, 2010. **108**(1): p. 014110-014110-6.

21. Zhu, M., et al., *Microstructure and Electrical Properties of MnO-Doped ($Na_{0.5}Bi_{0.5}$)$_{0.92}Ba_{0.08}TiO_3$ Lead-Free Piezoceramics*. Journal of the American Ceramic Society, 2007. **90**(1): p. 120-124.

22. Hiruma, Y., H. Nagata, and T. Takenaka, *Thermal depoling process and piezoelectric properties of bismuth sodium titanate ceramics*. Journal of Applied Physics, 2009. **105**(8): p. 084112-084112-8.

23. Sung, Y., et al., *Effects of Na nonstoichiometry in $Bi_{0.5}Na_{0.5+x}TiO_3$ ceramics*. Applied Physics Letters, 2010. **96**(2): p. 022901-022901-3.

24. Sung, Y., et al., *Effects of Bi nonstoichiometry in ($Bi_{0.5+x}$Na)TiO_3 ceramics*. Applied Physics Letters, 2011. **98**(1): p. 012902.

25. Jaffe, H., et al., *IRE standards on piezoelectric crystals: measurements of piezoelectric ceramics*. Proc. IRE, 1961. **49**: p. 1161-1169.

26. Hammer, M., et al., *Correlation between surface texture and chemical composition in undoped, hard, and soft piezoelectric PZT ceramics*. Journal of the American Ceramic Society, 1998. **81**(3): p. 721-724.

27. Ma, C., et al., *Domain structure-dielectric property relationship in lead-free (1-x)($Bi_{1/2}Na_{1/2}$)TiO_3-x$BaTiO_3$ ceramics*. Journal of Applied Physics, 2010. **108**(10): p. 104105-104105-8.

28. Ma, C. and X. Tan, *Phase diagram of unpoled lead-free–ceramics*. Solid State Communications, 2010. **150**(33): p. 1497-1500.

29. Ma, C., H. Guo, and X. Tan, *A New Phase Boundary in ($Bi_{1/2}Na_{1/2}$)TiO_3–$BaTiO_3$ Revealed via a Novel Method of Electron Diffraction Analysis*. Advanced Functional Materials, 2013. **23**(42): p. 5261-5266.

30. Daniels, J.E., et al., *Electric-field-induced phase transformation at a lead-free morphotropic phase boundary: Case study in a 93%($Bi_{0.5}Na_{0.5}$)TiO_3–7%*. Applied Physics Letters, 2009. **95**(3): p. 032904-032904-3.

31. Spreitzer, M., M. Valant, and D. Suvorov, *Sodium deficiency in $Na_{0.5}Bi_{0.5}TiO_3$*. Journal of Materials Chemistry, 2007. **17**(2): p. 185-192.

32. Kofstad, P., *Nonstoichiometry, Diffusion, and Electrical Conductivity in Binary Metal Oxides*. 1972: Interscience, Wiley.

33. Li, M., et al., *A family of oxide ion conductors based on the ferroelectric perovskite $Na_{0.5}Bi_{0.5}TiO_3$*. Nature materials, 2014. **13**(1): p. 31-35.

34. Xu, C., D. Lin, and K. Kwok, *Structure, electrical properties and depolarization temperature of ($Bi_{0.5}Na_{0.5}$)TiO_3-$BaTiO_3$ lead-free piezoelectric ceramics*. Solid state sciences, 2008. **10**(7): p. 934-940.

35. Rödel, J., et al., *Perspective on the Development of Lead-free Piezoceramics*. Journal of the American Ceramic Society, 2009. **92**(6): p. 1153-1177.

36. Smyth, D.M., *The defect chemistry of metal oxides*. The Defect Chemistry of Metal Oxides, by DM Smyth, pp. 304. Foreword by DM Smyth. Oxford University Press, Jun 2000. ISBN-10: 0195110145. ISBN-13: 9780195110142, 2000. **1**.

37. Zuo, R., et al., *Influence of A-site nonstoichiometry on sintering, microstructure and electrical properties of ($Bi_{0.5}Na_{0.5}$)TiO_3 ceramics*. Materials Chemistry and Physics, 2008. **110**(2): p. 311-315.

38. Eichel, R.-A., *Structural and dynamic properties of oxygen vacancies in perovskite oxides—analysis of defect chemistry by modern multi-frequency and pulsed EPR techniques*. Physical Chemistry Chemical Physics, 2011. **13**(2): p. 368-384.

39. Shannon, R.t., *Revised effective ionic radii and systematic studies of interatomic distances in halides and chalcogenides*. Acta Crystallographica Section A: Crystal Physics, Diffraction, Theoretical and General Crystallography, 1976. **32**(5): p. 751-767.

40. Technologies, R. *RT66A Analysis 2.1 User's Manual*.

41. Chen, M., et al., *Structure and electrical properties of $(Na_{0.5}Bi_{0.5})_{1-x}Ba_xTiO_3$ piezoelectric ceramics*. Journal of the European Ceramic Society, 2008. **28**(4): p. 843-849.

42. Chu, B.-J., et al., *Electrical properties of $Na_{1/2}Bi_{1/2}TiO_3$-$BaTiO_3$ ceramics*. Journal of the European Ceramic Society, 2002. **22**(13): p. 2115-2121.

43. Takahashi, S. and M. Takahashi, *Effects of impurities on the mechanical quality factor of lead zirconate titanate ceramics*. Japanese Journal of Applied Physics, 1972. **11**(1): p. 31.

44. Damjanovic, D., *Ferroelectric, dielectric and piezoelectric properties of ferroelectric thin films and ceramics*. Reports on Progress in Physics, 1998. **61**(9): p. 1267.

45. Pohanka, R.C. and P. Smith, *Recent advances in piezoelectric ceramics*. Electronic Ceramics, 1987: p. 45-146.

46. Lin, D., K. Kwok, and H. Chan, *Piezoelectric and ferroelectric properties of Cu-doped $K_{0.5}Na_{0.5}NbO_3$ lead-free ceramics*. Journal of Physics D: Applied Physics, 2008. **41**(4): p. 045401.

47. Zhang, L. and X. Ren, *Aging behavior in single-domain Mn-doped $BaTiO_3$ crystals: Implication for a unified microscopic explanation of ferroelectric aging*. Physical Review B, 2006. **73**(9): p. 094121.

48. Sapper, E., et al., *Aging in the relaxor and ferroelectric state of Fe-doped $(1-x)(Bi_{1/2}Na_{1/2})TiO_3$-$xBaTiO_3$ piezoelectric ceramics*. Journal of Applied Physics, 2014. **116**(10): p. 104102.

6 Effects of A-site Non-Stoichiometry on Oxide Ion Conduction in $0.94Bi_{0.5}Na_{0.5}TiO_3$-$0.06BaTiO_3$ Ceramics

Sasiporn Prasertpalichat, Whitney Schmidt and David P. Cann

Materials Science, School of Mechanical Industrial and Manufacturing Engineering

Oregon State University

Corvallis, OR 97331

In Preparation to Publish in

Journal Chemistry of Materials

6.1 Abstract

Lead free $0.94(Bi_{0.5}Na_{0.5})TiO_3$-$0.06BaTiO_3$ ceramics were prepared by conventional solid state mixed oxide route with the A-site stoichiometry modified to incorporate donor-doping (through Bi-excess) and acceptor-doping (through Na-excess). Both stoichiometric and non-stoichiometric ceramics exhibited a single perovskite phase with pseudo-cubic symmetry. Significant improvements in the dielectric properties were observed in Bi-excess compositions and a deterioration in properties was observed in Na-excess compositions. Impedance spectroscopy was utilized to analyze the effects of A-site non-stoichiometry on conduction mechanisms. Bi-excess compositions resulted in an electrically homogeneous microstructure with an increase in resistivity by ~3-4 orders of magnitude and an associated activation energy of 1.57 eV which was close to half of the optical band gap. In contrast, an electrically heterogeneous microstructure was observed in both the stoichiometric and Na-excess compositions. In addition, the Na-excess compositions exhibited low resistivities ($\rho \sim 10^3$ Ω-cm) with characteristic peaks in the impedance data indicating ionic conductivity similar to recent observations of oxide ion conduction in $(Bi_{0.5}Na_{0.5})TiO_3$. Long term annealing studies were also conducted at 800°C to identify changes in crystal structure and electrical properties. The results of this study demonstrate that the dielectric and electrical properties of $0.94(Bi_{0.5}Na_{0.5})TiO_3$-$0.06BaTiO_3$ ceramics are very sensitive to Bi/Na stoichiometry.

6.2 Introduction

The $Pb[Zr_xTi_{1-x}]O_3$ (PZT) oxides have been dominating piezoelectric material market for more than half a century due to the excellent piezoelectric properties at the morphotropic phase boundary (MPB) [1]. Not only has it been used in both thin film and ceramic embodiments, nanoscale structured PZT has also been investigated for use in ferroelectric memory applications [2]. However, environmental and health concerns regarding the toxicity of lead (Pb^{2+}) has led to a restriction on its use in many electronic and electrical devices as seen in legislation in the European union [3] and other countries [4-6]. Therefore, a search for lead-free piezoelectric materials with comparable properties to that of PZT is a topic of significant current interest [7]. The perovskite compound $Bi_{0.5}Na_{0.5}TiO_3$ (BNT) is one of the most promising candidates due to high remanent polarization (P_r of 38 $\mu C/cm^2$) and high maximum temperature (T_m of 320°C) [8]. However, high leakage currents [9] and a high coercive field (E_c = 73 kV/cm) make the poling process very difficult, thus preventing high piezoelectric properties from being achieved. To overcome these issues, a number of BNT-based solid solutions were explored e.g. BNT-$BaTiO_3$ (BNT-BT) [10-12], BNT-$Bi_{0.5}K_{0.5}TiO_3$ (BNT-BKT) [13], BNT-BT-$K_{0.5}Na_{0.5}TiO_3$ (BNT-BT-KNN) [14] and BNT-$NaNbO_3$ (BNT-NN) [15].

Among BNT-based materials, BNT-BT-based solid solutions have attracted a great deal of attention due to the existence of the MPB at a composition 0.94BNT-0.06BT that is characterized by ferroelectric rhombohedral and tetragonal phases. Similar to PZT, compositions near this MPB are accompanied by an enhancement in dielectric permittivity and piezoelectric coefficients [12]. Later studies further refined the

location of the MPB of (1-*x*)BNT-*x*BT to be over the compositional range of x = 0.06-0.08 [11, 12, 16, 17]. Reports about the crystal structure at the MPB reveal that it is quite complex. There exists a discrepancy between the local structure and the average long range structure. In addition, upon application of an electric field there is a shift in the MPB position as well as a change in the structure of the MPB [18]. For $x = 0.06$, within the resolution limits of laboratory-scale XRD instrumentation, independent studies from Ranjan *et al.* [19] and Zhang *et al.* [20] reported the room temperature structure to be pseudocubic. Later studies from high resolution neutron diffraction [21] confirmed the structure to be pseudocubic with slight tetragonal and rhombohedral distortions. However, the local structure determined by using TEM [22, 23] appeared to be a mixture of complex domain (*R3c*) and nanodomain (*P4bm*) structures. Similarly, the average structure of the $x = 0.07$ composition obtained from high resolution synchrotron XRD showed pseudocubic symmetry [24] whereas a TEM study revealed only nanodomain features corresponding to *P4bm* symmetry. In addition, recent *in situ* TEM results showed that the MPB (i.e. $x = 5.5$, 6 and 7%) was not stable under an applied electric field and the constituent (*R3c*) and (*P4bm*) phases can be created or destroyed. For example, for compositions at $x = 5.5$ and 6% BT, an initial MPB with co-existing *R3c* and *P4bm* phases completely transformed to pure *R3c* (i.e. the MPB was destroyed) through the sequence *P4bm* > *P4mm* > *R3c*.

The depolarization temperature (T_d) and the temperature at which the dielectric constant is maximum (T_m) for MPB compositions were reported to be in a range of ~90-105 °C and ~ 255-288 °C [25], respectively. Recent studies proposed that T_d at MPB (x = 0.06) does not involve any phase change from a ferroelectric to antiferroelectric state

but is instead the result of an evolution of a coexistence of *R3c* and *P4bm* polar nanoregions at increasing temperatures [26].

For the BNT end member compound, a small change in the stoichiometry of the A-site cation, which is most likely due to the volatility of Na and Bi cations during sintering, was found to significantly affect the conductivity, the dielectric properties as well as the piezoelectric properties. For example, Hiruma *et al.* [27] observed an improvement in dielectric properties with an enhancement in resistivity by one order of magnitude in BNT samples which have a Bi/Na ratio greater than 1 (e.g. Bi-excess or Na-deficient samples). Also, Sung *et al*. [28] showed an improvement in resistivity and d_{33} but a lower in T_d in samples prepared with excess bismuth (e.g. $Bi_{0.5+x}Na_{0.5}TiO_3$, x = 0.01, 0.02). Although these previous studies attempted to control the Bi/Na ratio, some reports fail to address the hygroscopic nature of the Na_2CO_3 starting reagent. A recent study by Li *et al.* focused on the effect of drying the Na_2CO_3 starting reagent and found that the transport properties are sensitive to the control of stoichiometry [29]. In addition, a recent study by Li *et al.* [30] explicitly showed that oxygen vacancies were responsible for the high leakage current in Bi-deficient BNT, and consequently revealed that BNT has great potential for oxide ion conductor applications.

In BNT, the effects of A-site non-stoichiometry on the electrical properties has been extensively investigated and the results were very helpful in explaining the resultant changes in dielectric, ferroelectric and piezoelectric properties in BNT. However, no study regarding the effect of A-site non-stoichiometry in (*1*-*x*)BNT-*x*BT compositions near the morphotropic phase boundary have been reported in the literature. Therefore, in

this study, the effects of A-site acceptor-doped (through Na excess) and A-site donor-doped (through Bi excess) modifications on the composition 94BNT-6BT (i.e. near the MPB) on electrical properties will be investigated by using impedance spectroscopy. The annealing effects on each composition were also studied. In addition, our previous study demonstrated hardening similar to the hardening characteristics that are typically observed in hardened PZT in acceptor-doped (Na excess) *(1-x)*BNT-*x*BT in the compositions x = 0.055, 0.06 and 0.07 (i.e. MPB compositions). Therefore, this study will help clarify the effects of A-site non-stoichiometry on the electrical properties as well as giving more insight into the observed hardening in our previous study.

6.3 Experimental Procedure

Ceramics of the composition $0.94(Bi_{0.5}Na_{0.5})TiO_3$-$0.06BaTiO_3$ [denoted as 6BT (s) hereafter] were prepared by conventional solid state mixed oxide route. A-site donor- and acceptor-doping compositions were synthesized according to the chemical formula $0.94(Bi_{0.51}Na_{0.50})TiO_3$-$0.06BaTiO_3$ [denoted as 6BT (Bi)] and $0.94(Bi_{0.50}Na_{0.505})TiO_3$-$0.06BaTiO_3$ [denoted as 6BT (Na)], respectively. Prior to batching, Na_2CO_3 powders were dried at 150°C for 10 h due to concerns regarding its hygroscopic nature. The reagent grade powder of Bi_2O_3 (99.9%, Alfa Aesar), Na_2CO_3 (99.5%, Alfa Aesar), TiO_2 (99.9%, Sigma Aldrich) and $BaCO_3$ (99.9%, Alfa Aesar) were weighed according to the chemical formula and then vibratory-milled in ethanol using yttrium-stabilized zirconia media for 6 h. Powders were calcined at 800°C for 2 h before re-milling and drying again in order to achieve sub-micron sized powder. Calcined powders were mixed with 3

wt% polyvinyl butyral (PVB) before uniaxially cold-pressing at 150 MPa to form a 12.7 mm diameter disc. A covered crucible with a sacrificial powder of the same composition was used in order to minimize the loss of volatile Bi and Na components during sintering. The sintering temperatures for donor-, stoichiometric, and acceptor-doped 94BNT-6BT were 1,170, 1,160 and 1,150°C, respectively. For the annealing study, sintered pellets were buried in the powders of the same compositions and annealed at 800°C in air for 7 days.

Phase purity and crystal structure determination was carried out on crushed sintered pellets using X-ray diffraction (XRD, Bruker AXS D8) with CuKα radiation in a standard Bragg-Brentano geometry. Prior to electrical measurements, samples were ground and polished to ~ 0.7 mm thick and then silver electrodes (Heraeus C1000) were applied to both sides and fired at 700°C for 0.5 h. Dielectric measurements were conducted over a wide temperature range (25-600^{o}C) using a high temperature measurement cell (NorECS ProboStat) equipped with an LCR meter (Agilent 4284A). Impedance spectroscopy (IS) measurements were conducted at different temperatures over the frequency range of 0.1 Hz to 1 MHz by using an impedance gain/phase analyzer (Solatron 1260A), which was equipped with Solatron 1296A dielectric interface in order to improve data accuracy at low frequencies. Before impedance measurements were carried out at each temperature step, the sample was held at temperature for 1 h to ensure temperature homogeneity.

6.4 Results and discussions

6.4.1 As-sintered samples

Bulk densities of the 6BT (Bi), 6BT (s) and 6BT (Na) ceramics determined using Archimedes method were found to be 95%, 93% and 90% of the theoretical density, respectively, suggesting that relatively high density samples were obtained. Within the resolution of laboratory XRD, all compositions showed a single-phase perovskite with no trace of secondary phases. The stoichiometric compositions did not show any splitting of the characteristic rhombohedral (111) peaks or the characteristic (200) tetragonal peaks, indicating a pseudocubic structure. This result is in agreement with recent studies from both laboratory and synchrotron XRD data in which the crystal structure of the MPB was reported to be nearly cubic [19] or pseudocubic [21, 24]. In the doped compositions, donor-doping did not show any change in the crystal structure, while a slight rhombohedral distortion was observed in acceptor-doped samples.

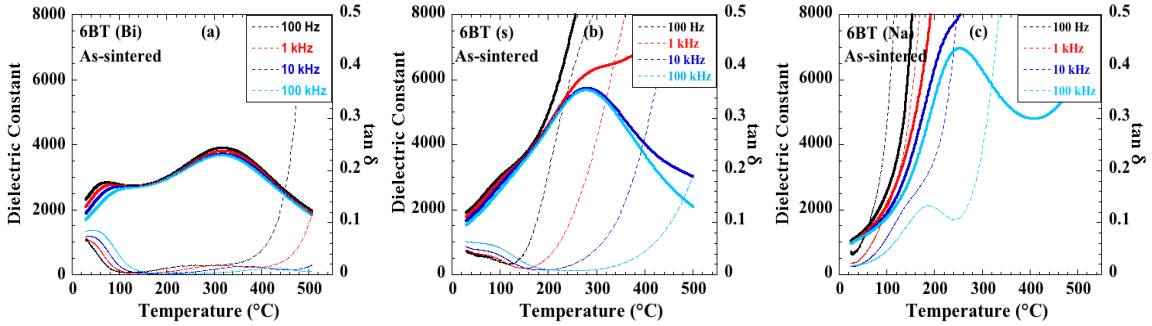

Fig. 6.1 Temperature dependence of the dielectric constant and dielectric loss (tan δ) of as-sintered (a) 6BT (Bi), (b) 6BT (s) and (c) 6BT (1Na)

Figure 6.1 shows temperature dependence of the dielectric constant and dielectric loss (tan δ) of donor, stoichiometric and acceptor-doped 6BT compositions. For the stoichiometric 6BT (s) sample, an anomalously high dielectric constant was measured at relatively low frequencies (e.g. 100 Hz and 1 kHz) and high dielectric losses were observed. This could be attributed to the presence of Bi and Na vacancy defects (V_{Bi}''', V_{Na}') which were generated during the high temperature sintering process along with their compensating positively charged defects ($V_O^{\cdot\cdot}$, $h^{\cdot}$) as shown in equation (6.1):

$$e' + 3[V_{Bi}'''] + [V_{Na}'] = 2[V_O^{\cdot\cdot}] + h^{\cdot} \quad (6.1)$$

A further deterioration in the dielectric properties was observed in acceptor-doped (1% Na excess) compositions as seen in Fig. 6.1 (c). Due to the similar ionic radii between Bi ($r_{Bi^{3+}}$ = 1.34 Å) [31] and Na ($r_{Na^{+}}$ = 1.39 Å) [32], some excess Na could replace Bi and result in a negatively charged defect Na_{Bi}'', thus leading to a further increase in compensating oxygen vacancies and/or holes as shown in equation (6.2). This would explain the degradation of the dielectric properties as seen in Figure 6.1 (c).

$$e' + 3[V_{Bi}'''] + [V_{Na}'] + 2[Na_{Bi}''] = 2[V_O^{\cdot\cdot}] + h^{\cdot} \quad (6.2)$$

In contrast, a significant improvement in dielectric properties was observed in donor doped 6BT (2% Bi excess) as seen from a persistence of low dielectric loss (< 3% at 1 kHz) up to high temperature (450°C) and the disappearance of the anomalous high

dielectric constant at low frequencies. There are two likely reasons for this result. First, excess Bi compensates for Bi loss during sintering, leading to a decrease in both V_{Bi}''' defects and the corresponding positively charged defects ($V_O^{\cdot\cdot}$ and $h^{\cdot}$) [33]. Second, it is most likely that some excess Bi substitutes for Na which results in the formation of positively charged $Bi_{Na}^{\cdot\cdot}$ defects which then need to be compensated either by an increase in negatively charged defects (e.g. V_{Bi}''' , V_{Na}', e') or by a decrease in positively charged defects (i.e. $V_O^{\cdot\cdot}$, $h^{\cdot}$). However, due to the observation of improved dielectric properties, it is most likely that the latter is a dominant mechanism.

$$e' + 3[V_{Bi}'''] + [V_{Na}'] + 2[Na_{Bi}''] = 2[V_O^{\cdot\cdot}] + h^{\cdot} + 2Bi_{Na}^{\cdot\cdot} \qquad (6.3)$$

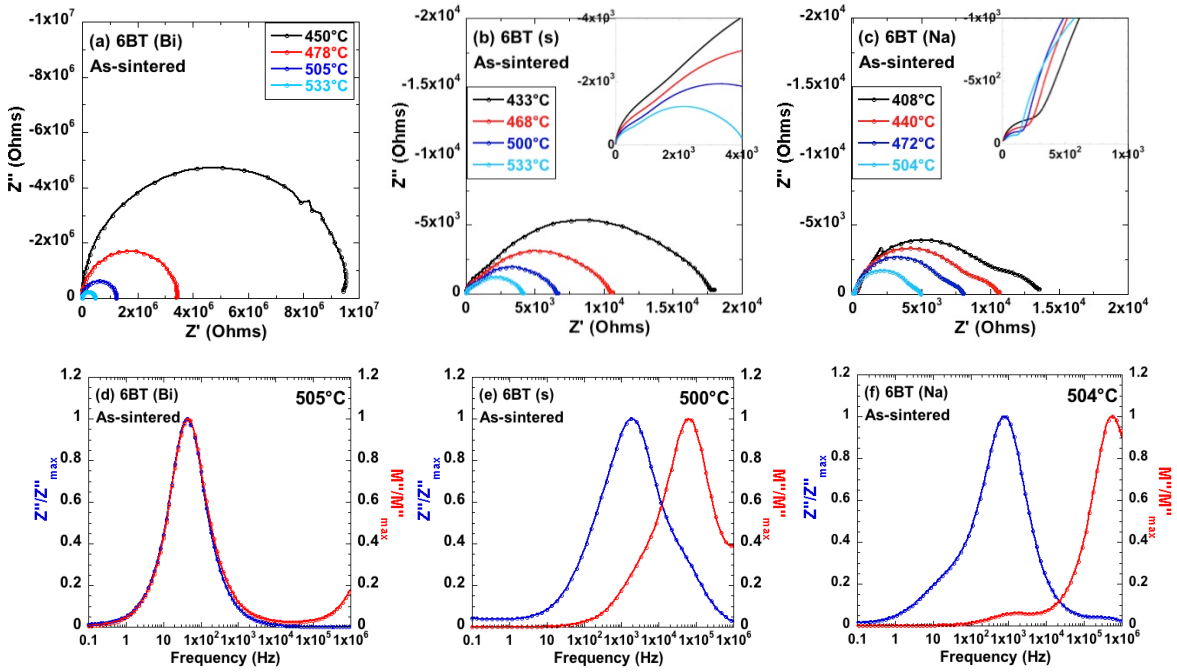

Fig. 6.2. Complex plane plots of (a) 6BT (Bi), (b) 6BT (s) and (c) 6BT (Na) compositions with the inset in (b) and (c) showing the high frequency data on an enlarged scale to highlight the bulk response. Corresponding normalized Z'' and M'' spectroscopic plots at ~500 °C are shown for (d) 6BT (Bi), (e) 6BT (s) and (f) 6BT (Na)

To gain a better understanding about the influence of A-site acceptor- and donor-doping on the conductivity and electrical structure, impedance spectroscopy measurements were conducted at different frequencies and temperatures. Impedance complex plane plots (Z* plot) for 6BT (Bi), 6BT (s) and 6BT (Na) are shown in Fig. 6.2.

For the stoichiometric composition (6BT (s), Fig. 6.2 (b)), the Z* plots at all temperatures feature a slightly distorted semicircle at low frequency corresponding to the grain-boundary response and a much smaller second semicircle at higher frequency corresponding to the bulk response which can be seen more clearly in an enlarged scale in the inset of Fig. 6.2 (b). The corresponding spectroscopic plots of the imaginary

component of the impedance (Z'') and electric modulus (M'') are shown in Fig. 6.2 (e). Since the Debye-like peak magnitude is weighted according to the R value in the Z'' spectra and the C^{-1} value in the M'' spectra, a region with relatively higher resistance and capacitance (i.e. grain boundary) will appear as a dominant peak in the Z'' spectra and a minor peak in the M'' spectra [30, 34], which agrees well with Z'' and M'' peak characteristics shown in the low frequency data of Fig. 6.2 (e). Accordingly, a region with lower resistance and capacitance (i.e. bulk) will display the opposite characteristics (i.e. a dominant peak in the M'' spectra and a minor peak in the Z'' spectra), which can be seen in high frequency data in Fig. 6.2 (e). In addition, at 500 °C, the dielectric constant extracted from capacitance associated with high frequency semicircle is ~ 1970, which is in a good agreement with high frequency bulk dielectric constant obtained from direct dielectric measurement shown in Fig. 6.1 (b). These two observations confirm the assignment of the peaks to the bulk and grain boundary components.

Similar to the 6BT (s) composition, acceptor-doped compositions (6BT (Na), Fig. 6.2 (c)) showed two semicircles corresponding to bulk and grain boundary components, indicating that an electrically inhomogeneous microstructure was present. However, compared to 6BT(s), both the bulk and grain boundary resistivity significantly decreased in magnitude as seen in Table 6.1. In addition, it could also be seen from Table 6.1 that acceptor-doping resulted in a modest decrease in grain boundary resistivity but a considerable decrease (~ one order of magnitude lower) in bulk resistivity. This could suggest that the effect of acceptor-doping is not limited to the grain boundary but the bulk was also affected. On the other hand, one can infer from this result that the observed

changes in dielectric properties might be related more to the properties of the bulk than that of the grain boundary. This finding is consistent with the study of Yoon *et al.* on Mg-doped $BaTiO_3$ which found a substantial change in bulk resistivity along with a small change in grain boundary resistivity [35]. The corresponding Z'' and M'' spectroscopic plots of 6BT (Na) are shown in Fig. 6.2 (f). In the Z'' spectroscopic plot, due to a considerable decrease in bulk resistivity, a previously observed shoulder at high frequency corresponding to the bulk response in 6BT (s) was nearly absent in 6BT (Na). In addition, it should be noted that a shoulder appeared at a very low frequencies (~10 Hz) which likely corresponds to an ionic conduction mechanism which was not noticeable in the data of 6BT (s) [30].

Table 6.1 A comparison of bulk and grain boundary resistivity (ρ) among 6BT (Bi), 6BT (s) and 6BT (Na) at selected temperatures. Due to the electrical homogeneity of 6BT (Bi), only the bulk component resistivity is shown.

Compositions	**Resistivity (ρ, Ω.cm)**					
	~ 440 °C		~470 °C		~500 °C	
	bulk	gb	bulk	gb	bulk	gb
6BT (Bi)	$1.4x10^8$	-	$5.0x10^7$	-	$1.8x10^7$	-
6BT (s)	$3.4x10^4$	$1.3x10^5$	$2.2x10^4$	$7.4x10^4$	$1.5x10^4$	$4.6x10^4$
6BT (Na)	$3.0x10^3$	$8.6x10^4$	$2.2x10^3$	$6.9x10^4$	$1.5x10^3$	$4.4x10^4$

In contrast, within the measured frequency range used, the Z^* plot of donor-doping (6BT (Bi)) exhibited a single semicircle as seen in Fig. 6.2 (a) indicating that sample was electrically homogeneous. At 500 °C, the dielectric constant extracted from

capacitance values associated with this semicircle was ~ 2,300 which agrees well with the high frequency dielectric constant obtained from direct dielectric measurement at the same temperature shown in Fig. 6.1 (a), thus confirming that it originates from the bulk. Compared to 6BT (s), it can be seen from Table 6.1 that donor-doping resulted in an increase in bulk resistivity by 3 to 4 orders of magnitude. This is consistent with recent studies on Bi-excess compositions in $Bi_{0.5}Na_{0.5}TiO_3$ (BNT) by Li *et al* [30]. The corresponding Z'' and M'' spectroscopic plots are shown in Fig. 6.2 (d) where the Z'' and M'' peaks were coincident at the same frequency, confirming that the sample is electrically homogeneous.

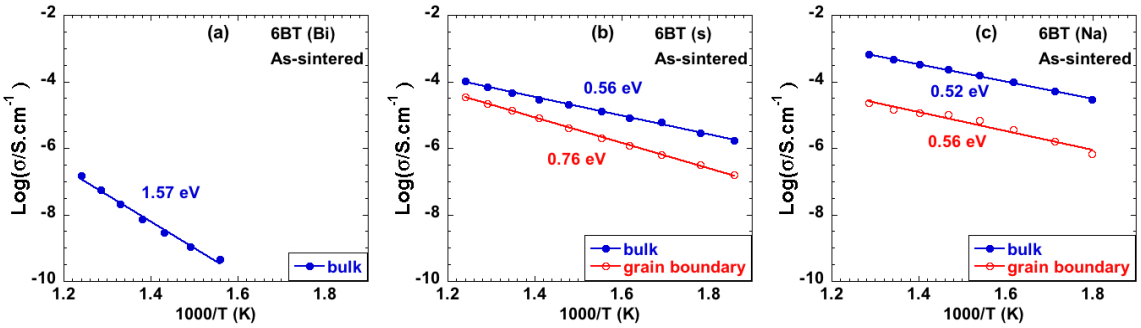

Fig. 6.3 Arrhenius-type plots of the bulk and grain boundary conductivity for (a) 6BT (Bi), (b) 6BT (s) and (c) 6BT (Na). Only the bulk component is shown in the 6BT (Bi) sample due to the electrically homogeneous structure.

Arrhenius-type plots for all the three compositions are shown in Fig. 6.3. The activation energy for the bulk and grain boundary responses for each sample has been determined from analysis of the Arrhenius plots. For the electrically homogeneous 6BT (Bi) composition, an activation energy of 1.57 eV was observed, which is approximately

half of the band gap ($E_g/2$), suggesting that the conduction mechanism in this sample is primarily dominated by an intrinsic electronic conduction mechanism [30, 36]. In contrast, for 6BT (s) and 6BT (Na) the activation energies for the bulk and grain boundary component ranged between 0.5-0.7 eV, which is consistent with conduction mechanisms dominated by extrinsic defects [30][34].

The observed increase in the resistivity of donor-doped compositions (6BT (Bi)) seen in the impedance data agrees well with the observed low tan δ values seen in the dielectric measurements. Similarly, a decrease in resistivity seen in acceptor-doped (6BT (Na)) compositions was also consistent with the observation of high dielectric loss values. The trend in the change in resistivity with doping suggests that p-type charge carriers (e.g. $[V_O^{\cdot\cdot}], h^{\cdot}$) are dominant in the stoichiometric 6BT (s) composition. Furthermore, Li *et al.* [30] reported that the oxygen ionic transport number (t_i) in stoichiometric and Mg acceptor-doped BNT was greater than 0.9 suggesting that the conduction mechanism in the 6BT (s) specimen in this study may be dominated by oxygen vacancies ($V_O^{\cdot\cdot}$) as well.

6.4.2 Annealing effects

Samples subjected to annealing in air at 800°C for 7 days showed no noticeable change in crystal structure. The XRD data of all samples showed a single perovskite phase with no trace of secondary phase. A pseudocubic structure similar to as-sintered sample was still observed, indicating that there is no change in long-range order after

annealing. Figure 6.4 shows temperature dependence of dielectric constant and dielectric loss of all annealed samples. For donor-doping (6BT (Bi), Fig. 6.4 (a)) and acceptor-doping (6BT ((Na), Fig. 6.4 (c)), the dielectric properties remained almost the same as compared to the as sintered samples. For 6BT (Bi), while no change in dielectric constant was observed, it should be noted that a high dielectric loss values shifted to slightly lower temperatures. For 6BT (Na), both the dielectric constant and dielectric loss values remained nearly the same.

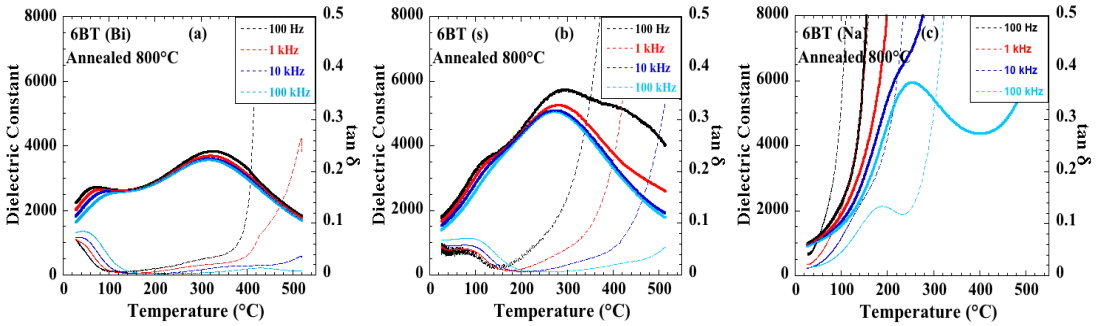

Fig. 6.4 Temperature dependence of dielectric constant and dielectric loss (tan δ) for (a) 6BT (Bi), (b) 6BT (s) and (c) 6BT (Na) samples, which was annealed in air at 800 °C for 7 days.

In contrast, a significant improvement in dielectric properties was clearly observed in the stoichiometric composition, 6BT (s), where a considerable decrease in the dielectric loss and a decrease in the anomalously high dielectric constant at 100 Hz at temperatures above 300°C was clearly evident. This suggests that the concentration of electrically active defects in this composition substantially decreased after annealing.

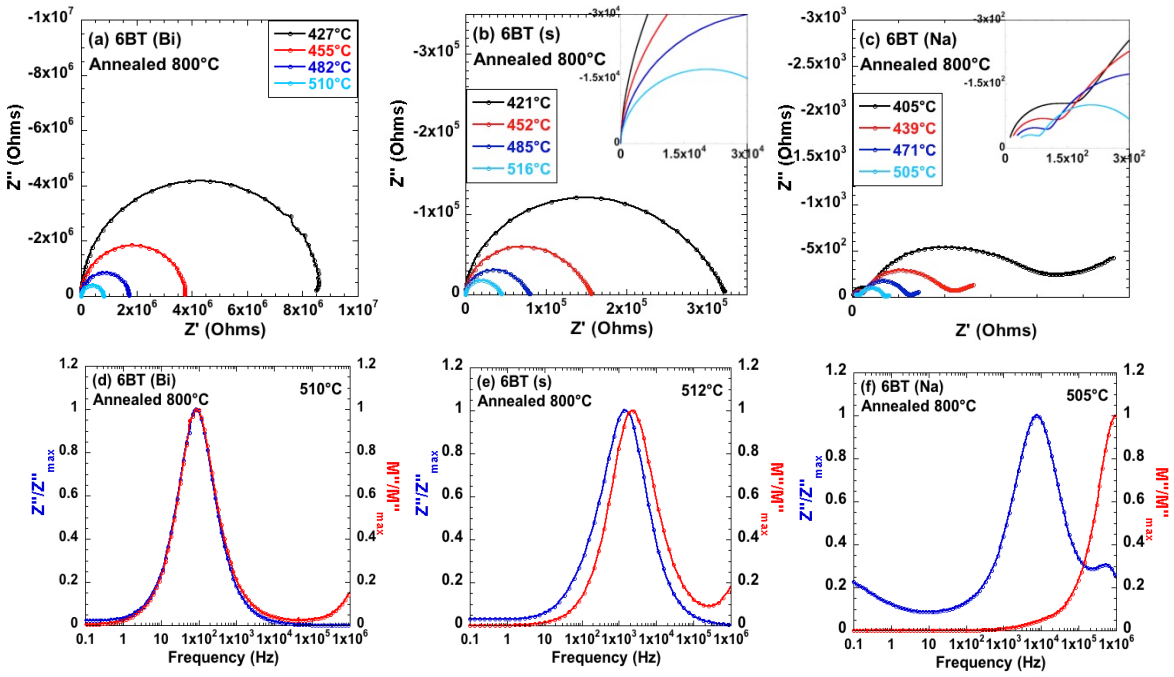

Fig. 6.5 Complex plane plots for annealed samples of (a) 6BT (Bi), (b) 6BT (s) and (c) 6BT (Na) compositions with an inset in (b) and (c) to include high frequency data on an enlarged scale to highlight the bulk response. Corresponding normalized Z'', M'' spectroscopic plots at ~500 °C are shown for (d) 6BT (Bi), (e) 6BT (s) and (f) 6BT (Na)

Impedance spectroscopy was performed on these annealed specimens to provide a greater analysis of the defect mechanisms in this series of compositions. The complex plane plots and corresponding Z'', M'' spectroscopic plots of each compositions are shown in Fig. 6.5 (a)-(f). For the donor-doped composition (6BT (Bi)), a single semicircle (Fig. 6.5 (a)) as well as coincident $Z''$and M''peaks (Fig. 6.5 (d)) were observed, indicating that the 6BT (Bi) sample remained electrically homogeneous as it was for the as sintered sample. A small decrease in the resistivity was observed after annealing as seen in Table 6.2, which supports the finding of the increase in dielectric loss shown in Fig. 6.4 (a). For the annealed acceptor-doped sample 6BT (1Na) (Fig. 6.5

(c)), two semicircles was clearly observed corresponding to bulk and grain boundary components similar to that of the as-sintered sample, suggesting that the sample is still electrically heterogeneous. Similar to 6BT (Bi), annealing also resulted in a small decrease of resistivity as seen in Table 6.2.

As opposed to the doped annealed samples 6BT (Bi) and 6BT (Na), a significant change in the impedance response was observed in annealed 6BT (s) sample as seen from a single semicircle in Fig. 6.5 (b) and the corresponding coincident $Z''$and M''peaks in Fig. 6.5 (e). In addition, an increase in the resistivity by one order of magnitude was observed as seen in Table 6.2, which is consistent with the overall improvement in dielectric properties.

Table 6.2 A comparison of bulk and grain boundary resistivity (ρ) for each composition before and after annealing at 800 °C for 7 days. Only the bulk component was shown for 6BT (Bi) and 6BT (s) sample due to homogeneity.

Compositions	**Resistivity at ~ 500 °C (ρ, Ω.cm)**			
	As sintered		**Annealed 800 °C 7 days**	
	bulk	gb	bulk	gb
6BT (Bi)	$1.8x10^7$	-	$1.0x10^7$	-
6BT (s)	$1.5x10^4$	$4.6x10^4$	$3.9x10^5$	-
6BT (Na)	$1.5x10^3$	$4.4x10^4$	$5.8x10^2$	$2.4x10^3$

Arrhenius plots of the bulk and grain boundary conductivity of all annealed samples are shown in Fig. 6.6 (a)-(c). For the 6BT (Bi) sample, annealing resulted in a

minor decrease in the activation energy from 1.57 eV to 1.23 eV whereas for the stoichiometric 6BT (s) sample E_a increased significantly from 0.56 eV to1.00 eV. For annealed acceptor-doped sample 6BT (Na), the bulk activation energy was unchanged, whereas the grain boundary activation energy increased from 0.56 to 0.70 eV upon annealing.

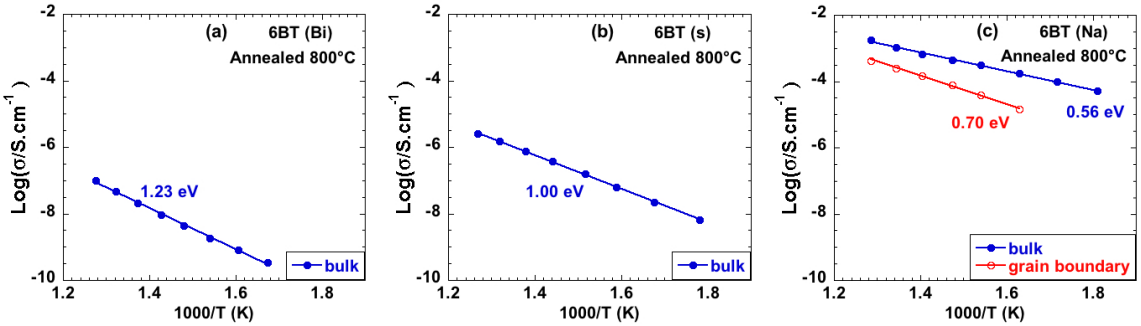

Fig. 6.6 Arrhenius-type plot of bulk and grain boundary conductivity for annealed (a) 6BT (Bi), (b) 6BT (s) and (c) 6BT (Na). Only bulk component is shown in 6BT (2% Bi) and 6BT (s) samples due to electrically homogeneity.

The significant improvement in electrical homogeneity and resistivity in the annealed stoichiometric sample 6BT (s) but the absence of any significant change in the doped 6BT (Bi) and 6BT (Na) samples can be explained with two competing mechanisms: (1) the loss of volatile cations Bi and Na, which can leads to additional oxygen loss and (2) a re-oxidation process, which can reduce the oxygen vacancy concentration. For the stoichiometric composition, the concentration of oxygen vacancies established from the initial as-sintered sample decreased during the anneal due to the re-oxidation process, thus resulting in an electrically homogeneous structure and an increase in resistivity.

6.5 Conclusions

Single-phase perovskite for $0.94(Bi_{0.5}Na_{0.5})TiO_3$-$0.06BaTiO_3$ ceramics were prepared with stoichiometric compositions as well as compositions incorporating A-site donors (through Bi excess) and A-site acceptor doping (through Na excess). All of the sintered ceramics exhibited pseudo-cubic symmetry using laboratory scale XRD. Significant improvements in dielectric properties were observed including low dielectric loss in donor-doped compositions. In contrast, deterioration in dielectric properties including an increase in dielectric loss was observed with acceptor-doping. Impedance spectroscopy revealed that stoichiometric and acceptor-doped compositions had an electrically heterogeneous microstructure. In addition, it was observed that acceptor doping resulted in a decrease in the resistivity by one order of magnitude with respect to stoichiometric 6BT. In contrast, donor doping resulted in an electrically homogeneous microstructure with an increase in resistivity by over three orders of magnitudes and the associated activation energy was 1.57 eV ($E_a \sim \frac{1}{2}E_g$), suggesting intrinsic electronic conduction as the primary conduction mechanism. Annealing studies revealed that homogeneity and resistivity of compositions with moderate oxygen vacancy concentrations (i.e. 6BT (s)) could be improved. This study confirms that small changes in the A-site stoichiometry in $0.94(Bi_{0.5}Na_{0.5})TiO_3$-$0.06BaTiO_3$ can result in a large changes in electrical properties, from highly insulating behavior in donor-doped compositions to ionic conduction in acceptor-doped compositions.

6.6 References

1. Haertling, G.H., *Ferroelectric ceramics: history and technology.* Journal of the American Ceramic Society, 1999. **82**(4): p. 797-818.

2. Varghese, J., et al., *Fabrication of arrays of lead zirconate titanate (PZT) nanodots via block copolymer self-assembly.* Chemistry of Materials, 2013. **25**(8): p. 1458-1463.

3. *Restriction of the use of certain hazardous substances in electrical and electronic equipment (RoHS)*, in *EU-Directive 2002/95/EC*, O.J.E. Union, Editor 2003.

4. *Law for promotion of effective utilization of resources: Minister of Economy, Trade and Industry, Japan.* 2001.

5. *Solid waste: hazardous electronic waste: U.S. California Senate Bill No. 50.* 2004.

6. *Measures for the Administration on Pollution Control of Electronic Information Products : Ministry of Information Industry China Order No. 39.* 2006.

7. Saito, Y., et al., *Lead-free piezoceramics.* Nature, 2004. **432**(7013): p. 84-87.

8. Smolenskii, G., et al., *New ferroelectrics of complex composition.* Sov. Phys. Solid State, 1961. **2**(11): p. 2651-2654.

9. Nagata, H., et al., *Piezoelectric properties of bismuth sodium titanate ceramics.* Developments in Dielectric Materials and Electronic Devices, 2012: p. 213-221.

10. Chen, M., et al., *Structure and electrical properties of $(Na_{0.5}Bi_{0.5})_{1-x}Ba_xTiO_3$ piezoelectric ceramics.* Journal of the European Ceramic Society, 2008. **28**(4): p. 843-849.

11. Xu, C., D. Lin, and K. Kwok, *Structure, electrical properties and depolarization temperature of $(Bi_{0.5}Na_{0.5})TiO_3$-$BaTiO_3$ lead-free piezoelectric ceramics.* Solid state sciences, 2008. **10**(7): p. 934-940.

12. Takenaka, T., K.-I. Maruyama, and K. Sakata, *$(Bi_{1/2}Na_{1/2})TiO_3$−$BaTiO_3$ system for lead-free piezoelectric ceramics.* Japanese Journal of Applied Physics, 1991. **30**(9B): p. 2236-2239.

13. Yoshii, K., et al., *Electrical properties and depolarization temperature of $(Bi_{1/2}Na_{1/2})TiO_3$-$(Bi_{1/2}K_{1/2})TiO_3$ lead-free piezoelectric ceramics.* Japanese journal of applied physics, 2006. **45**: p. 4493.

14. Zhang, S.-T., et al., *Lead-free piezoceramics with giant strain in the system $Bi_{0.5}Na_{0.5}TiO_3$–$BaTiO_3$–$K_{0.5}Na_{0.5}NbO_3$. I. Structure and room temperature properties.* Journal of Applied Physics, 2008. **103**(3): p. 034107.

15. Takenaka, T., T. Okuda, and K. Takegahara, *Lead-free piezoelectric ceramics based on $(Bi_{1/2}Na_{1/2})TiO_3$-$NaNbO_3$.* Ferroelectrics, 1997. **196**(1): p. 175-178.

16. Xu, Q., et al., *Structure and electrical properties of $(Na0.5Bi_{0.5})_{1-x}Ba_xTiO_3$ ceramics made by a citrate method.* Journal of Electroceramics, 2008. **21**(1-4): p. 617-620.

17. Chu, B.-J., et al., *Electrical properties of $Na_{1/2}Bi_{1/2}TiO_3$-$BaTiO_3$ ceramics.* Journal of the European Ceramic Society, 2002. **22**(13): p. 2115-2121.

18. Jo, W., et al., *Evolving morphotropic phase boundary in lead-free $(Bi_{1/2}Na_{1/2})TiO_3$–$BaTiO_3$ piezoceramics.* Journal of Applied Physics, 2011. **109**(1): p. 014110.

19. Ranjan, R. and A. Dviwedi, *Structure and dielectric properties of $(Na_{0.50}Bi_{0.50})_{1-x}Ba_xTiO_3$: $0 \leq x \leq 0.10$.* Solid state communications, 2005. **135**(6): p. 394-399.

20. Zhang, S.-T., et al., *Giant Strain in Lead-Free Piezoceramics $Bi_{0.5}Na_{0.5}TiO_3$–$BaTiO_3$–$K_{0.5}Na_{0.5}NbO_3$ System.* Applied Physics Letters, 2007. **91**(11): p. 112906-112906-3.

21. Simons, H., et al., *Electric-field-induced strain mechanisms in lead-free 94%$(Bi_{1/2}Na_{1/2})TiO_3$–6%$BaTiO_3$.* Applied Physics Letters, 2011. **98**(8): p. 082901.

22. Ma, C. and X. Tan, *Phase diagram of unpoled lead-free–ceramics.* Solid State Communications, 2010. **150**(33): p. 1497-1500.

23. Ma, C. and X. Tan, *In situ Transmission Electron Microscopy Study on the Phase Transitionsin Lead-Free $(1-x)(Bi_{1/2}Na_{1/2})TiO_3$–$xBaTiO_3$ Ceramics.* Journal of the American Ceramic Society, 2011. **94**(11): p. 4040-4044.

24. Daniels, J.E., et al., *Electric-field-induced phase transformation at a lead-free morphotropic phase boundary: Case study in a 93%$(Bi_{0.5}Na_{0.5})TiO_3$–7% $BaTiO_3$.* Applied Physics Letters, 2009. **95**(3): p. 032904-032904-3.

25. Rödel, J., et al., *Perspective on the Development of Lead-free Piezoceramics.* Journal of the American Ceramic Society, 2009. **92**(6): p. 1153-1177.

26. Jo, W., et al., *On the phase identity and its thermal evolution of lead free $(Bi_{1/2}Na_{1/2})TiO_3$-6mol%$BaTiO_3$.* Journal of Applied Physics, 2011. **110**(7): p. 074106.

27. Hiruma, Y., H. Nagata, and T. Takenaka, *Thermal depoling process and piezoelectric properties of bismuth sodium titanate ceramics.* Journal of Applied Physics, 2009. **105**(8): p. 084112-084112-8.

28. Sung, Y., et al., *Effects of Bi nonstoichiometry in $(Bi_{0.5+x}Na)TiO_3$ ceramics.* Applied Physics Letters, 2011. **98**(1): p. 012902.

29. Li, M., Zhang, Huairuo, Zhang, Cook, Stuart N, Li, Linhao, Kilner John A, Reaney, Ian M, Sinclair, Derek C, *The dramatic influence of A-site non-stoichiometry on the electrical conductivity and conduction mechanisms in the perovskite oxide $Na_{0.5}Bi_{0.5}TiO_3$.* Chemistry of Materials, 2015. **27**: p. 629-634.

30. Li, M., et al., *A family of oxide ion conductors based on the ferroelectric perovskite $Na_{0.5}Bi_{0.5}TiO_3$.* Nature materials, 2014. **13**(1): p. 31-35.

31. Eitel, R.E., et al., *New high temperature morphotropic phase boundary piezoelectrics based on $Bi(Me)O_3$–$PbTiO_3$ ceramics.* Japanese Journal of Applied Physics, 2001. **40**(10R): p. 5999.

32. Shannon, R.t., *Revised effective ionic radii and systematic studies of interatomic distances in halides and chalcogenides.* Acta Crystallographica Section A: Crystal Physics, Diffraction, Theoretical and General Crystallography, 1976. **32**(5): p. 751-767.

33. Eichel, R.-A., *Structural and dynamic properties of oxygen vacancies in perovskite oxides—analysis of defect chemistry by modern multi-frequency and pulsed EPR techniques.* Physical Chemistry Chemical Physics, 2011. **13**(2): p. 368-384.

34. Morrison, F.D., D.C. Sinclair, and A.R. West, *Characterization of Lanthanum-Doped Barium Titanate Ceramics Using Impedance Spectroscopy.* Journal of the American Ceramic Society, 2001. **84**(3): p. 531-538.

35. Yoon, S.H., C.A. Randall, and K.H. Hur, *Effect of Acceptor (Mg) Concentration on the Resistance Degradation Behavior in Acceptor (Mg)-Doped BaTiO3 Bulk Ceramics: I. Impedance Analysis.* Journal of the American Ceramic Society, 2009. **92**(8): p. 1758-1765.

36. Bousquet, M., et al., *Optical properties of an epitaxial $Na_{0.5}Bi_{0.5}TiO_3$ thin film grown by laser ablation: Experimental approach and density functional theory calculations.* Journal of Applied Physics, 2010. **107**(10): p. 104107.

7 Summary

In this chapter, the role of A-site non-stoichiometry on dielectric, ferroelectric, piezoelectric and transport properties of lead free piezoelectric ceramics based on compositions in the 1-x($Bi_{0.5}Na_{0.5}TiO_3$)-$x$$BaTiO_3$ system near the MPB will be summarized based on the results outlined in the previous chapters.

In summary, a single-phase perovskite with no trace of secondary phases was obtained for both donor- and acceptor-doping, within the resolution of the x-ray diffraction instrument used in these studies. However, while donor-doping had little or no effect on the crystal structure, acceptor-doping promoted rhombohedral distortions. Significant improvements in the dielectric properties were seen for all donor-doped compositions and a deterioration in the dielectric properties was observed in all acceptor-doped compositions. Compared to the stoichiometric composition, a significant increase in coercive field (E_c) was observed in all acceptor-doped compositions, which can be attributed to domain wall pinning as is typically found in hard PZT. The increased E_c was confirmed via PUND tests and remanent P-E hysteresis data, indicating that this finding is an example of true hardening rather than an artifact from conduction losses. In addition, all A-site acceptor-doped compositions exhibited an increase in mechanical quality factor (Q_m) as well as a decrease in d_{33}, tan δ, P_r and ε_r, which are all the typical characteristics of "hardening" observed in acceptor-doped PZT. Hardening characteristics were attributed to the simultaneous occurrence of a long-range domain

structure and a clamping of the domain structures by defect dipoles. Shown in Table 7.1 are the values of ε_r, tan δ, E_c, P_r, d_{33} and Q_m, for donor-, stoichiometric and acceptor-doped compositions.

Table 7.1 Values of ε_r, tan δ, E_c, P_r, d_{33} and Q_m, for donor-, stoichiometric and acceptor-doped compositions.

***(1-x)*BNT-*x*BT**	ε_r	**tan δ**	E_c* **(kV/cm)**	P_r* **(kV/cm)**	d_{33} (pC/N) 1 h after poling	d_{33} (pC/N) 7 days after poling	Q_m
5.5BT (Bi)	1806	0.043	41.2	29.9	132	126	106
5.5BT (s)	1784	0.042	35.1	16.0	128	120	113
5.5BT (Na)	1150	0.01	38.1	32.3	81	78	246
6BT (Bi)	2113	0.069	37.2	31.4	142	151	69
6BT (s)	1790	0.047	36.9	29.2	125	127	150
6BT (Na)	1054	0.023	42.6	27.0	82	110	323
7BT (Bi)	1808	0.058	22.9	27.4	197	180	67
7BT (s)	1696	0.038	32.0	21.9	148	138	156
7BT (Na)	1042	0.021	36.5	19.0	44	48	196

* E_c and P_r obtained from the remanent *P-E* hysteresis measurement

To gain a greater insight into these phenomena, impedance spectroscopy was conducted on selected compositions. Impedance spectroscopy revealed that stoichiometric and acceptor-doped compositions had an electrically heterogeneous microstructure. In addition, it was observed that Na-excess compositions exhibited low

resistivity ($\rho \sim 10^3$ Ω-cm) with characteristic peaks in the impedance data indicating ionic conductivity similar to recent observations of oxide ion conduction in $(Bi_{0.5}Na_{0.5})TiO_3$. In contrast, donor doping resulted in an electrically homogeneous microstructure with an increase in resistivity by over three orders of magnitudes ($\rho \sim 10^7$ Ω-cm) and the associated activation energy was 1.57 eV ($E_a \sim ½E_g$), suggesting intrinsic electronic conduction as the primary conduction mechanism. In addition, annealing studies (800 °C, 7 days) revealed that homogeneity and resistivity could be improved in the stoichiometric composition, which possesses moderate oxygen vacancy.

Based on all of these findings, it can be concluded that a small modification in the A-site stoichiometry of (1-*x*)BNT-*x*BT not only can adjust materials characteristics from "hardening" to "softening", but also can effectively control the defect chemistry and result in significant changes in electrical properties, from highly insulating behavior in donor-doped compositions to ionic conduction in acceptor-doped compositions. Therefore, this study reveals A-site donor doping as a key to solve high leakage current problems and subsequently make it suitable for dielectric and piezoelectric applications. On the other hand, the data from A-site acceptor-doping also reveals *(*1-*x)*BNT-*x*BT as a good candidate for ionic conductor applications. Shown in Fig 7.1 is the Arrhenius plot of bulk conductivity from our study compared to that of a previous study on the BNT system where the Bi-deficient BNT was shown to be a promising candidate for ionic conductor applications.

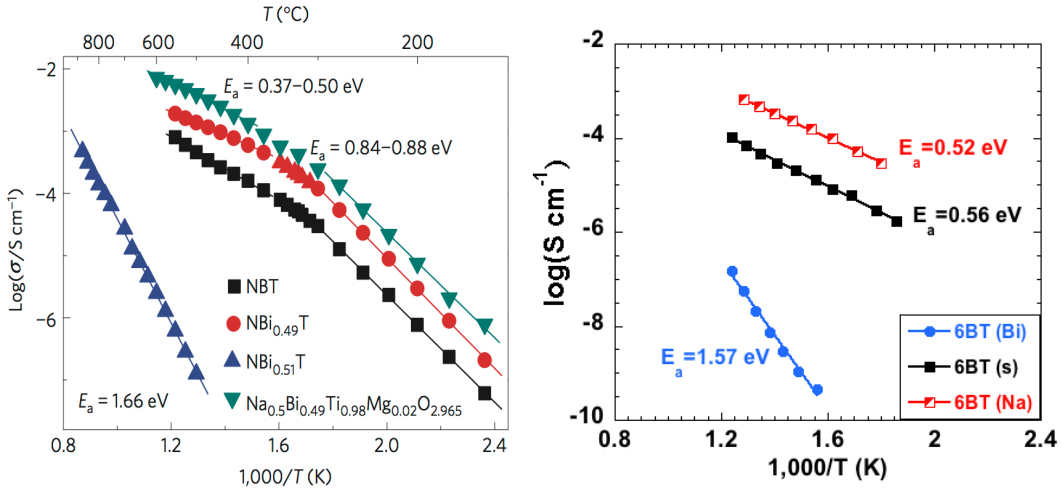

Fig. 7.1 Arrhenius plot of bulk conductivity showing the effect of A-site cation non-stoichiometry in (a) BNT [1] and (b) 0.94BNT-0.06BT (this study).

7.1 References

1. M. Li, M. J. Pietrowski, R. A. De Souza, H. Zhang, I. M. Reaney, S. N. Cook, J. A. Kilner and D. C. Sinclair, *Nature materials*, 2014, 13, 31-35.

8 Future work

This chapter will describe a selection of future studies that will provide more insight into the role of A-site cation non-stoichiometry on (1-x)BNT-xBT. The first section will go over the studies that will be of help in gaining a better understanding regarding the hardening behavior. The second section will go over studies aimed to help develop a comprehensive picture on the effects of A-site non-stoichiometry in regards to the ionic conductor applications.

8.1 Hardening

8.1.1 Relationship between symmetry and hardening in A-site acceptor-doped *(1-x)*BNT-*x*BT by using Rietveld refinements from high resolution synchrotron XRD data

Previous experimental results in this study, including dielectric, ferroelectric and piezoelectric as well as impedance data in all A-site acceptor-doped compositions have shown "hardening" characteristics that were explained based on an enhancement in the long range domain structure and defect chemistry (i.e. domain stabilization from $V_O^{\cdot\cdot}$ or defect dipoles). While defect chemistry has been known to play an important role in controlling the hardening [2], the effect of the symmetry is also of paramount importance as it can directly affect the materials properties like E_c, P_r and others, which are similar to

the effect of hardening. For example, in the study of Nb-doped PZT from Jin *et al.* [3], by varying the Zr/Ti ratio, the structure can be changed from rhombohedral to tetragonal symmetry and the corresponding E_c also increases from ~ 10 kV/cm for rhombohedral phase to ~35 kV/cm for tetragonal phase as seen in Fig. 8.1.

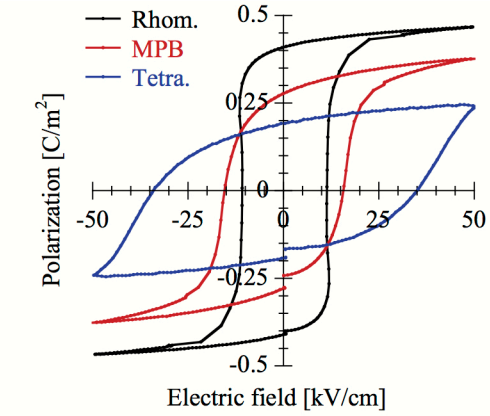

Fig. 8.1 A dependence of *P-E* hysteresis loop on composition (Zr/Ti ratio) in Nb-doped PZT (picture taken from Jin *et al.*[3])

Given that the compositions in this study are near the MPB, excess Na and Bi additions could shift the structure to the rhombohedral or tetragonal side of the MPB. Since it is harder to switch the domain configuration in tetragonal state as compared to the rhombohedral state, it might give a false impression of hardening in our study. Therefore, detailed structural analysis is required to separate the effect of defect-related hardening from the effect of symmetry.

The high resolution X-ray diffraction study was carried out on selected samples at 11-BM beamline, Advance Photon Source (APS), Argonne National laboratory. The 11-BM is a bending magnet beamline, which can operate in the energy range of 15 – 35 keV ($\lambda \sim 1.0 - 0.34$ Å). The data were collected at ambient temperature with a 2θ step of 0.001°. The calibrated x-ray wavelength used was 0.41378(1) Å. The samples were prepared by pulverizing the ceramic pellets and followed by annealing at 400 °C for 24 hours in order to relieve any residual stress from crushing. The preliminary results of high resolution synchrotron X-ray diffraction are discussed below.

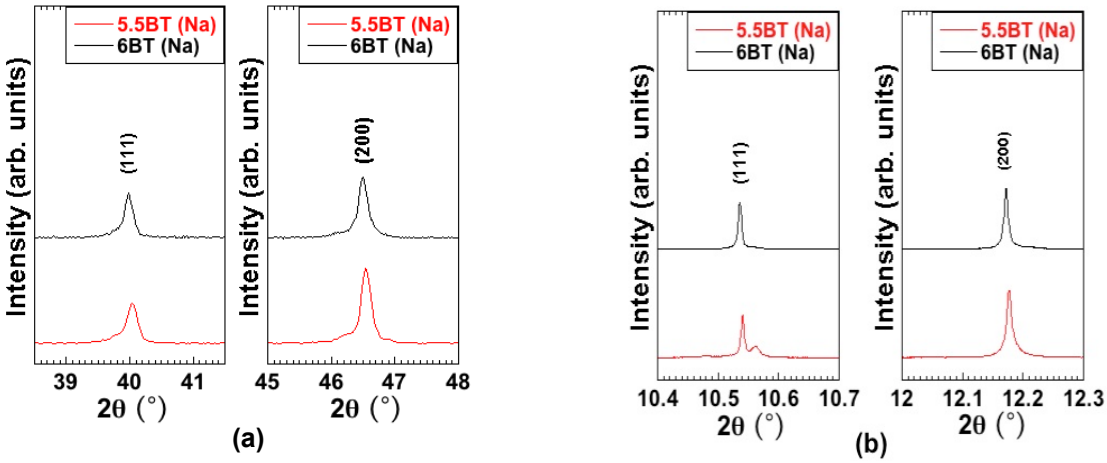

Fig. 8.2 An enlarged 2θ region of (111) and (200) reflections for 5.5BT (Na) and 6BT (Na) obtained from (a) laboratory XRD and (b) high resolution synchrotron XRD

For 5.5BT (Na) and 6BT (Na), the laboratory scale XRD showed an enhancement in the rhombohedral distortion as seen from a broadening of (111) characteristic rhombohedral peak (Fig. 8.2 (a)). The results also agreed with a study of pure BNT in which a transition from rhombohedral to cubic phase was observed after sample was

intentionally prepared with Na-deficiency [4]. However, according to the relatively low resolution of laboratory XRD, the conclusion about the effect of symmetry on hardening could not be definitively stated since there is still some unclear issues. For example, the presence of a small shoulder in the (200) characteristic tetragonal peak (Fig 8.2 (a)), could be evidence of an induced tetragonal phase due to Na-doping or it could be merely a result of a relatively low resolution of laboratory XRD. After performing a high resolution XRD on these samples, a splitting in (111) peak could be resolved and a single sharp (200) peak were observed in 5.5BT (Na) (see Fig. 8.2 (b)), clearly indicating a rhombohedral distortion. In contrast, a single sharp peak was observed in both (111) and (200) peaks of 6BT (Na), indicating pseudocubic symmetry (see Fig. 8.2 (b)). However, a more comprehensive Rietveld refinement is needed in order to extract the constituent phases and discuss their effects with more certainty.

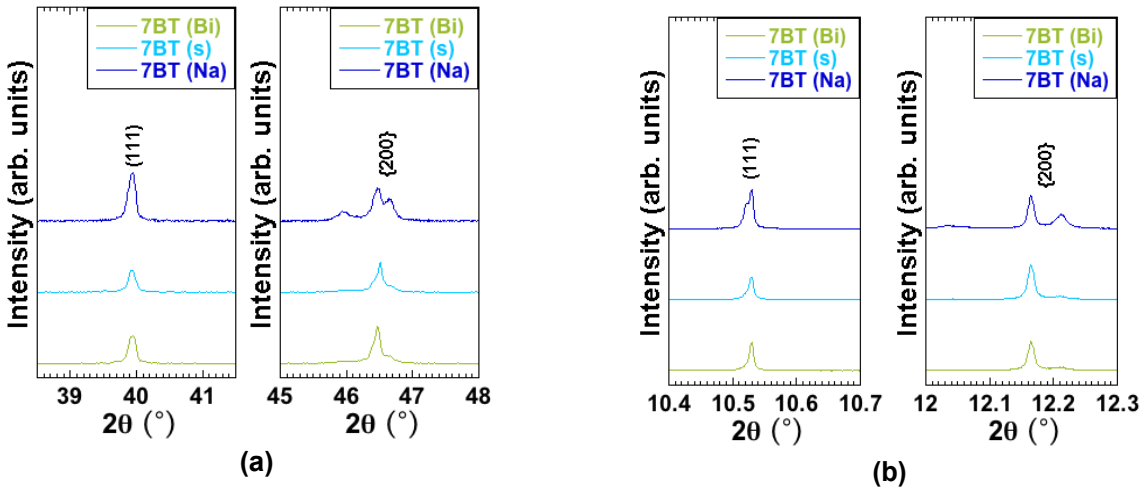

Fig. 8.3 An enlarged 2θ region of (111) and (200) reflections for 7BT (Bi), 7BT (s) and 7BT (Na) from (a) laboratory XRD and (b) high resolution synchrotron XRD

For the 7BT system in which the degree of hardening is the most severe, the laboratory XRD pattern of 7BT (Na) showed obvious splitting of {200} reflections but no splitting in the (111) characteristic rhombohedral peak when compared to that of 7BT (s) (see Fig. 8.3(a)). After conducting high resolution synchrotron XRD on these samples, synchrotron XRD data revealed a splitting in both the (111) characteristic rhombohedral and (200) characteristic tetragonal peaks, indicating that both phases coexist in 7BT (Na). In order to gain more insight to the relationship between symmetry and hardening, Rietveld refinement should be systematically performed on 7BT (Bi), 7BT (s) and 7BT (Na) in order to extract the constituent phases and determine the percentages of each phase for these compositions.

8.1.2 Investigation of domain stabilization through thermally stimulated depolarization current (TSDC) measurement and temperature dependent strain

In terms of applications, the depolarization temperature (T_d) is an important figure of merit for piezoelectric materials, as it determines the upper limit for the temperature at which it can be operated. Thus, a higher T_d is more favorable as it provides a wider temperature range for device operation [5]. Commonly, the $T_{F\text{-}R}$, which is obtained from the temperature dependence of the dielectric measurement on poled samples ($\varepsilon'(T)$), is assumed to be identical to the T_d obtained from thermally stimulated depolarization current (TSDC) measurements due to a good agreement between T_d and $T_{F\text{-}R}$ in PLZT [6] and $BaTiO_3$ [7]. However, this is not true for *(1-x)*BNT-*x*BT system as shown in a recent study by Sapper *et al.* [8] in which T_d and $T_{F\text{-}R}$ involved different mechanisms and T_d is always lower than $T_{F\text{-}R}$. The study explained that T_d is the point

where the macroscopic polarization starts to decay due to a fluctuation of the domains from thermal activation (i.e. the coherence of dipoles within the domain still persist) whereas the T_{F-R} is the point where the domains break up into PNRs (i.e. the loss of long range order between the dipoles). Thus, for most applications, T_d is the more appropriate parameter, as it is the onset temperature at which the material properties begin to deteriorate.

In this study, T_d obtained from TSDC measurements will be of help in understanding the effects of A-site non-stoichiometry on the domain stabilization. In TSDC experiments, the samples will be poled at their optimized conditions and then the current will be measured during heating by using high precision ampere meter [8]. The peak in current-temperature plot directly corresponds to T_d. For acceptor-doped compositions in which the domains are stabilized, T_d is expected to increase with respect to stoichiometric compositions, while donor-doped compositions are expected to show opposite results. To further confirm the TSDC result, the electromechanical strain will be measured as a function of temperature. The temperature at which the negative strain disappears should be consistent with the result obtained from TSDC.

8.2 *(1-x)*BNT-*x*BT as a potential ionic conductor

8.2.1 Direct determination of transport species through impedance spectroscopy under different oxygen partial pressure and electromotive force measurement (EMF)

From impedance spectroscopy measurements, an increase in resistivity via donor-doping and a decrease in resistivity via acceptor doping indicates that p-type charge carriers (e.g. $V_O^{\cdot\cdot}, h^{\cdot}$) are dominant in the stoichiometric 6BT (s) sample. While the primary charge carriers are most likely oxygen vacancies ($V_O^{\cdot\cdot}$) due to similar results between this study and the recent study on the BNT system [1] direct evidence is still needed in our system in order to confirm this observation. Therefore, impedance spectroscopy data should be collected under different atmospheres (e.g. N_2 and O_2) down to low frequency (~ 1 mHz). For donor-doped compositions (e.g. 6BT (Bi)), where n-type electronic conduction is the dominant mechanism, the arc associated with bulk response (R_b) is expected to be pO_2 dependent. For example, a decrease of R_{bulk} should be observed under N_2 atmosphere (i.e. reducing atmosphere) due to an increase in electron concentration. For acceptor-doped compositions, where either $h^{\cdot}$ or $V_O^{\cdot\cdot}$ could be the dominant charge carrier, R_{bulk} should be pO_2 dependent if the conduction is dominated by holes and it should be independent for a limited range of pO_2 if $V_O^{\cdot\cdot}$ is the dominant conduction species.

It should be noted that the complex impedance response is the sum of electronic (σ_{eon}) and ionic (σ_{ion}) conducting contributions. Typically an electrode like silver partially blocks the ionic conducting species. Consequently, apart from high frequency

bulk and grain boundary, the Warburg element at a very low frequency, which is a response due to space charge polarization contribution, is observed as seen in Fig. 8.4. Collecting the IS data down to a very low frequency (~1 mHz) will allow us to get a full analysis of the Warburg element and the ionic transference number (t_{ion}) could be obtained according to following equation:

$$t_{ion} = \frac{\sigma_{ion}}{\sigma_{total}} = \frac{R^{tot}}{R^{ion}} = \frac{R^{eon} - R^{tot}}{R^{eon}} \tag{8.1}$$

Thus, for the acceptor-doped composition (e.g. 6BT (Na)), if $V_{\ddot{O}}$ is the dominant carrier species, the transference number should be close to unity.

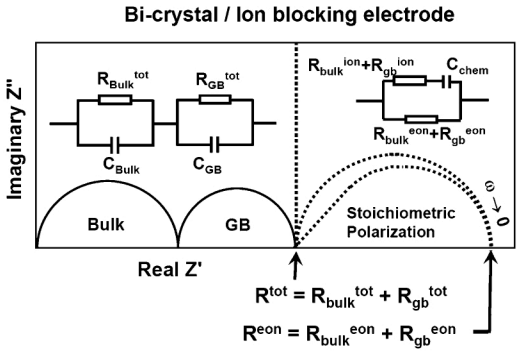

Fig. 8.4 A schematic representation of the impedance spectrum showing a contribution from bulk, grain boundary (GB) and Warburg element (picture taken from [9])

Another effective method that can directly tell the ionic transference number (t_i) is the EMF measurement. An EMF measurement consists of creating different oxygen partial pressures on either side of the sample and measuring the voltage across the

sample. This voltage is then compared to the ideal value, which can be calculated using Nernst equation as following:

$$E_{Nernst} = -\frac{RT}{nF} ln \frac{p_2}{p_1} \quad (8.2)$$

where n = charge, R = gas constant (J/mol.K), T = Temperature (K), F = Faraday constant and p_2 and p_1 = oxygen partial pressures. The ionic transference number can then be obtained by:

$$t = \frac{E_{measured}}{E_{Nernst}} \quad (8.3)$$

8.3 References

1. Li, M., et al., *A family of oxide ion conductors based on the ferroelectric perovskite Na0. 5Bi0. 5TiO3.* Nature materials, 2014. **13**(1): p. 31-35.

2. Jaffe, B., *Piezoelectric ceramics*. Vol. 3. 1971: Academic press.

3. Jin, L., *Broadband Dielectric Response in Hard and Soft PZT*. 2011.

4. Spreitzer, M., M. Valant, and D. Suvorov, *Sodium deficiency in $Na_{0.5}Bi0.5TiO_3$.* Journal of Materials Chemistry, 2007. **17**(2): p. 185-192.

5. Anton, E.-M., et al., *Determination of depolarization temperature of $(Bi_{1/2}Na_{1/2})TiO_3$-based lead-free piezoceramics.* Journal of Applied Physics, 2011. **110**(9): p. 094108.

6. Wojcik, K. and A. Aleksandrowicz, *Polarization and thermal depolarization currents in plzt ceramics.* Ferroelectrics, 1989. **89**(1): p. 243-253.

7. Jeong, J. and Y.H. Han, *Effects of Mn-doping on TSDC and degradation of BaTiO3.* Journal of electroceramics, 2006. **17**(2-4): p. 1051-1055.

8. Sapper, E., et al., *Influence of electric fields on the depolarization temperature of Mn-doped (1-x) $Bi_{1/2}Na_{1/2}TiO_3$-$xBaTiO_3$.* Journal of Applied Physics, 2012. **111**(1): p. 014105.

9. Yoon, S.H., C.A. Randall, and K.H. Hur, *Effect of Acceptor (Mg) Concentration on the Resistance Degradation Behavior in Acceptor (Mg)-Doped BaTiO3 Bulk Ceramics: I. Impedance Analysis.* Journal of the American Ceramic Society, 2009. **92**(8): p. 1758-1765.